

**ORGANIC-BASED ELECTRO-OPTIC MODULATORS  
FOR MICROWAVE PHOTONIC APPLICATIONS**

by

David Eng

A dissertation submitted to the Faculty of the University of Delaware in partial fulfillment of the requirements for the degree of Doctor of Philosophy in Electrical and Computer Engineering

Fall 2015

© 2015 David Eng  
All Rights Reserved

ProQuest Number: 10014783

All rights reserved

INFORMATION TO ALL USERS

The quality of this reproduction is dependent upon the quality of the copy submitted.

In the unlikely event that the author did not send a complete manuscript and there are missing pages, these will be noted. Also, if material had to be removed, a note will indicate the deletion.



ProQuest 10014783

Published by ProQuest LLC (2016). Copyright of the Dissertation is held by the Author.

All rights reserved.

This work is protected against unauthorized copying under Title 17, United States Code  
Microform Edition © ProQuest LLC.

ProQuest LLC.  
789 East Eisenhower Parkway  
P.O. Box 1346  
Ann Arbor, MI 48106 - 1346

**ORGANIC-BASED ELECTRO-OPTIC MODULATORS  
FOR MICROWAVE PHOTONIC APPLICATIONS**

by

David Eng

Approved: \_\_\_\_\_  
Kenneth E. Barner, Ph.D.  
Chair of the Department of Electrical and Computer Engineering

Approved: \_\_\_\_\_  
Babatunde A. Ogunnaike, Ph.D.  
Dean of the College of Engineering

Approved: \_\_\_\_\_  
Ann L. Ardis, Ph.D.  
Interim Vice Provost for Graduate and Professional Education

I certify that I have read this dissertation and that in my opinion it meets the academic and professional standard required by the University as a dissertation for the degree of Doctor of Philosophy.

Signed:

---

Dennis W. Prather, Ph.D.  
Professor in charge of dissertation

I certify that I have read this dissertation and that in my opinion it meets the academic and professional standard required by the University as a dissertation for the degree of Doctor of Philosophy.

Signed:

---

Shouyuan Shi, Ph.D.  
Member of dissertation committee

I certify that I have read this dissertation and that in my opinion it meets the academic and professional standard required by the University as a dissertation for the degree of Doctor of Philosophy.

Signed:

---

Mark S. Mirotznik, Ph.D.  
Member of dissertation committee

I certify that I have read this dissertation and that in my opinion it meets the academic and professional standard required by the University as a dissertation for the degree of Doctor of Philosophy.

Signed:

---

Richard Martin, Ph.D.  
Member of dissertation committee

## ACKNOWLEDGMENTS

The work that I have accomplished over the past five years is a result of far more than my individual efforts and is truly representative of the support and encouragement I have received from both colleagues and mentors at the University of Delaware, as well as the family and friends I am fortunate to have in my life.

I want to start by thanking my advisor, Dr. Dennis Prather, for having confidence in me and convincing me to join his group at the University of Delaware. The insight, motivation and endless enthusiasm he provided throughout my graduate student career have made the past five years exciting, challenging and immensely gratifying.

I owe enormous thanks to Dr. Benjamin Olbricht for teaching me about organic electro-optic materials, from physical interactions on the molecular level to the macro dynamics involved with poling, as well as the myriad laboratory skills that were essential to my becoming an effective researcher. I am largely indebted to Dr. Shouyuan Shi, for patiently introducing me to the field of microwave electromagnetic design and characterization by enduring countless questions and brainstorming sessions. I want to thank Dr. Mathew Zablocki for sharing his expansive knowledge of fabrication tools and processes, and his continual willingness to offer advice in overcoming frustrations in the cleanroom.

My experience as a graduate student was heavily influenced by all of the graduate students and researchers who have worked in and around Dr. Prather's labs for the past five years. The daily conversations and interactions—both collaborative

and nonsensical—made coming to the labs every day an enjoyable experience. I want to thank everyone who I had the pleasure of interacting with during my time at the University of Delaware for their contribution to the friendly and supportive atmosphere.

I want to thank the members of my dissertation committee for offering their time and efforts to read this dissertation and attend my defense. As active and innovative researchers, I know that they all have busy schedules and I greatly appreciate their time in reviewing and critiquing my graduate work.

Finally, I am endlessly grateful to the family and friends who have accompanied me along my graduate school journey. Their unwavering support and encouragement has been immeasurably comforting. In particular my parents, Heather and James, and sister, Robin, are a continual source of insight, inspiration and happiness who have kept me on an even keel. Lastly, I am infinitely grateful to my girlfriend, Leighann, who supported me every day during my graduate school career, celebrating the triumphs, consoling me through my frustrations, and making my life an overall happy one.

## TABLE OF CONTENTS

LIST OF TABLES .....	ix
LIST OF FIGURES .....	x
ABSTRACT .....	xiv

### Chapter

1	INTRODUCTION .....	1
1.1	Microwave Photonics .....	2
1.1.1	Optical and Wireless Integration for Next Generation Communications.....	5
1.1.2	Millimeter Wave Imaging .....	7
1.2	Electro-Optic Modulators and Materials .....	10
1.2.1	Silicon Modulators .....	11
1.2.2	Lithium Niobate Modulators .....	12
1.2.3	Organic EO Material Modulators .....	13
1.3	Dissertation Outline .....	16
1.4	Original Contributions.....	18
2	DC PHASE MODULATOR DESIGN.....	22
2.1	Optical Phase Modulation .....	22
2.2	Anisotropic Electro-Optic Materials .....	24
2.2.1	Anisotropic Materials .....	24
2.2.2	Linear Electro-Optic Materials – Pockels Effect.....	25
2.2.3	Electro-Optic Phase Modulation .....	28
2.3	All Polymer DC Phase Modulator Design .....	30
2.3.1	OEOM Optical Waveguide Design .....	31
2.3.2	Numerical Optical Modeling .....	32
2.4	Conclusion.....	37

3	DC ALL-POLYMER MODULATOR FABRICATION AND CHARACTERIZATION.....	38
3.1	Low Frequency Modulator Fabrication.....	38
3.2	Inducing EO Activity – Poling.....	43
3.2.1	OEOM Poling.....	44
3.2.2	Modulator Poling.....	48
3.3	Phase Modulation Testing.....	50
3.3.1	Polarization Rotation Method.....	51
3.3.2	DC Phase Modulation Measurement.....	54
3.4	Conclusion.....	58
4	RF DIELECTRIC CHARACTERIZATION OF THIN FILMS.....	59
4.1	RF Dielectric Constant Characterization Techniques.....	59
4.2	Thin Film Microstrip Ring Resonators.....	62
4.2.1	Coupling to the Ring Resonator.....	63
4.2.2	Arc Coupler Design.....	64
4.3	Thin Film MSRR Fabrication.....	70
4.4	Dielectric Constant Measurement.....	74
4.5	Dielectric Loss Tangent Measurement.....	78
4.6	Conclusion.....	81
5	HIG FREQUENCY MODULATOR DESIGN AND FABRICATION.....	83
5.1	Traveling Wave Modulator Design.....	83
5.1.1	Impedance Matching and RF Loss.....	84
5.1.2	Wave Velocity Matching.....	87
5.1.3	Modulation Frequency Response.....	90
5.1.4	DC-RF-Optical Field Overlap.....	92
5.1.5	Effective Modulation Length.....	94
5.2	RF Microstrip Modulator Fabrication.....	100
5.2.1	Patterned Cu Ground Plane.....	101
5.2.2	Optical Waveguide Fabrication and Poling.....	102
5.2.3	Microstrip Signal Fabrication and Ground Plane Exposure.....	102
5.2.4	Edge Facet Dicing and Optical End Facet Cleaving.....	104

5.3	Conclusion.....	105
6	RF PACKAGING AND MODULATION TESTING .....	106
6.1	Ceramic CPW to Thin Film Microstrip Transition .....	107
6.1.1	Wire Bond Transition Design.....	108
6.1.2	Wire Bond Transition Testing.....	110
6.2	RF Packaging.....	113
6.2.1	Coaxial to CPW to Microstrip Integration .....	114
6.2.2	RF Packaging Loss Testing.....	116
6.3	RF Phase Modulation .....	120
6.3.1	Optical Sideband Generation.....	120
6.3.2	RF Phase Modulation Measurement .....	122
6.4	Conclusion.....	127
7	CONCLUSION .....	128
7.1	Summary.....	128
7.2	Outlook and Future Work.....	131
	REFERENCES .....	133
Appendix		
A	PERMISSIONS TO USE COPYRIGHTED MATERIAL .....	141
A.1	Figure 1.1.....	141
A.2	Figure 1.2.....	142

## LIST OF TABLES

Table 1.1: LiNbO <sub>3</sub> OEOM Comparison.....	15
Table 2.1: Optimal waveguide parameters for IKD-1-50 and SEO-25.....	36
Table 3.1: Polymer waveguide etch parameters.....	40
Table 3.2: OEOM Waveguide Core Solutions.....	41
Table 3.3: DC Modulator results for IKD-1-50 and SEO250 modulators. ....	57
Table 4.1: Radii and coupling lengths of UV15 MSRRs. ....	70
Table 4.2: Low pressure, high bias etch for via pedestal exposure.....	72

## LIST OF FIGURES

Figure 1.1: Attenuation in a silica fiber and the gain offered by an erbium doped fiber amplifier near 1550 nm. Loss and gain plots taken from Miya <i>et al.</i> (1979) [3] and Mears <i>et al.</i> (1987) [5], respectively. Reproduced by permission of the Institution of Engineering and Technology. ....	3
Figure 1.2: Atmospheric attenuation in the microwave and millimeter wave regime. Plot taken from [6], with permission. ....	4
Figure 1.3: Illustration of the integrated optical-wireless networking concept. Note that this concept is equally applicable to indoor WLAN type applications. ....	5
Figure 1.4: Visible (left) and mmW (right) image of Evans Hall at the University of Delaware taken at 77 GHz. Image courtesy of Dr. John P. Wilson. ....	8
Figure 1.5: Millimeter wave antenna and EO modulator for optical up conversion. Image courtesy of Dr. Janusz Murakowski. ....	9
Figure 2.1: Schematic diagram of a phase modulator phase shifting an optical beam relative to a reference wave. ....	22
Figure 2.2: The index ellipsoid illustrating the refractive index along three principal axes. ....	25
Figure 2.3: Basic EO phase modulator schematic. ....	28
Figure 2.4: OEOM inverted ridge waveguide structure .....	31
Figure 2.5: FDFD mode solution for an SEO250 core inverted ridge waveguide showing the TM mode vertical field component. ....	33
Figure 2.6: Two modes solved for with Lumerical FDFD algorithm. (Left) A true second order TM mode. (Right) A slab waveguide mode. ....	34
Figure 2.7: Heat map of confinement factor overlaid with lines indicating boundaries of number of supported modes. ....	35
Figure 2.8: Vertical field component of the fundamental TM mode for an IKD-1-50 waveguide (left) and an SEO250 waveguide (right). ....	36

Figure 3.1: All polymer waveguide fabrication process. ....	39
Figure 3.2: Low frequency modulator electrodes and contact pad. ....	42
Figure 3.3: (a) Cryo cleaved end facet of OEOM modulator waveguide. (b) Fully fabricated low frequency OEOM modulator. ....	43
Figure 3.4: Pre and post poling chromophore orientation. ....	45
Figure 3.5: Sample poling trace from simple reflection technique in-situ EO activity measurement. Figure courtesy of Dr. Benjamin C. Olbricht. ....	47
Figure 3.6: Modulator poling setup showing (a) thermocouple and contacted modulator, (b) spring loaded voltage and current probes and (c) enclosure with gas inlet for a N <sub>2</sub> atmosphere. ....	48
Figure 3.7: Modulator poling trace for an SEO250 device showing temperature, applied voltage and leak through current. ....	49
Figure 3.8: Polarization rotation with increases phase difference between the horizontal and vertical field components. The colored shapes represent the polarization state as $\Delta\phi$ increases, the black line is the output intensity cosine curve. ....	52
Figure 3.9: (a) Polarization rotation measurement setup diagram. (b) Picture of lab setup for polarization rotation phase modulator testing. ....	55
Figure 3.10: Polarization rotation phase modulation measurement trace. ....	56
Figure 4.1: Electric field of a microstrip transmission line. The field magnitude is represented in the heat map and the field vectors are shown as red arrows. ....	61
Figure 4.2: Traditional microstrip ring resonator with terminated feed line coupling. ....	63
Figure 4.3: Thin film microstrip ring resonator with arc coupler. ....	64
Figure 4.4: T-couple power output and coupler structure (inset). ....	66
Figure 4.5: (a) MSRR with arc coupler model in HFSS. (b) Field profile in polymer. ....	67
Figure 4.6: MSRR arc coupler resonance error modeling and analysis. ....	68

Figure 4.7: MSRR fabrication process. (a) Via pedestals electroplating. (b) Substrate deposition and curing. (c) Via pedestal exposure. (d) Microstrip feed and ring patterning and electroplating. ....	71
Figure 4.8: SEMs of fabricated MSRRs on UV15 showing (a) ring and arc coupler and (b) CPW contact point. ....	73
Figure 4.9: MSRR $\epsilon_r$ extraction procedure. (a) Resonant frequencies from a fabricated ring are measured and $\epsilon_{eff}$ is calculated. (b) The ring microstrip parameters are then measured and (c) plugged into an HFSS model to calculate $\epsilon_{eff}$ for varying values of $\epsilon_r$ . Comparison between the measured and calculated values of $\epsilon_{eff}$ yield the dielectric constant of the material. ....	75
Figure 4.10: $\epsilon_r$ calculation example showing measured resonances from which $\epsilon_{eff}$ is calculated, and a heat map of numerically calculated $\epsilon_{eff}$ for different values of $\epsilon_r$ . ....	76
Figure 4.11: Extracted $\epsilon_r$ of UV15 from 10 – 110 GHz measured with varying rings with radii ranging from 1.3 – 5 mm. ....	77
Figure 4.12: Measured, fitted and calculated microstrip loss and data. The best fit with the measured data is achieved by combining the extracted dielectric loss with calculated conduction loss that accounts for surface roughness. ....	80
Figure 5.1: S-parameters for a thin film UV15 microstrip with the contact pad taper illustrating a well matched transition. ....	85
Figure 5.2: Effective length calculations for a TE CPW traveling wave OEOM modulator.....	96
Figure 5.3: Effective length calculations for a TM CPW traveling wave OEOM modulator.....	97
Figure 5.4: Effective length calculations for a TM microstrip traveling wave OEOM modulator.....	98
Figure 5.5: RF microstrip modulator fabrication process. ....	100
Figure 5.6: SEM of diced microstrip modulator showing electroplated signal electrode, ground plane vias and diced edge facet. ....	105

Figure 6.1: (a) HFSS model of CPW to thin film microstrip transition. (b) Vertical offset and feed gap that were determined to be the dominant parameter for a low loss transition. ....	109
Figure 6.2: (a) Field transition from CPW to conductor-backed CPW to microstrip. (b) $S_{12}$ parameters for the CPW to microstrip transition with varying vertical offset. ....	110
Figure 6.3: SEM image of the CPW to thin film microstrip wirebond transition. ....	111
Figure 6.4: Direct probe measurement of CPW to microstrip wire bond transition loss. ....	113
Figure 6.5: Coaxial to CPW to microstrip modulator RF packaging. ....	114
Figure 6.6: (a) CAD drawing of the testing stage clamp assembly. (b) Photograph of a mounted and bonded CPW fed OEOM modulator. (c) Stereoscope image of feed CPW, modulator microstrip and wirebond connections. ....	116
Figure 6.7: S-parameters of RF packaged OEOM phase modulator. ....	117
Figure 6.8: CPW and modulator microstrip attenuation coefficients. ....	118
Figure 6.9: Loss factors in the microstrip modulator RF packaging illustrating a feed loss <1 dB out to 50 GHz. ....	119
Figure 6.10: RF modulation sideband testing setup. ....	123
Figure 6.11: Generated optical sidebands from 5–40 GHz of the clad microstrip modulator. ....	124
Figure 6.12: Measured and calculated sideband power roll-off for a clad and unclad microstrip modulator normalized to the sideband response at 5 GHz. .	125
Figure 6.13: Calculated modulation response for a clad and unclad microstrip modulator. ....	126
Figure A.1: Permission to use plots in Figure 1.1. ....	141
Figure A.2: Permission to use plot in Figure 1.2. ....	142

## ABSTRACT

Microwave photonics couples the abilities of microwave electronics for radar and wireless data distribution with fiber optics for low loss, lightweight, ultra-high bandwidth communications. Through electrical-to-optical and optical-to-electrical conversions, microwave photonics systems capitalize on the relative strengths inherent in each frequency regime for maximum functionality and deployability. Beyond simply replacing electrical components with optical ones, the field of microwave photonics has uncovered a variety of new and exciting possibilities that will enable next generation communication networks and contribute to the development and improvement of new and existing technologies.

Fundamental to any microwave photonic system is the electro-optic modulator that performs the electrical-to-optical conversion. Decades of engineering have produced high performance modulators in  $\text{LiNbO}_3$ , which are currently deployed in essentially all state-of-the-art microwave photonic systems. However, cutting-edge systems with higher complexity and stringent device requirements are being developed. As a result, the demand for higher performance modulators that require lower drive voltages and higher frequency operation is growing and will soon overcome the physical limitations of  $\text{LiNbO}_3$ . To address this growing demand, groundbreaking work in the field of organic electro-optic materials has been achieved over the past 10–15 years that has resulted in materials with electro-optic coefficients

up to 10 times that of  $\text{LiNbO}_3$  and with demonstrated EO response times into the THz regime.

This dissertation presents the work carried out over the past 5 years at the University of Delaware towards developing low drive-voltage, high bandwidth electro-optic modulators to support next generation microwave photonic systems. Many previous examples of organic-based electro-optic modulators have been demonstrated, but the focus of this work was on developing a simple, scalable device that would effectively harness the capabilities of organic electro-optic materials without the use of specialized cladding materials or nano-scale fabrication techniques.

Initial efforts were focused on designing an all-polymer organic electro-optic material based optical waveguide using a commercially available cladding material, and developing a fabrication procedure that successfully integrates the material without compromising its electro-optic activity. These waveguides were integrated into low frequency modulators for phase modulation demonstration that confirmed the expected high electro-optic activity and correspondingly low drive voltages. Additionally, a procedure for inducing the high electro-optic activity in the waveguide core through a process known as ‘poling’ was developed.

To transition from low frequency modulation to broadband devices capable of operating up to 50 GHz, it was necessary to gather some dielectric information of the waveguide materials for high frequency design. This is a significant challenge with the thin polymer layers used in optical waveguides, as most RF dielectric constant measurement techniques are intended for thicker substrates, on the order of 100’s of microns. Therefore a modification to the traditional microstrip ring resonator dielectric constant measurement was developed that allowed measurement of thin films down to

~10  $\mu\text{m}$ . This technique was used to acquire the necessary dielectric constant information of the waveguide materials.

A high frequency traveling wave microstrip modulator was then designed and optimized for operation up to 50 GHz. A novel, comprehensive figure of merit was developed that accounts for the applied poling field that is necessary in organic electro-optic modulators, as well as the index matching and RF attenuation that is typically considered in traveling wave modulator design. This figure of merit was used to confirm the superiority of the microstrip modulator architecture compared with TE or TM CPW configurations that have been previously demonstrated in  $\text{LiNbO}_3$  modulators.

Finally, efforts were turned towards RF packaging of the microstrip modulators for practical utilization and integration. Because RF signals typically need to be amplified, filtered or otherwise altered prior to being sent to the modulator, a heterogeneous transition from a standard ceramic RF substrate to the electro-optic modulator was developed. This single-stage wire bond transition allowed for electrical signal manipulation circuitry to be directly bonded and packaged with the modulator for compact and efficient system integration. The transition was demonstrated independently and with a fully RF packaged organic-based electro-optic modulator that was contacted with standard 2.4 mm coaxial cables. The integrated device showed modulation up to 40 GHz, the limit of the RF source.

## Chapter 1

### INTRODUCTION

Microwave photonics is the study and application of the interplay between electromagnetic waves at optical and microwave frequencies, and their interactions with matter. Despite being governed by the same set of four equations, unified and presented by Maxwell in 1865 [1], the many orders of magnitude between these two frequency regimes results in distinctly different phenomena when interacting with matter that have varying applicability for solving modern day technological challenges. Microwave fields are transported and manipulated through electrical components such as transmission lines, waveguides and antennas while optical fields are generated by lasers, carried in optical fibers and received on photodetectors. Microwave photonics utilizes both frequency regimes by converting from electrical-to-optical (E/O) or optical-to-electrical (O/E) depending on which frequency regime is more advantageous for a given application.

The performance of microwave photonic systems is often limited by the devices executing these conversions. E/O conversions can be achieved by directly modulating the laser power with the electrical signal, or by encoding the signal onto a continuous laser beam with an external electro-optic modulator. O/E conversion is accomplished with a photodiode that transforms the optical power into an electrical current. In general, the components that carry out these conversions are referred to as electro-optic (EO) devices and the vast applicability of microwave photonics drives an ever increasing demand for higher performance from these components.

The topic of this dissertation is the design, fabrication and demonstration of highly efficient EO modulators for E/O conversion. The following sections will discuss several applications within microwave photonics that require high performance modulators, and existing modulator technologies. The subsequent chapters will detail work done over the past 5 years at the University of Delaware towards developing EO modulators in organic electro-optic materials, a relatively new material system that demonstrates great promise for next generation high performance EO modulators.

## **1.1 Microwave Photonics**

Optical fiber communications were enabled by the development of the laser in 1960 and low loss silica fibers in the 1970s [2], [3]. The extremely low propagation loss of  $<0.5$  dB/km at 1550 nm and 1310 nm in optical fibers compared with 360 dB/km in coaxial cable at microwave frequencies [4], along with the availability of low noise optical amplifiers such as erbium doped fiber amplifiers (EDFAs) [5], and the low dispersion of narrow optical linewidths makes optical communications the far superior choice for point to point data transmission. The long haul information transfer abilities provided by fiber optics is illustrated in Figure 1.1 by the attenuation of silica fibers and gain offered by EDFAs. Fiber optic based systems have already been designed and deployed in applications such as cable distribution and super computer interconnects. As the requisite technologies advance, increasingly powerful and agile systems continue to be developed.

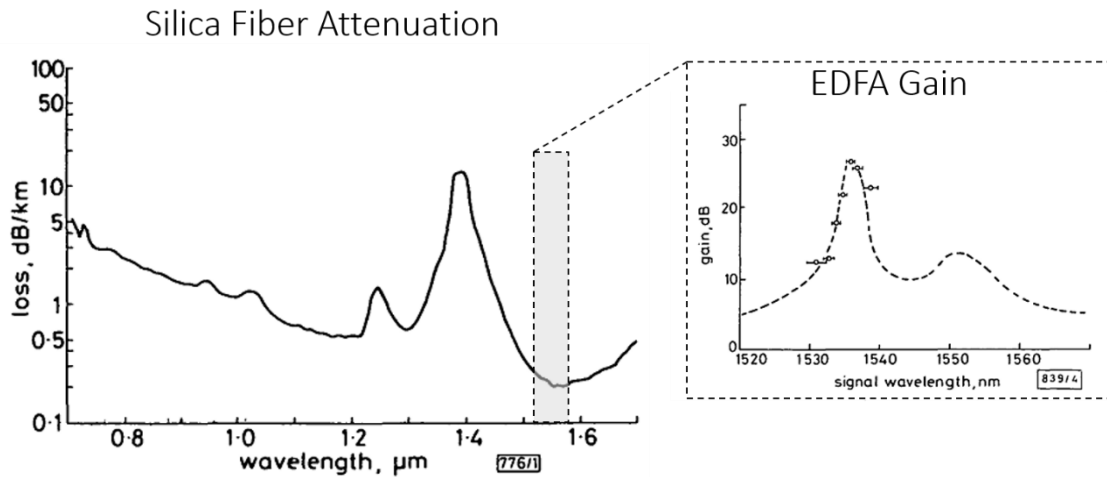


Figure 1.1: Attenuation in a silica fiber and the gain offered by an erbium doped fiber amplifier near 1550 nm. Loss and gain plots taken from Miya *et al.* (1979) [3] and Mears *et al.* (1987) [5], respectively. Reproduced by permission of the Institution of Engineering and Technology.

Microwave electronics such as radio communications and radar were developed in the early to mid-1900's and solve different types of communication problems by radiating and receiving electromagnetic waves in the MHz and GHz range over broad spatial distributions enabling communication with mobile receivers or sensing objects in unknown locations. Windows of low atmospheric attenuation below 0.5 dB/km are available in these frequency regimes, as shown in Figure 1.2, which make it possible for far reaching communications or large area sensing through atmospheric wave propagation.

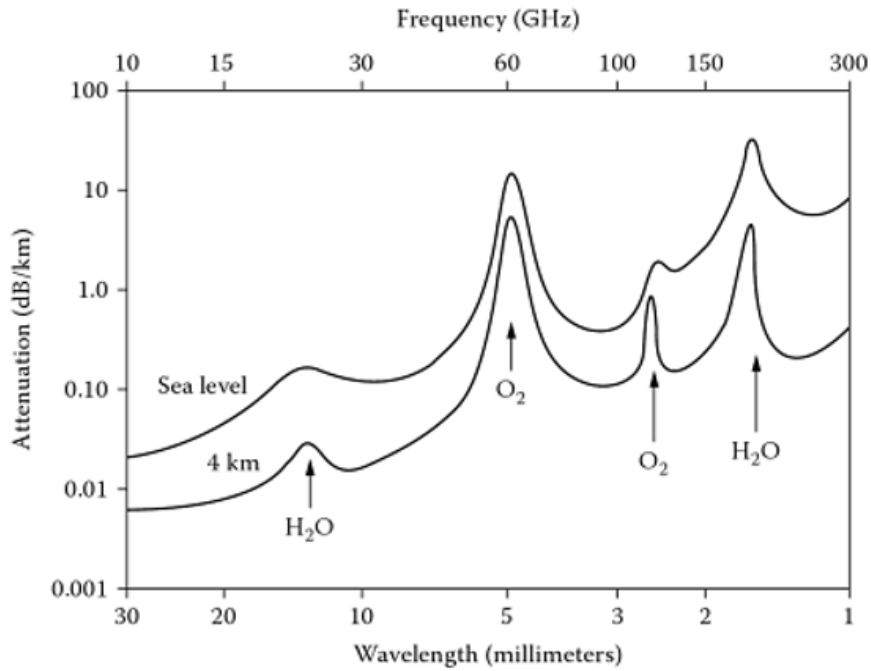


Figure 1.2: Atmospheric attenuation in the microwave and millimeter wave regime.  
Plot taken from [6], with permission.

As increasingly complex microwave systems are developed the accumulation of bulky metal components increases the size, weight and required power (SWaP), and increased loss degrades performance at high bandwidths, both of which result in limitations to developing deployable systems. Additionally because maximum data rates are set by the carrier frequency according to the Nyquist-Shannon sampling theorem, microwave electronics is ultimately limited in data capacity. Microwave photonics leverages the low SWaP and THz frequencies of fiber optic communications to enable more compact and efficient microwave systems with bandwidth limited by the EO components rather than the sampling rate. However, beyond just replacing copper components with silica fibers, the interplay of optical and microwave fields has

led to the development of new techniques for applications such as RF generation and imaging. A few of these applications will be discussed in the following sections.

### 1.1.1 Optical and Wireless Integration for Next Generation Communications

Sending radio signals over optical fibers is another solution offered by microwave photonics that harnesses the advantages of optical communications to distribute radio signals to and from transmitting and receiving antennas at widely spaced remote locations [4], [7]. Radio-over-fiber (RoF) systems, also referred to as hybrid-fiber-radio, convert the electrical RF signal to an optical carrier at a central distribution site and then transport that signal via optical fiber to one or many antenna sites as shown schematically in Figure 1.3.

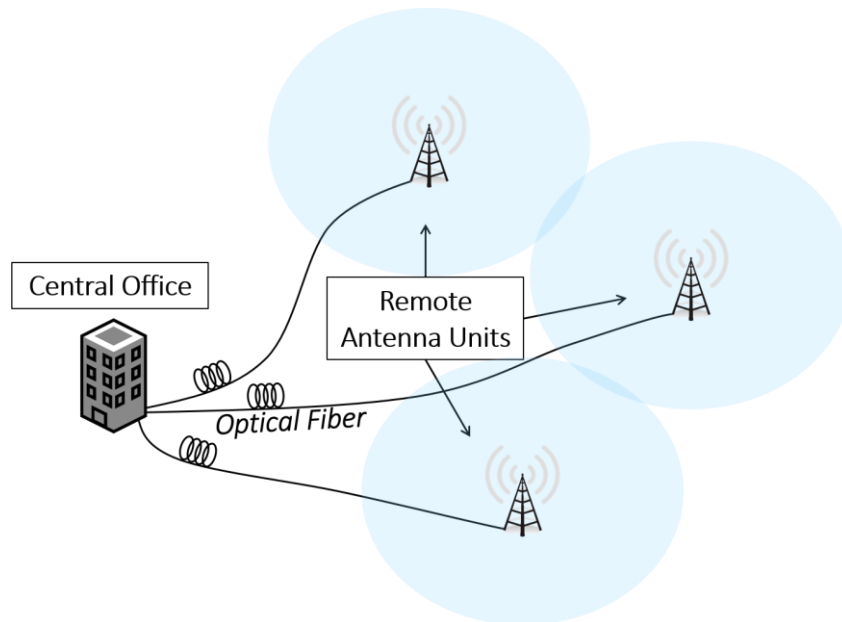


Figure 1.3: Illustration of the integrated optical-wireless networking concept. Note that this concept is equally applicable to indoor WLAN type applications.

The low loss and essentially limitless bandwidth of optical fibers enables large spatial coverage with large volumes of data controlled from a central processing location. Fiber optic data transmission not only enables the distribution of RF signals but also allows for increased data throughput via wavelength division multiplexing and subcarrier division multiplexing. Passive optical networks for routing and distribution from a central office to antenna base stations are being developed for low cost infrastructures to provide long reaching wireless distribution [8], [9]. RoF systems have been deployed in cellular networks, wireless local area networks (WLAN) and mobile broadband networks [8]. A commercially deployed system by CommScope Inc., capable of operating from 800 MHz to 2.5 GHz has been utilized at major events like to 2000 Olympic Games in Sydney, Australia and the 2006 World Cup in Germany [4], [10].

Advancements in optical-wireless integration are extending far beyond the 2.5 GHz frequency range however [11]. Next generation 5G wireless systems aiming to utilize millimeter wave frequency carriers near 30 GHz for exceptionally high data rates will undoubtedly deploy photonic links to distribute signals from central offices to remote antenna units. The higher atmospheric attenuation of electromagnetic waves in the millimeter wave regime is overcome and indeed utilized by small-cell systems that are broadly distributed with optical networks but have short-range wireless reach enabling increased spectral reuse [12]. Research in fiber-wireless (FiWi) networks in just the past ten years has been extremely active in exploring network configurations for optimal bandwidth and deployability. For example radio-and-fiber networks that implement different control protocols for the optical and wireless media enable longer reach than RoF systems by eliminating limitations imposed by optical propagation

delays causing timeouts in wireless protocols [13]. There have also been designs for moving cell networks that could enable high quality of service broadband internet to fast moving users such as train passengers [14], as well as systems that photonically generate the RF signals at remote antenna locations by optical heterodyning [15]. Photonically enabled wireless systems in the W-band (75-110 GHz) [16], at 120 GHz [17], and even up to above 200 GHz [15] have all been studied in the continual march towards next generation high volume data distribution networks.

Implicit in all of these systems are the E/O and O/E conversions at the distribution and access points and the components performing the conversions quickly become limiting factors. Recent advances in high power, broadband photodiodes such as uni-traveling carrier photodiodes have shown operation up to 400 GHz, though with very little output power [18]. More recent modified uni-traveling carrier photodiodes have demonstrated high output RF power up to 2.5 dBm at 40 GHz [19]. High performance modulators capable of operating at frequencies into the millimeter wave regime with low drive voltages are equally important for acceptable signal-to-noise ratios. Efforts towards developing these modulators are also ongoing, as will be discussed in this dissertation.

### **1.1.2 Millimeter Wave Imaging**

Aside from just communications systems, microwave photonics has been used to enable or enhance other technologies. A prime example of this is passive imaging at millimeter wave (mmW) frequencies that has been developed here at the University of Delaware in conjunction with Phase Sensitive Innovations (Newark, DE). These imaging systems operate based on thermal or blackbody radiation in the mmW regime (30–300 GHz), which can be gathered and analyzed to reproduce an image of the

radiating body. There are several low atmospheric attenuation windows in the mmW regime near 35 GHz, 95 GHz, 140 GHz and 220 GHz, observable in Figure 1.2, that allow sufficient wave propagation for collection and analysis [20]. Imaging at these wavelengths is of great value to many defense applications because of its ability to see through common visual obscurants such as dust, smoke and fog. Additionally because the energy being gathered is simply blackbody radiation, mmW imaging systems can be completely passive, requiring no illumination to construct an image. Sample imagery at 95 GHz from a W-band mmW imaging system developed at the University of Delaware is shown in Figure 1.4.



Figure 1.4: Visible (left) and mmW (right) image of Evans Hall at the University of Delaware taken at 95 GHz. Image courtesy of Dr. John P. Wilson.

Millimeter wave imaging systems consist of a single scanning antenna or an array of antennas that gather the radiation and implement some detection scheme to convert the data to a usable format to reconstruct the image. Early demonstrations of mmW imaging processed the gathered radiation with heterodyne detection or direct detection [21]. More recent systems however use a photonic technique called optical up-conversion in which the received radiation is used to drive a phase modulator and generate optical sidebands which are isolated with optical filters [20]. A drawing of an antenna and EO modulator optical up-conversion unit is shown in Figure 1.5.

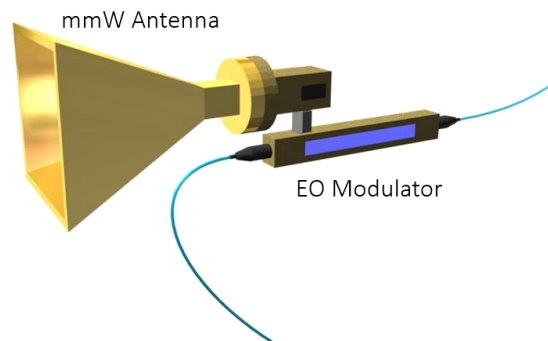


Figure 1.5: Millimeter wave antenna and EO modulator for optical up conversion. Image courtesy of Dr. Janusz Murakowski.

This technique has been used to generate an image in multiple ways. The isolated sideband power is proportional to the received mmW energy and can be fed to a photodiode to produce a baseband photocurrent signal for back end electrical processing and image generation [20]. Alternatively, a variation of this technique has been demonstrated that uses a distributed aperture array and keeps the mmW signal in the optical domain. In this technique the image is reconstructed using the Fourier

properties of an optical lens to project the image onto a CCD camera, eliminating the need for bulky back end processing of electrical signals [22].

The imagers developed in this group are capable of imaging at 35 GHz, 77 GHz and 94 GHz, a primary barrier in building these systems was the availability of EO modulators that can effectively modulate at these high frequencies. To address this requirement EO modulators that operate up to a record setting 300 GHz were developed [23]. These modulators have enabled the realization of the mmW imaging systems and remarkable results have been obtained. The imaging could be improved however with higher performance modulators that would require a smaller drive voltage from the received mmW energy, lowering the signal-to-noise ratio and increasing image quality [20].

## **1.2 Electro-Optic Modulators and Materials**

As evidenced by the preceding sections EO modulators are a crucial component to enabling microwave photonic systems for a variety of reasons. High frequency operation is an obvious parameter that directly relates to the achievable bandwidth. The required drive voltage, parametrized as the voltage required to induce a  $\pi$  phase shift,  $V_\pi$ , is also an important parameter that dictates the voltage level needed at the input to the E/O conversion.  $V_\pi$  also impacts overall systems performance in metrics such as the noise figure, which is proportional to  $V_\pi^2$  for photonic links [24]. Other factors such as optical loss and power handling, device flexibility, and ease of packaging are also important in choosing or developing modulators for specific applications. Many modulators in various materials systems that demonstrate EO activity have been developed. A more thorough discussion of EO activity and

modulator operation will be presented in subsequent chapters, but a brief overview of existing modulator technologies is given here.

### **1.2.1 Silicon Modulators**

EO modulators built in Si have been demonstrated largely in efforts towards monolithically integrated Si photonic based optical interconnects to enable continued bandwidth improvement in chip-to-chip and rack-to-rack interconnects for digital computation [25]. The intrinsic linear EO effect in Si is too small for practical modulator design so Si modulators most commonly implement the plasma dispersion effect that changes the refractive index and absorption of Si based on the concentration of free charges which can be controlled with a PN or PIN diode structure [26]. Various Si modulator designs such as carrier accumulation, carrier depletion and resonant architectures have been demonstrated with bandwidths up to 40 Gb/s and drive voltages below 0.5 V (not in the same device) [25], [26]. Si modulators however introduce considerable optical loss due the challenge of coupling to and from the tightly confined Si waveguides that are on the order of 100's of nm in size and the propagation loss associated with optical light traveling through or near doped regions of Si. Additionally, the high RF attenuation of Si makes traveling wave architectures that could support operation at high microwave and millimeter wave frequencies largely inaccessible.

Si based modulators have been demonstrated that offer potential solutions for photonic integrated circuits and could leverage existing foundry processes. However as microwave photonic applications requiring modulators that operate above 50 GHz become more prevalent alternate material systems become more appealing for their RF and EO characteristics.

### 1.2.2 Lithium Niobate Modulators

The majority of currently deployed EO modulators for microwave photonics are built in lithium niobate ( $\text{LiNbO}_3$ ).  $\text{LiNbO}_3$  is a crystalline material with an EO coefficient,  $r_{33}$ , of  $\sim 30$  pm/V and acceptably low RF losses that allow for simple traveling wave architectures that efficiently transfer RF signal energy to the interaction region with a coplanar waveguide (CPW) transmission line.  $\text{LiNbO}_3$  is also highly transparent at telecommunication wavelengths and optical waveguides can be fabricated by diffusing Ti strips into the substrate that demonstrate 0.2 dB/cm propagation loss and 0.5 dB coupling loss per facet with a single mode fiber [27]. These waveguides have also demonstrated high optical power handling with demonstrated irradiation up to 500 mW without inducing any serious damage [24]. A significant challenge in  $\text{LiNbO}_3$  modulators is the large index dispersion between optical and RF frequencies, varying from 2.14 to 5.6. This index mismatch can be overcome by tuning the RF effective index with a silicon dioxide buffer layer and controlled electrode heights [28], however this often requires tedious iterative processing to appropriately split the RF field between the  $\text{LiNbO}_3$ , silicon dioxide and air.

Decades of engineering have produced highly impressive  $\text{LiNbO}_3$  modulators that have demonstrated modulation as high as 300 GHz with drive voltage around 6 V [23]. There are also numerous commercially available  $\text{LiNbO}_3$  modulators from vendors such as Thorlabs Inc. and EOSpace with varying operating frequencies and drive voltages that are deployed in systems like the ones listed in the previous sections. However, as cutting edge microwave photonic systems demand increasingly higher performance modulators, the physical limitations of the  $\text{LiNbO}_3$  are being reached. In particular the 30 pm/V  $r_{33}$  of  $\text{LiNbO}_3$  enforces a lower limit on  $V_\pi$  unless

very long interaction lengths are used ( $>5$  cm for  $<1$  V). The rigid crystalline structure of  $\text{LiNbO}_3$  is another limiting factor that restricts the achievable device architectures to planar top down fabrication on an existing wafer. Another impediment to more advanced design is the low index contrast of Ti diffused  $\text{LiNbO}_3$  waveguides which is typically below 0.5% [27]. This makes optical components such as splitters, delay lines or gratings difficult to achieve without additional high index material depositions or very large bending radii. While  $\text{LiNbO}_3$  modulators will likely always play an important role in many microwave photonic systems, higher performance modulators with lower drive voltages at higher bandwidths and possibly homogeneously integrated optical components will be needed to improve current systems and enable future ones.

### **1.2.3 Organic EO Material Modulators**

For next generation modulators a new class of organic EO materials (OEOMs) has been heavily researched and developed over the past 10–15 years resulting in materials that have demonstrated EO coefficients as high as 300 pm/V, ten times higher than  $\text{LiNbO}_3$  [29], and remarkably fast response times, with demonstrations into the THz regime [30]. Beyond the performance enhancements that would result from these EO properties alone, OEOMs are synthesized as raw chromophores or covalently bonded to polymer chains, and dissolved in solvents for a solution based, spin processable material system. This allows for a much broader range of device architectures that can most efficiently harness the enhanced EO properties of OEOMs and also presents the opportunity for flexible devices built entirely in polymer [31].

Another advantage of OEOM waveguides is the higher optical index contrast that is achievable by appropriate choice of cladding material and OEOM index tuning

based on the chromophore and host polymer ratios in a given solution. The index contrast in this work for example varied from 6–12 %, compared with 0.5% of  $\text{LiNbO}_3$ . The higher available index contrast allows for compact MMI splitters and tighter bending radii for homogeneously integrated optical components [32]. Loss in OEOM based waveguides can be kept to below 1 dB/cm [27], but will vary depending on the material properties of the OEOM being implemented. Optical power handling at telecom wavelengths in OEOMs was an initial challenge because of photo-degradation that occurs due to reactions between EO chromophores and oxygen. However, recent advances in molecular engineering and processing of these chromophores has significantly improved their photo-stability and 100 mW irradiations at 1550 nm without significant degradation, determined by monitoring output waveguide power, have been demonstrated [33]. Finally, a significant advantage of using OEOMs is their very low dielectric attenuation and index dispersion out to 400 GHz [34], which is ideal for low loss, well index matched broadband traveling wave modulators. A comparison of  $\text{LiNbO}_3$  and OEOMs is summarized in Table 1.1.

Table 1.1: LiNbO<sub>3</sub> OEOM Comparison

	<b>LiNbO<sub>3</sub></b>	<b>OEOMs</b>
<b>EO Activity (<math>r_{33}</math>)</b>	30 pm/V	Up to 300 pm/V
<b>Frequency Response</b>	300 GHz (in device)	15 THz (material meas.)
<b>Index Dispersion (RF <math>\rightarrow</math> Opt.)</b>	High (2.14 $\rightarrow$ 5.6)	Low (< 15% variation)
<b>Power Handling Demonstrated</b>	500 mW	100 mW
<b>Index Contrast</b>	0.5%	Varies, up to 12%
<b>Optical Loss</b>	0.2 dB/cm	< 1 dB/cm (Material dependent)
<b>Physical Characteristics</b>	Crystalline, brittle	Polymer, flexible

The inherent advantages of OEOMs have garnered the attention of researchers pursuing high performance EO modulator designs, and additional enticement is found in the prospect of the performance enhancement that will result from the continual research in OEOM synthesis and processing with photonic applications in mind. Many novel and impressive OEOM based modulators have been developed over the past two decades with demonstrations of low drive voltages and broadband operation. For exceptionally low drive voltages OEOM filled Si and TiO<sub>2</sub> slot waveguides that confine and enhance the modulation field across the EO waveguide core were designed and demonstrated at low frequencies [35], [36], and designs for slot modulators operating at RF frequencies have been proposed [37], [38]. OEOM filled Si photonic crystals have been used to create a slow light effect that increases the effective modulator interaction length while minimizing the device footprint allowing for lumped element electrodes and operation up to 25 GHz [39]. Both slot and photonic crystal based modulators exhibit impressively low drive voltages down to below 1 V but suffer from increased sensitivity to scattering losses due to the enhanced fields as well as fabrication complexity, typically requiring electron-beam

lithography, which is a significant hurdle to device yield for practical device deployment.

Exceptionally low drive voltage devices that do not require nanoscale lithography have also been pursued through the use of more novel cladding and electrode materials. Intriguing work using transparent conducting oxides that allow electrodes to be patterned in direct contact with the OEOM for a maximum modulation field without introducing high optical loss have demonstrated drive voltages between 2–3 V [40]. As will be discussed in a later chapter a unique challenge in OEOMs is the need to pole the materials to attain the promised high EO coefficients. To this end, specialized sol-gel cladding materials that offer higher conductivity than the OEOM core have been developed to optimize the poling field across the active region. These devices have demonstrated higher in device EO coefficients and correspondingly low drive voltages down to 0.65 V [41], [42]. The fast EO response time and excellent index matching offered by OEOMs has also been harnessed to demonstrate phase modulation at frequencies beyond 100 GHz in a microstrip traveling wave modulator configuration [43]. The impressive performance demonstrated by the aforementioned devices illustrates the enormous potential of OEOM based EO modulators. The tradeoffs between different devices architectures could lead to varying solutions for different applications and motivates continued work in OEOM modulator development.

### **1.3 Dissertation Outline**

The many examples of OEOM based modulators have yielded a large knowledge base for the processing and integration of OEOMs for microwave photonic applications. As was alluded to in the preceding section, most of the recent work is

dependent on high tolerance fabrication techniques or specialized materials. The focus of this research was the development of an all-polymer modulator that harnesses the high performance characteristics of OEOMs in a simply fabricated, scalable device architecture that utilizes all commercially available materials. Efforts were also directed towards RF packaging to enable practical integration of high frequency devices for microwave photonic applications. The trajectory of this work began with vials of synthesized EO chromophores and concluded with an RF packaged modulator with operation at 40 GHz. Efforts along the way included optical waveguide and low frequency modulator development, RF material characterization, traveling wave modulator design, and RF transitions and packaging. The following dissertation will present this work, done at the University of Delaware since August 2010. The chapters are organized according to the following outline.

Chapter 2 will discuss the basics of EO phase modulation including a review of anisotropic EO materials. It will then cover the basics of phase modulator design and the work that was done simulating the all polymer optical waveguide to determine field overlap and number of supported modes. Optimal waveguide dimensions are determined for DC phase modulation with two different OEOMs.

Chapter 3 will outline the fabrication routine for the OEOM based optical waveguide and DC modulation electrodes. Poling, the technique used to induce EO activity in the OEOM waveguide, will then be introduced and discussed including the procedure for poling materials in-device and the modulator poling station that was designed and built in-house. Next, a phase modulation measurement based on polarization rotation will be explained in detail and the DC phase modulation testing setup is shown. Finally, DC phase modulation results are presented.

Chapter 4 will discuss an RF dielectric characterization technique using microstrip ring resonators. The technique is a novel modification to existing measurements and allows for the RF characterization of thin polymer films such as OEOMs. The design, fabrication and implementation of the measurement will be presented along with measured dielectric and attenuation constants.

Chapter 5 discusses traveling wave RF modulator design. A detailed explanation of important design factors such as RF loss and velocity matching are presented, along with a newly formulated comprehensive figure-of-merit for OEOM modulators that includes the importance of the poling field for inducing EO activity. Optimal dimensions for a traveling wave microstrip OEOM modulator will be determined and the fabrication process will be presented.

Chapter 6 investigates RF packaging of a microstrip OEOM modulator and addresses the challenge of making a smooth RF transition from standard coaxial connectors to the modulation electrode as would be necessary for practical utilization. A wire bond transition is designed and demonstrated, and a full RF packaging scheme is developed that enables high frequency modulation testing. This packaging scheme is implemented and modulation results out to 40 GHz are presented.

#### **1.4 Original Contributions**

The work presented in this dissertation comprises the research I performed during the course of my Ph.D. graduate student career. This work has resulted in the following original contributions:

1. Fabrication and demonstration of a simply fabricated, all-polymer, symmetric clad UV15 OEOM based phase modulator.

2. Design and demonstration of a modified microstrip ring resonator RF dielectric constant measurement technique implementing an arc coupler for thin film characterization applicable to OEOMs.
3. Dielectric constant characterization of UV15 cladding material out to 110 GHz.
4. Formulation of comprehensive figure-of-merit of OEOM modulators including poling field analysis.
5. Design and demonstration of a CPW to thin film microstrip wire bond transition for heterogeneous integration of microstrip modulators with RF substrates.
6. Demonstration of RF packaged OEOM microstrip modulator heterogeneously integrated with a ceramic substrate.

#### **Peer Review Journal Articles**

1. **D. Eng**, S. Kozacik, I. Kosilkin, J. Wilson, D. Ross, S. Shi, L. Dalton, B. Olbricht, and D. Prather, "Simple Fabrication and Processing of an All-Polymer Electro-Optic Modulator," *IEEE Journal of Selected Topics in Quantum Electronics*, pp. 1–1, 2013.
2. **D. Eng**, B. C. Olbricht, S. Shi, and D. W. Prather, "Dielectric characterization of thin films using microstrip ring resonators,"

*Microwave and Optical Technology Letters*, vol. 57, no. 10, pp. 2306–2310, Oct. 2015.

3. **D. Eng**, Z. Aranda, B. C. Olbricht, S. Shi, and D. W. Prather, “Heterogeneous Packaging of Organic Electro-Optic Modulators with RF Substrates,” *Photonics Technology Letters, IEEE*. **Accepted for publication November 19, 2015.**

### **Conference Presentations and Publications**

1. **D. Eng**, S. Kozacik, S. Shi, B. C. Olbricht, and D. W. Prather, “All-Polymer modulator for high frequency low drive voltage applications,” in *Proc. SPIE 8983, Organic Photonic Materials and Devices XVI*, 898316, March 7, 2014.
2. **D. Eng**, S. Kozacik, J. P. Wilson, D. Ross, S. Shi, B. C. Olbricht, D. W. Prather, "Simply fabricated all polymer electro-optic modulator," in *Photonics Conference (IPC), 2013 IEEE* , vol., no., pp. 30-31, 8-12, Sept. 2013.
3. B. C. Olbricht, **D. Eng**, S. Kozacik, S. Shi, D. W. Prather, "The role of processing towards application of organic EO material modulators," in *Photonics Conference (IPC), 2013 IEEE* , vol., no., pp.647-648, 8-12 Sept. 2013.

4. **D. Eng**, S. Kozacik, B. C. Olbricht, S. Shi, D. W. Prather, “All-polymer modulator for high frequency low drive voltage applications,” in *Proc. SPIE 8622, Organic Photonic Materials and Devices XV*, 86220T, March 6, 2013.
5. B. C. Olbricht, **D. Eng**, S. Kozacik, D. Ross, D. W. Prather, “Processing of organic electro-optic materials: solution-phase assisted reorientation of chromophores,” in *Proc. SPIE 8622, Organic Photonic Materials and Devices XV*, 86220U, March 6, 2013.
6. **D. Eng**, S. Kozacik, B. C. Olbricht, S. Shi, D. W. Prather, “Broadband low-drive voltage polymer electro-optic modulator,” in *Proc. SPIE 8259, RF and Millimeter-Wave Photonics II*, 82590C, February 23, 2012.
7. S. Kozacik, **D. Eng**, M. Zablocki, M. Roman, A. Sharkawy, J. Murakowski, B. C. Olbricht, S. Shi, D. W. Prather, “Dual vertical slot modulator for millimeter wave photonics,” in *Proc. SPIE 8259, RF and Millimeter-Wave Photonics II*, 82590D, February 23, 2012.

## Chapter 2

### DC PHASE MODULATOR DESIGN

#### 2.1 Optical Phase Modulation

Phase modulation is a simple method of encoding RF electrical signals onto a THz infrared optical carrier in which the optical phase front is shifted by a given amount that corresponds to an electrical signal, shown schematically in Figure 2.1.

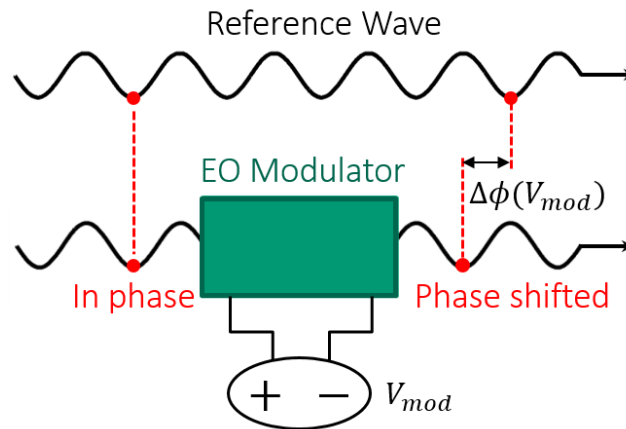


Figure 2.1: Schematic diagram of a phase modulator phase shifting an optical beam relative to a reference wave.

A phase shift is commonly achieved by altering the index of refraction of the medium through which the optical beam is traveling, resulting in an optical path length change and a phase shift relative to an unmodulated beam. This can be understood by considering the optical carrier in phasor form in the frequency domain

$$\mathbf{E} = \mathbf{E}_0 e^{-j\beta_0 z} \quad (2.1)$$

where  $\beta_0$  is the wavenumber defined as  $\beta_0 = \frac{2\pi}{\lambda} n_0$ , and  $n_0$  is the refractive index of the core material. The subscript,  $0$ , indicates the intrinsic, unmodulated refractive index. By changing the refractive index of the material a small amount  $\Delta n$ , the wavenumber is slightly changed to  $\beta = \beta_0 + \Delta\beta$  where  $\Delta\beta = \frac{2\pi}{\lambda} \Delta n$ . The resulting phase shift for an index modulation of  $\Delta n$  is then

$$\Delta\phi = \frac{2\pi}{\lambda} \Delta n L, \quad (2.2)$$

where  $L$  is the interaction length of the modulator. Information can be transmitted with an optically phase shifted beam in multiple ways: it can be recombined with another coherent beam to produce amplitude modulation via constructive and destructive interference; the phase shift itself can be evaluated by reference with a local oscillator (phase shift keying) or referenced to the phase of the previous bit (differential phase shift keying); or the generated optical sidebands with amplitude proportional to the phase shift can be measured. This change in refractive index of the optical material can be accomplished in several ways including thermal variation [44], [45], carrier injection in semiconductors such as silicon [25], [26] or even mechanical stress [46]. However, for high speed, low drive voltage index modulation the most commonly used method is the implementation of EO materials whose optical indexes shift in response to an applied electric field. An overview of EO materials will be given in the next section.

## 2.2 Anisotropic Electro-Optic Materials

### 2.2.1 Anisotropic Materials

In isotropic, linear materials the constitutive relationship is a linear relation between the electric field  $\mathbf{E}$  and the electric displacement  $\mathbf{D}$  through the scalar permittivity  $\epsilon$

$$\mathbf{D} = \epsilon \mathbf{E} = \epsilon_r \epsilon_0 \mathbf{E}$$

where  $\epsilon_0$  is the permittivity of free space and  $\epsilon_r$  is the relative dielectric constant of the material, related to the refractive index by  $n = \sqrt{\epsilon_r}$ . In anisotropic media each component of the electric displacement vector does not necessarily change with the same linear relationship. So the constitutive relation is a vector equation

$$\mathbf{D} = \bar{\epsilon} \mathbf{E}$$

where  $\bar{\epsilon}$  is a  $3 \times 3$  permittivity tensor that relates each component of the electric displacement to all three components of the electric field. A coordinate system can always be found to make the permittivity tensor diagonal meaning that the components of  $\mathbf{E}$  and  $\mathbf{D}$  are parallel and directed along 3 axes referred to as the principal axes. Similarly the refractive index  $\bar{n}$  becomes a diagonal  $3 \times 3$  tensor whose diagonal components correspond to the principal axes. This diagonal  $3 \times 3$  tensor can be represented geometrically as an ellipsoid defined by

$$\frac{x_1^2}{n_1^2} + \frac{x_2^2}{n_2^2} + \frac{x_3^2}{n_3^2} = 1 \quad (2.4)$$

where  $n_1, n_2$  and  $n_3$  are the diagonal components of the  $\bar{n}$  tensor and  $x_1, x_2,$  and  $x_3$  are the 3 principal axes. This geometrical representation is commonly called the index ellipsoid and is a useful visual tool that illustrates the relative index along each axis as shown in Figure 2.2.

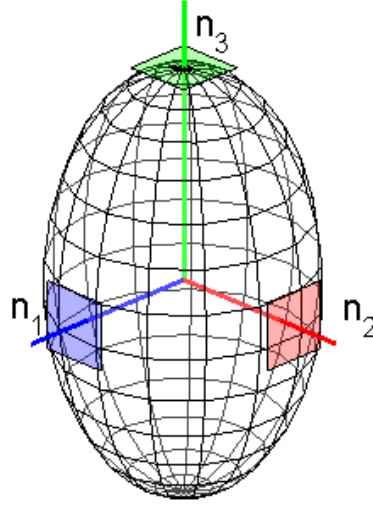


Figure 2.2: The index ellipsoid illustrating the refractive index along three principal axes.

### 2.2.2 Linear Electro-Optic Materials – Pockels Effect

To explore the effect of EO activity on the index ellipsoid it is convenient to restate the constitutive relation in terms of the impermeability  $\eta = \frac{1}{\epsilon_r}$  [47]

$$\epsilon_0 \mathbf{E} = \frac{1}{\epsilon_r} \mathbf{D} = \bar{\eta} \mathbf{D}. \quad (2.5)$$

Note that  $\bar{\eta} = \frac{1}{\epsilon_r} = \frac{1}{n^2}$  where  $\bar{n}$  is the optical refractive index and both  $\bar{\eta}$  and  $\bar{n}$  are unitless. The change in the impermeability of an isotropic material due to an externally applied scalar electric field  $E$  can be represented in a power series

$$\eta(E) = \eta_0 + rE + \sigma(E^2). \quad (2.6)$$

The linear term is known as Pockels effect and the coefficient  $r$  is the linear EO response constant with units of inverse electric field, m/V. For anisotropic materials we must consider the impermeability tensor stated in Equation 2.5. Written out more explicitly the vector constitutive relation for anisotropic materials in terms of the impermeability tensor  $\bar{\eta}$  is

$$\epsilon_0 \begin{bmatrix} E_1 \\ E_2 \\ E_3 \end{bmatrix} = \begin{bmatrix} \eta_{11} & \eta_{12} & \eta_{13} \\ \eta_{21} & \eta_{22} & \eta_{23} \\ \eta_{31} & \eta_{32} & \eta_{33} \end{bmatrix} \begin{bmatrix} D_1 \\ D_2 \\ D_3 \end{bmatrix}. \quad (2.7)$$

Introducing an EO response into the impermeability tensor of an anisotropic material greatly complicates the vector impermeability because in general each component of the impermeability tensor is influenced by all three components of the applied field to varying degrees as is expressed in Equation 2.8

$$\eta_{ij}(\mathbf{E}) = \eta_{0,ij} + \sum_{k=1}^3 r_{ijk} E_k + \sigma(\mathbf{E}^2). \quad (2.8)$$

This can be written as the sum of vectors and matrices

$$\bar{\eta}(\mathbf{E}) = \bar{\eta}_0 + \bar{r}_1 E_1 + \bar{r}_2 E_2 + \bar{r}_3 E_3 \quad (2.9)$$

where each matrix  $\bar{r}_k$  is a second rank  $3 \times 3$  tensor and the full  $\bar{r}$  tensor is a  $3 \times 3 \times 3$  third rank tensor

$$\bar{r} = \underbrace{\begin{bmatrix} r_{11,1} & r_{12,1} & r_{13,1} \\ r_{21,1} & r_{22,1} & r_{23,1} \\ r_{31,1} & r_{32,1} & r_{33,1} \end{bmatrix}}_{k=1} \underbrace{\begin{bmatrix} r_{11,2} & r_{12,2} & r_{13,2} \\ r_{21,2} & r_{22,2} & r_{23,2} \\ r_{31,2} & r_{32,2} & r_{33,2} \end{bmatrix}}_{k=2} \underbrace{\begin{bmatrix} r_{11,3} & r_{12,3} & r_{13,3} \\ r_{21,3} & r_{22,3} & r_{23,3} \\ r_{31,3} & r_{32,3} & r_{33,3} \end{bmatrix}}_{k=3}. \quad (2.10)$$

The linear EO response tensor  $\bar{r}$  is therefore a 27 component tensor, and each of the  $3 \times 3$  matrices in Equation 2.10 is multiplied by the appropriate component of the external field and summed to find the total anisotropic impermeability tensor in Equation 2.9.

Simplifications to the above analysis can be made by observing the symmetry in the impermeability tensor, namely that  $\eta_{ij} = \eta_{ji}$ . This implies that the linear EO coefficient tensor in Equation 2.10 should show the same symmetry. The typical renaming convention to account for this symmetry is

$$\bar{\eta}_k = \begin{bmatrix} \eta_{11,k} & \eta_{12,k} & \eta_{13,k} \\ \eta_{21,k} & \eta_{22,k} & \eta_{23,k} \\ \eta_{31,k} & \eta_{32,k} & \eta_{33,k} \end{bmatrix} \rightarrow \begin{bmatrix} \eta_{1,k} & \eta_{6,k} & \eta_{5,k} \\ \eta_{6,k} & \eta_{2,k} & \eta_{4,k} \\ \eta_{5,k} & \eta_{4,k} & \eta_{3,k} \end{bmatrix} \quad (2.11)$$

for the impermeability tensor, and similarly

$$\bar{r}_k = \begin{bmatrix} r_{11,k} & r_{12,k} & r_{13,k} \\ r_{21,k} & r_{22,k} & r_{23,k} \\ r_{31,k} & r_{32,k} & r_{33,k} \end{bmatrix} \rightarrow \begin{bmatrix} r_{1,k} & r_{6,k} & r_{5,k} \\ r_{6,k} & r_{2,k} & r_{4,k} \\ r_{5,k} & r_{4,k} & r_{3,k} \end{bmatrix} \quad (2.12)$$

for the linear EO response tensor. The full  $\bar{r}$  tensor can then be rewritten as a  $6 \times 3$  rank 2 tensor

$$\bar{r} = \begin{bmatrix} r_{1,1} & r_{1,2} & r_{1,3} \\ r_{2,1} & r_{2,2} & r_{2,3} \\ r_{3,1} & r_{3,2} & r_{3,3} \\ r_{4,1} & r_{4,2} & r_{4,3} \\ r_{5,1} & r_{5,2} & r_{5,3} \\ r_{6,1} & r_{6,2} & r_{6,3} \end{bmatrix} \quad (2.13)$$

where the columns now represent the 3 components of the external electric field and the rows represent the 6 impermeability relationships between the components of  $\mathbf{E}$  and  $\mathbf{D}$ , summarized in Equation 2.11.

To convert from impermeability back to the refractive index to find  $\Delta n$  due to Pockels effect we will consider a single component of  $n$  and  $\eta$  to calculate

$$\Delta n = \frac{dn}{d\eta} \Delta \eta. \quad (2.14)$$

Recalling that  $n = \frac{1}{\sqrt{\eta}}$  we find

$$\frac{dn}{d\eta} = -\frac{\eta^{-\frac{3}{2}}}{2} = -\frac{(\eta_0 + rE)^{-\frac{3}{2}}}{2}. \quad (2.15)$$

Plugging Equation 2.15 and the first order term from Equation 2.6,  $\Delta \eta = rE$ , into 2.14 we find

$$\Delta n = -\frac{rE}{2(\eta_0 + rE)^{\frac{3}{2}}} = -\frac{rE}{2\left(\frac{1}{n_0^2} + rE\right)^{\frac{3}{2}}}. \quad (2.16)$$

The EO coefficient  $r$  is a very small value, on the order of pm/V ( $10^{-12}$ ), and  $E$  will be on the order of V/ $\mu\text{m}$  ( $10^6$ ) so  $rE$  will be on the order of  $10^{-6}$ . We can therefore safely make the approximation  $\frac{1}{n_0^2} + rE \rightarrow \frac{1}{n_0^2}$  which leaves us with

$$\Delta n = -\frac{1}{2}n_0^3 r E, \quad (2.17)$$

which is the commonly seen form of Pockels effect for linear refractive index modulation. For an anisotropic EO material in the presence of an external field  $\mathbf{E}$  the refractive index shifts along each principal axis according to the components of  $\mathbf{E}$  and the corresponding components of  $\bar{r}$  in 2.13, altering the shape of the index ellipsoid. In LiNbO<sub>3</sub> and OEOMs the dominant component of the  $\bar{r}$  tensor is a response between a parallel field and index component and by convention the coordinate systems are defined such that it is labeled  $r_{33}$ .

### 2.2.3 Electro-Optic Phase Modulation

In a standard EO phase modulator an optical waveguide with an EO core material is fabricated in between electrodes capable of directing an external field over the core to activate the  $r_{33}$  coefficient as shown in Figure 2.3.

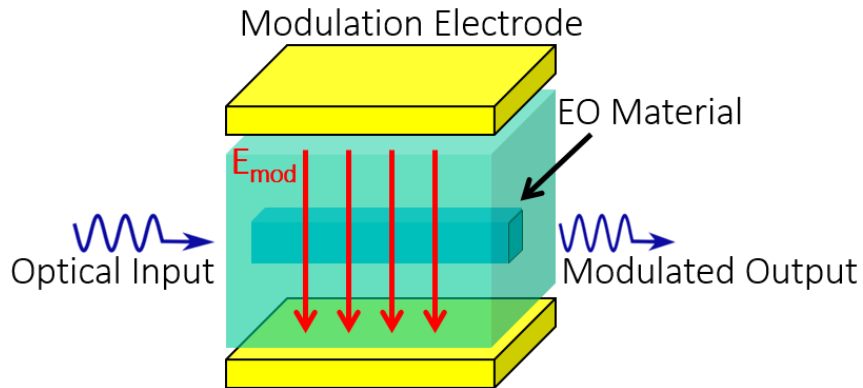


Figure 2.3: Basic EO phase modulator schematic.

In most practical waveguides the optical mode will not be 100% confined to the EO material and the modulating field may have some spatial variation resulting in a non-optimal modulation field. These field distributions are accounted for by an overlap integral [48] that quantifies the degree to which the modulating field  $E_{mod}$  overlaps with the optical mode  $E_{opt}$ , given by

$$\Gamma = \frac{d}{V} \frac{\iint_{EO\ core} E_{mod}(x,y) \cdot |E_{opt}(x,y)|^2 dx dy}{\iint_{-\infty}^{\infty} |E_{opt}(x,y)|^2 dx dy}. \quad (2.18)$$

Including this factor with Equations 2.2 and 2.17 given an external electric field  $E = \frac{V}{d}$  results in an EO induced phase shift

$$\Delta\phi = -\frac{\pi}{\lambda} n_0^3 r_{33} \frac{V}{d} \Gamma L \quad (2.19)$$

where  $d$  is the spacing between electrodes,  $V$  is the applied voltage and  $L$  is the interaction length of the modulator.

A common figure-of-merit for phase modulators is the voltage required to induce a  $\pi$  phase shift, this voltage is commonly referred to as  $V_\pi$ . Setting  $\Delta\phi = \pi$  in Equation 2.19 and solving for  $V$  we find

$$V_\pi = \frac{d\lambda}{n_0^3 r_{33} \Gamma L}. \quad (2.20)$$

From this expression we see that the modulator  $V_\pi$  can be lowered by increasing the interaction length,  $L$ , and decreasing the electrode gap,  $d$ , as well as ensuring strong overlap,  $\Gamma$ , between the optical and modulating fields. Since the interaction length of the modulator can be limited by the optical or RF loss of the device, an often quoted figure-of-merit is  $V_\pi L$ , which emphasizes how effectively the modulator architecture overlaps the optical and modulation fields, as well as the EO activity of the device.

### 2.3 All Polymer DC Phase Modulator Design

As was mentioned in the introduction, the past several decades have produced myriad OEOM based modulator designs. Very impressive work on Si/OEOM [35], [37], [49] and TiO<sub>2</sub>/OEOM [36], [50] hybrid devices has been accomplished demonstrating  $V_{\pi}L$  products as low as 1 V·mm. Some of these devices include exotic features like nano-slots for enhanced field confinement [38], [51], [52] and photonic crystals for a slow light effect that increases the effective interaction length [39]. Most of these devices however come at the expense of highly specialized fabrication procedures such as e-beam lithography with nm scale fabrication tolerances, while still others implement specialized cladding materials that need to be synthesized for the specific application [42], [53]. These fabrication and material requirements make scalability and repeatability a significant challenge.

A primary goal in this work was to develop a simply fabricated, scalable modulator that would harness the advantages of OEOMs without requiring specialized fabrication steps or materials, and that could be easily modified to integrate various OEOMs as they continue to be developed. For that reason an all-polymer device architecture was pursued that would require only standard UV lithography and easily available materials. The electrode architecture is a simple lumped element microstrip configuration with the modulating electrode patterned above the waveguide and a ground plane electrode below to produce a vertically directed modulating field through an EO waveguide core carrying a vertically polarized (transverse magnetic, TM) optical mode.

### 2.3.1 OEOM Optical Waveguide Design

One of the major challenges in designing an OEOM waveguide is developing a fabrication process that will not damage the material either by high temperatures, direct exposure to UV light, or contact with an incompatible solvent. In particular, patterning the OEOM to provide lateral confinement for a waveguide mode proves difficult because the OEOM is usually incompatible with photoresist, developers or resist removers involved in the process. The most common technique [41] [54] [55] to circumvent this issue is to pattern a trench in the bottom cladding layer and then spin deposit the OEOM core and subsequent cladding layer, which results in an inverted ridge waveguide structure as shown in Figure 2.4.

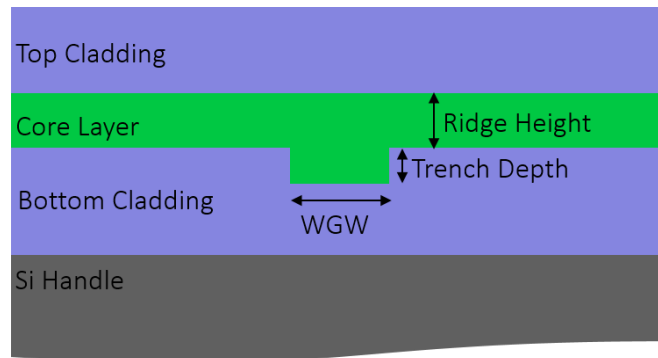


Figure 2.4: OEOM inverted ridge waveguide structure

The sequence of processing steps used to fabricate an inverted ridge waveguide offers the freedom to develop a patterning step without considering the stability of the OEOM. Once the core and top cladding layers are cured, the OEOM is encapsulated and protected during subsequent processing steps as long as the top cladding layer is a sufficiently impermeable material.

Determining the optimal cladding material includes device design factors such as optical index and loss as well as practical factors like material compatibility and cost. Significant work has been accomplished towards developing conductive cladding materials for improved poling efficiency (poling will be discussed in a following section) without introducing significant optical propagation loss [40], [42], [56]. However, as previously mentioned, the performance enhancement gained by some of these exotic cladding materials comes at the expense of fabrication complexity, including material synthesis processes that can impede manufacturability. In accordance with the goal of a simple, scalable device, the cladding layers in this device were made of UV15, a commercially available UV-thermal curable epoxy from Masterbond (NJ). A key advantage of UV15 is that it contains no solvents, eliminating any concerns of solvent incompatibility with the OEOM core. Additionally, once cured UV15 is a reasonably robust passivation layer, capable of shielding the OEOM from the solvents and resists of future processing steps. The index of UV15 has been reported [54] as 1.504 at 1550 nm. The index of the OEOM core varies depending on the material that is integrated. In this work two different OEOMs were implemented: IKD-1-50, a chromophore synthesized at the University of Washington; and SEO250, a commercially available chromophore generously supplied by the manufacturer Soluxra L.L.C. (WA). The refractive index of these materials were measured in house using the attenuated total internal reflection technique [57] to be 1.65 and 1.77 for IKD-1-50 and SEO250, respectively.

### **2.3.2 Numerical Optical Modeling**

Optimal waveguide dimensions were determined for both operational efficiency and fabrication ease. The Lumerical MODE finite difference frequency

domain (FDFD) mode solver [58] was implemented to determine the number of modes supported for a given set of dimensions, and to calculate the mode confinement. A sample mode profile for a first order TM mode in an SEO250 waveguide is shown in Figure 2.5.

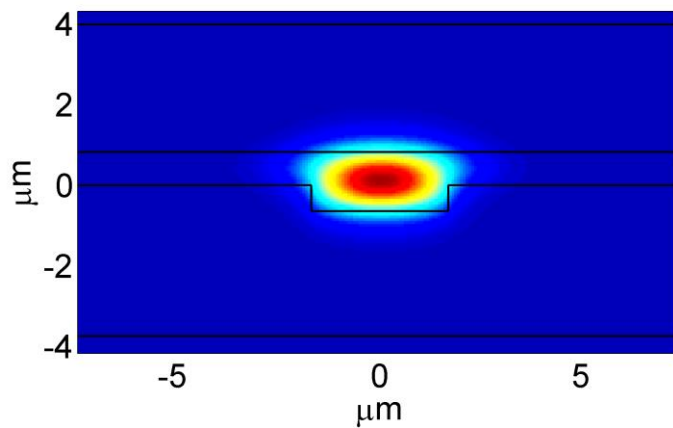


Figure 2.5: FDFD mode solution for an SEO250 core inverted ridge waveguide showing the TM mode vertical field component.

A TM EO phase modulator optical waveguide should be excited with only a single vertically polarized mode as multiple modes will result in dispersion and degraded signal fidelity. Waveguide dimensions were therefore designed to support only the fundamental TE and TM modes. The FDFD mode solving algorithm reports all electric field modes that are valid solutions to the waveguide architecture, index profile and boundary conditions. Perfectly matched layer (PML) [59] boundary conditions were used at the edges of the computational space to prevent solutions

corresponding to reflected fields; however non-physical modes with field maxima located at the boundary edges and modes supported outside of the waveguide core can also be found that solve the system of equations. An algorithm was therefore developed that evaluated each TM mode solution to determine if it was a true waveguide mode or not based on the position of the field maxima relative to the waveguide core. An example of a true second order TM waveguide mode and a slab mode that would not be excited by an optical fiber is shown in Figure 2.6. This algorithm was used to count the number of supported modes for a given set of waveguide parameters.

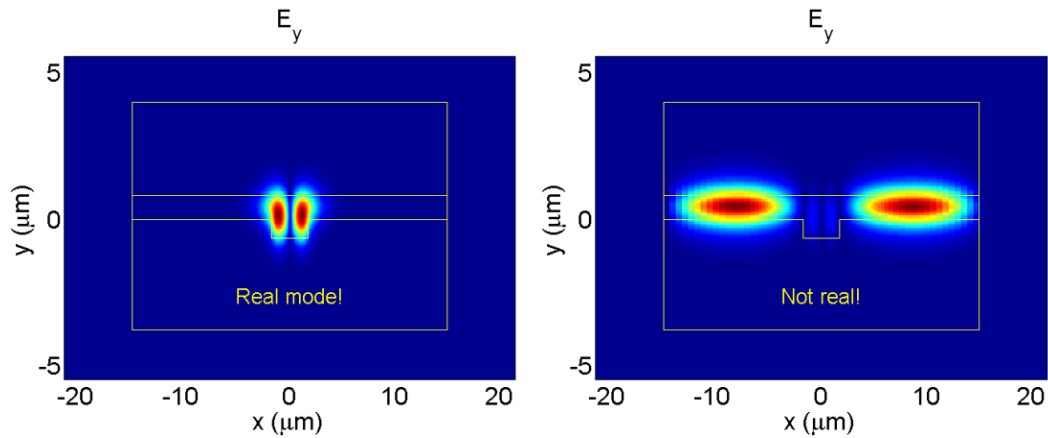


Figure 2.6: Two modes solved for with Lumerical FDFD algorithm. (Left) A true second order TM mode. (Right) A slab waveguide mode.

For the low frequency phase modulator it was assumed that the directly applied vertical modulation field was uniform throughout the optical waveguide with field strength  $E = V/d$ . The overlap integral in Equation 2.18 is therefore reduced to a simple confinement factor

$$\Gamma = \frac{\iint_{EO\ Core} |E_{opt}(x,y)|^2 dx dy}{\iint_{-\infty}^{\infty} |E_{opt}(x,y)|^2 dx dy}. \quad (2.21)$$

Mode confinement of the fundamental TM mode was calculated by exporting the field profiles to MATLAB and numerically calculating Equation 2.21. The algorithm for mode counting and mode confinement calculations were implemented on broad sweeps of the waveguide dimensions to find optimal waveguide parameters. An example confinement factor heat map with the number of supported modes indicated with overlaid lines for an SEO250 waveguide is shown in Figure 2.7.

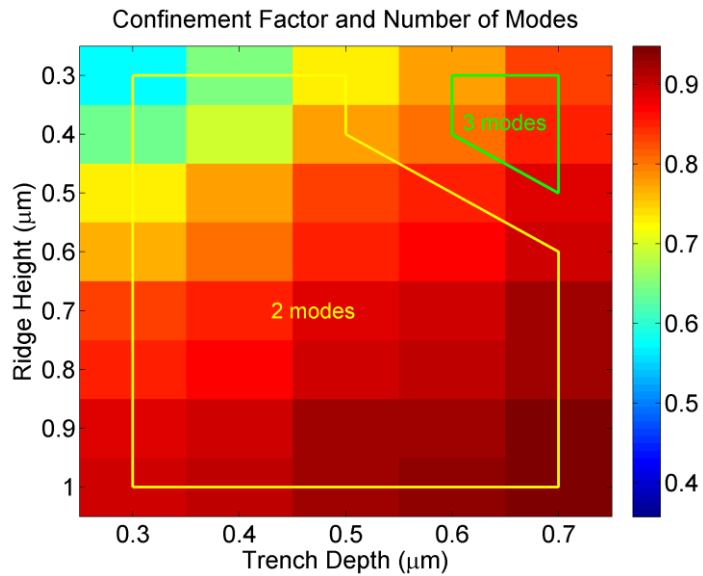


Figure 2.7: Heat map of confinement factor overlaid with lines indicating boundaries of number of supported modes.

Because of the relatively low index contrast (compared to Si-air, for example) between the UV15 cladding layers and the core material the tolerance on waveguide dimensions were reasonably relaxed and variations within a few 100's of nm still

resulted in adequate waveguide operation. A second order mode was supported for some of the waveguide parameters that were implemented, however because these modes are odd and the optical fiber launches an even mode, the coupling overlap to the higher order mode is very low. Second order modes generated by waveguide defects were occasionally observed to perturb modulation measurements, and were corrected for in subsequent device iterations. Optimized dimensions for IKD-1-50 and SEO250 are shown in Table 2.1 and the resulting mode profiles are shown in Figure 2.8. Note that for SEO250 waveguides the higher index contrast allows for a similar confinement with a smaller ridge height, which is contributes to keeping a thinner polymer stack.

Table 2.1: Optimal waveguide parameters for IKD-1-50 and SEO-25.

Material	Guide Width	Trench Depth	Ridge Height	Confinement
IKD-1-50	4 $\mu\text{m}$	0.5 $\mu\text{m}$	1.5 $\mu\text{m}$	94%
SEO250	3.5 $\mu\text{m}$	0.65 $\mu\text{m}$	0.75 $\mu\text{m}$	91%

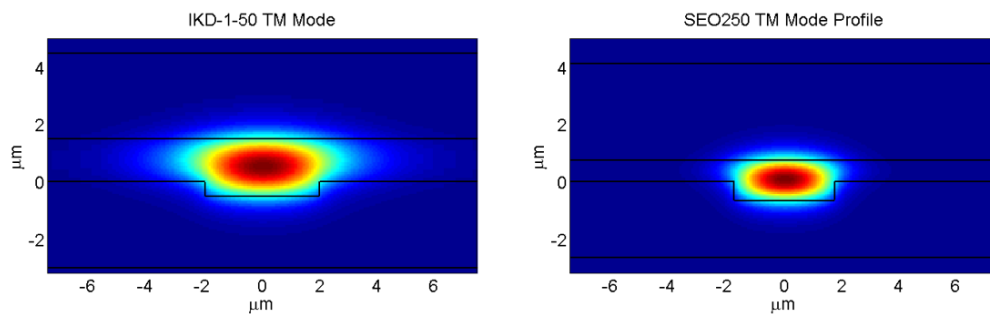


Figure 2.8: Vertical field component of the fundamental TM mode for an IKD-1-50 waveguide (left) and an SEO250 waveguide (right).

The top and bottom cladding layer thicknesses were not optimized waveguide variables as they do not contribute significantly to the shape of the optical mode. They are, however, very important to the final modulator performance because they dictate the total waveguide thickness and therefore the electrode gap  $d$  in Equation 2.20 for  $V_\pi$ . The cladding thicknesses should therefore be kept as thin as possible to provide the largest modulation field per applied voltage. The cladding thickness is limited by fabrication capabilities, as will be discussed in the following chapter, and optical conduction loss that will result from close proximity of the optical mode and the modulation electrodes. The modes in Figure 2.8 show visually that the optical mode is largely contained to within 2  $\mu\text{m}$  of the OEOM core and MODE solutions including the ground plane and modulation electrodes indicated that the spacing was sufficient to not induce significant additional loss. Therefore cladding thicknesses of  $\sim 3 \mu\text{m}$  were determined to be adequate for the modulator waveguide.

## 2.4 Conclusion

The inverted ridge waveguide architecture was chosen to be compatible with standard microfabrication processing techniques. Numerical mode simulations were performed to optimize the waveguide for maximum mode confinement in the OEOM core material and single mode operation. From these simulations dimensions for IKD-1-50 and SEO250 waveguides were determined. The waveguide cladding layer thicknesses were chosen for maximum modulation efficiency without introducing conduction loss due to proximity to the optical mode. The following chapter will discuss the fabrication routine that was developed to build this modulator, and the measured low frequency modulation results.

## Chapter 3

### DC ALL-POLYMER MODULATOR FABRICATION AND CHARACTERIZATION

#### 3.1 Low Frequency Modulator Fabrication

A fabrication challenge particular to OEOM modulators is the sensitivity of OEOMs to solvents and high temperatures. Organic solvents will quickly decompose the chromophores resulting in no EO activity and physical damage to the fabricated structures. Extremely high temperatures will also degrade the chromophores but lower temperatures from 100–150 °C that are frequently used in common fabrication processes can also have a deleterious effect on the EO activity for reasons related to the EO activity inducing poling step. Poling will be discussed in detail in the following section, however, it is necessary to mention here that the need to pole these devices necessitates keeping the temperature during processing to below the material's poling temperature, which is between 100–150 °C depending on material.

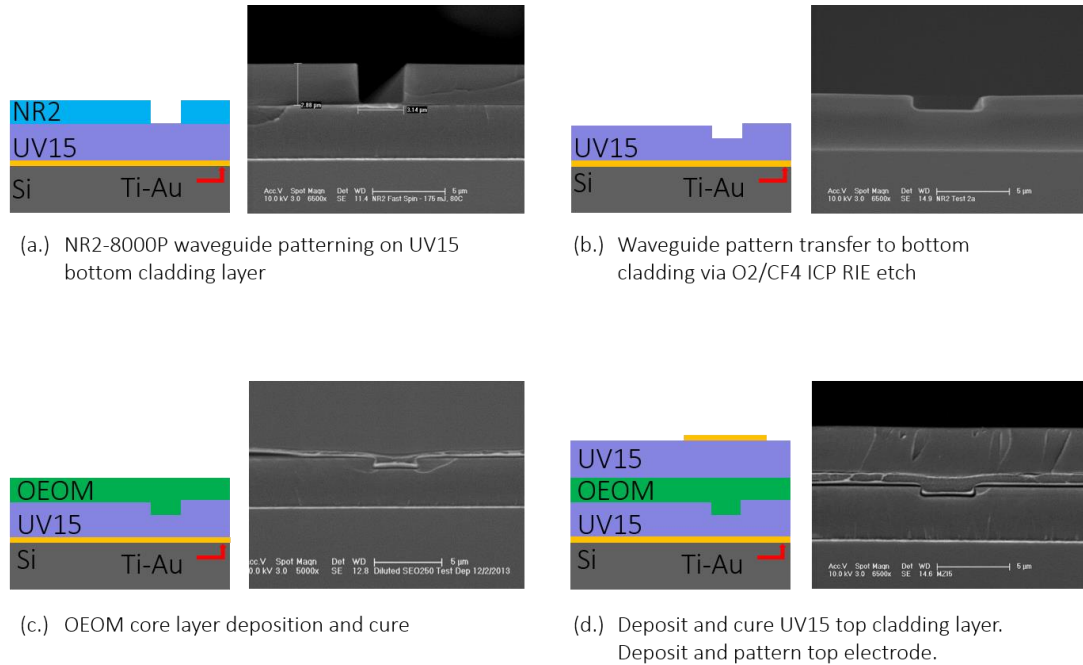


Figure 3.1: All polymer waveguide fabrication process.

As previously mentioned the fabrication process for these devices was designed to be straightforward and scalable. The modulators are fabricated on standard test Si wafers. The ground plane electrode consists of a 10 nm Ti adhesion layer and a 150 nm Au ground plane deposited via electron beam evaporation. The wafer is then cleaved into 2.5×3 cm substrates for individual sample processing. Cladding layer thicknesses are controlled by spin speeds and duration. Because UV15 has no evaporating solvents elongated spin times can continually decrease the film thickness down to below 3 μm. Keeping the UV15 undiluted also avoids solvent incompatibilities with the core layer during the top cladding deposition. The bottom UV15 cladding layer is spun at 6000 rpm for 7 minutes to achieve a layer thickness of

~3  $\mu\text{m}$ . This layer is cured with 5  $\text{J}/\text{cm}^2$  of 365 nm radiation, and a >20 hour bake at 110  $^\circ\text{C}$  under constant vacuum.

Waveguides of the desired width are patterned on a 1 mm pitch across the surface of each device using a 3  $\mu\text{m}$  thick NR2-8000P soft mask as shown in Figure 3.1 (a). The cured UV15 surface is cleaned with an acetone and isopropanol rinse at 3000 rpm and the resist is deposited at 6000 rpm for 60 seconds. The edge bead is removed with an acetone dipped swab prior the soft bake at 150  $^\circ\text{C}$  for 60 seconds. The resist is then brought into contact with the photomask with the waveguide pattern and exposed with 175  $\text{mJ}/\text{cm}^2$  of 365 nm light. Following the exposure is a post exposure bake (PEB) for 60 seconds at 100  $^\circ\text{C}$  and a 60 second develop in RD6.

The waveguide pattern is transferred to the UV15 bottom cladding with a 3:1  $\text{O}_2/\text{CF}_4$  ICP plasma that etches at a rate of ~15 nm/sec. The plasma etch parameters are listed in Table 3.1.

Table 3.1: Polymer waveguide etch parameters

Pressure	$\text{O}_2$ Flow	$\text{CF}_4$ Flow	ICP Power	Bias Power
13 Pa	50 sccm	16.7 sccm	270 W	50 W

Following the ICP etch, the soft mask is removed at room temperature with RR41, a commercial resist remover produced by the same manufacturer as the resist, Futurrex (NJ). The ability for a gentle room temperature resist removal process that would not attack the UV15 was a large driver in choosing NR2 as the photoresist. A 30 second submersion with slight agitation sufficiently removes the soft mask, however, it was found that RR41 leaves a residual layer on the UV15 that decomposes the EO chromophores. To drive off this residual the patterned surface is rinsed with

acetone and isopropanol, and then baked at 100 °C for  $\geq 4$  hours. This pattern transfer procedure yields smoothly etched surfaces and vertical sidewalls with a chemically stable surface for OEOM deposition, as shown in Figure 3.1 (b).

With the waveguide pattern completed all that remains is to deposit the core and top cladding layers, and to pattern electrodes. The OEOM film thickness is controlled by varying the percent of solids in the solution, as well as spin speed. OEOM solutions for IKD-1-50 and SEO250 are shown in Table 3.2.

Table 3.2: OEOM Waveguide Core Solutions

OEOM Solution	Solids	Solvent	% Solids
IKD-1-50	25% chromophore in PMMA	1,1,2-trichloroethane	4–8 %
SEO250	SEO250 in polymer host (proprietary)	Dibromomethane	3–5%

Prior to the OEOM deposition the etched UV15 surface is spun at 3000 rpm and blown off with N<sub>2</sub> to remove any particles that may have landed on the surface while transferring between the oven and spin processor. The OEOM core is spin deposited at 1250 rpm for 30 seconds, transferred to a hot plate at 70 °C for 5 minutes to drive off the solvent, and then thoroughly cured under vacuum for ~20 hours at 85 °C as shown in Figure 3.1 (c).

The waveguide fabrication is completed with a top cladding layer of UV15, which is deposited and cured using the same spin and UV cure process as the bottom cladding layer. For IKD-1-50 devices the thermal cure temperature is decreased to 100 °C to keep the device well below the material's poling temperature of 112 °C. The importance of this will be discussed in the following section on poling.

At this point the OEOM is sufficiently encapsulated, and electrodes can be patterned without damaging the core. The electrode pattern for each sample has three vertically stacked electrode configurations that each include three 16 mm long, 50  $\mu\text{m}$  wide lines connected to an elliptical contact pad for electrical contact during poling and modulation, resulting in nine possible modulated waveguides per sample. A diagram of the electrode configuration is shown in Figure 3.2.



Figure 3.2: Low frequency modulator electrodes and contact pad.

A 100 nm Au layer is evaporated onto the surface of the top UV15 layer and the electrode pattern is aligned and patterned over the waveguides using a positive resist AZ-5214. The lithography process for this resist includes a 30 second 90 °C soft bake, which is well below the poling temperature of both IKD-1-50 and SEO250. The electrodes are wet etched using a commercial iodine-based Au wet etch and the resist is removed with a flood UV exposure and another developing step.

The samples are then cleaved into three separate devices to be poled individually. The optical end facets are prepared by cyro-cleaving, a procedure in which the device is submerged in liquid nitrogen until completely frozen, and then cleaved along a crystal plane perpendicular to the optical waveguides. When cleaved at room temperature the polymer layers frequently tear and result in uneven jagged

edges. Cryo-cleaving fractures the polymers along the crystal plane providing flat and smooth surfaces suitable for optical coupling. Figure 3.3 (a) shows a cryo-cleaved optical end facet and Figure 3.3 (b) shows a completed modulator.

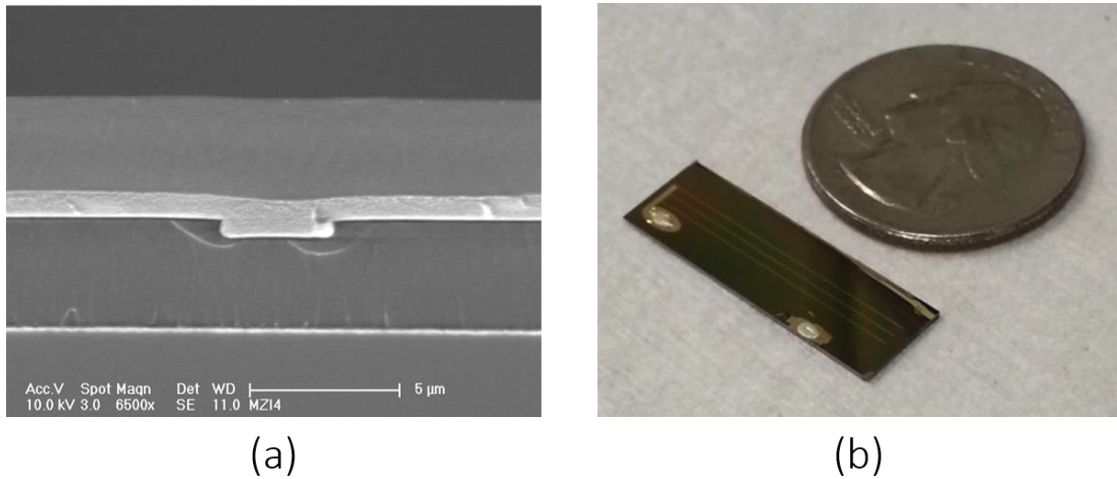


Figure 3.3: (a) Cryo cleaved end facet of OEOM modulator waveguide. (b) Fully fabricated low frequency OEOM modulator.

### 3.2 Inducing EO Activity – Poling

For a material to exhibit a linear EO effect it is necessary for the physical structure of that material to be non-centrosymmetric. A satisfying explanation for this is presented by Yariv [60] and summarized here. If a centrosymmetric material had a first order EO response such that an applied field  $E$  resulted in an index change of  $\Delta n_1 = rE$ , then the same applied field oriented in the opposite direction should result in an index change  $\Delta n_2 = -rE = -\Delta n_1$ . However, because the material is assumed to be centrosymmetric an inversion along any axis should yield the same result. The

previously stated equality would therefore only be true for  $r = 0$ , *i.e.* no linear EO activity.

Traditional EO materials such as  $\text{LiNbO}_3$  are crystalline and the required non-centrosymmetry is inherent in their lattice structure. By contrast OEOMs are prepared as a homogeneous solution before being spin cast onto the device. The active elements in an OEOM solution are dipolar conjugated molecules with delocalized  $\pi$ -electrons that can be easily shifted along the molecular structure when in the presence of an external electric field, resulting in a change in polarization [29]. After spin deposition these dipolar molecules are randomly oriented and form an amorphous and inherently centrosymmetric film. For EO activity it is therefore necessary to break this centrosymmetry by aligning the chromophores in the film along a specified axis. This is accomplished through a process known as poling.

### 3.2.1 OEOM Poling

Poling has been thoroughly studied in large part by the chemistry research groups that develop these EO chromophores [29], [61], [62] and while some exotic methods of chromophore alignment such as self-assembly and solution phase poling have been explored, the most practical and commonly used method is thermally enabled electric field poling. In this technique the film of randomly oriented chromophores as shown schematically in Figure 3.4 (a) is heated to just below its glass transition temperature in the presence of a strong DC electric field, typically between 50–100 V/ $\mu\text{m}$ . At this elevated temperature the chromophores are sufficiently mobilized such that the electrostatic forces between the dipolar molecule and the applied poling field can rotate the chromophore towards the axis defined by the poling field as shown in Figure 3.4 (b). Once the poling temperature has been reached and the

chromophores are aligned the film is brought back down to room temperature before removing the poling field, thereby locking in the order. It is important for the poling field to remain in place until the chromophores are immobilized at room temperature to prevent dipole-dipole interactions in which the positive and negative ends of two dipoles in close proximity are attracted to each other and rotate to form a net zero dipole moment. These dipole-dipole interactions also make it important to keep the temperature of the OEOM below  $T_p$  prior to poling, as a net zero dipole moment unit will not experience the rotational forces needed to align the chromophore with the poling field.

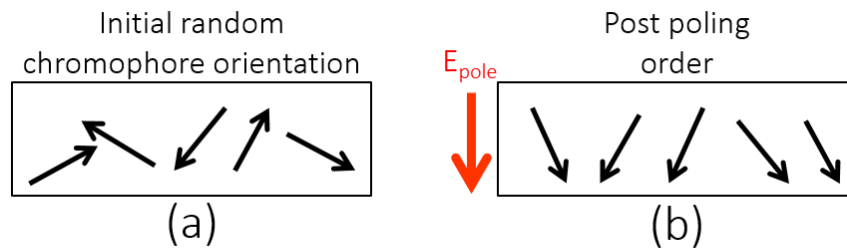


Figure 3.4: Pre and post poling chromophore orientation.

The degree of EO activity that results from this process is proportional the average molecular acentric order parameter  $\langle \cos^3 \theta \rangle$  that relates the degree to which the chromophores have been aligned to the axis defined by the poling field. Studies of OEOM poling efficiency have been largely conducted on simple slab devices consisting of a single OEOM layer sandwiched between two electrodes using two different measurements. The simple reflection technique [63] reported by Teng and Man uses a glass substrate and a transparent indium tin oxide (ITO) bottom electrode

that allows simultaneous free space optical and electrical probing for *in-situ*  $r_{33}$  measurement during poling. While the  $r_{33}$  values from this technique have been observed to be inaccurate [64], the relative EO activity that can be tracked during the poling process yields valuable information for optimizing the poling process. For more accurate measurements of  $r_{33}$  the attenuated total internal reflection technique [57] uses the same slab device and prism couples light into the OEOM slab, then tracks the shift in coupling angle as the index is modulated to back out the poled material's  $r_{33}$ . From these measurements information such as optimal poling temperature, applied bias and gas atmosphere are ascertained. As might be expected the resultant EO activity increases with the poling field strength due to the larger forces on the dipolar chromophores. However, as the poling field is increased the risk of shorting through a defect in the polymer stack or dielectric breakdown increases, and poling fields therefore rarely exceed 100 V/ $\mu\text{m}$ . Additionally it was found that exposure to atmospheric  $\text{O}_2$  at elevated temperatures causes chromophore decomposition, optimal poling is therefore achieved in a  $\text{N}_2$  atmosphere.

Perhaps the most crucial parameter in the poling process is the poling temperature  $T_p$ , which must be determined for each particular OEOM. This is the temperature at which the molecules become sufficiently mobile to align with the electric field without suffering any decomposition due to overheating. Unfortunately the multiple layers, varying electrode configurations and Si substrates of practical EO modulator structures prohibit *in-situ* measurements such as the simple reflection technique making in-device poling an enduring challenge. Device poling processes are therefore based on measurements of simple slab waveguides using the measurement

techniques described above.  $T_p$  for each material is determined using the simple reflection technique as shown in Figure 3.5.

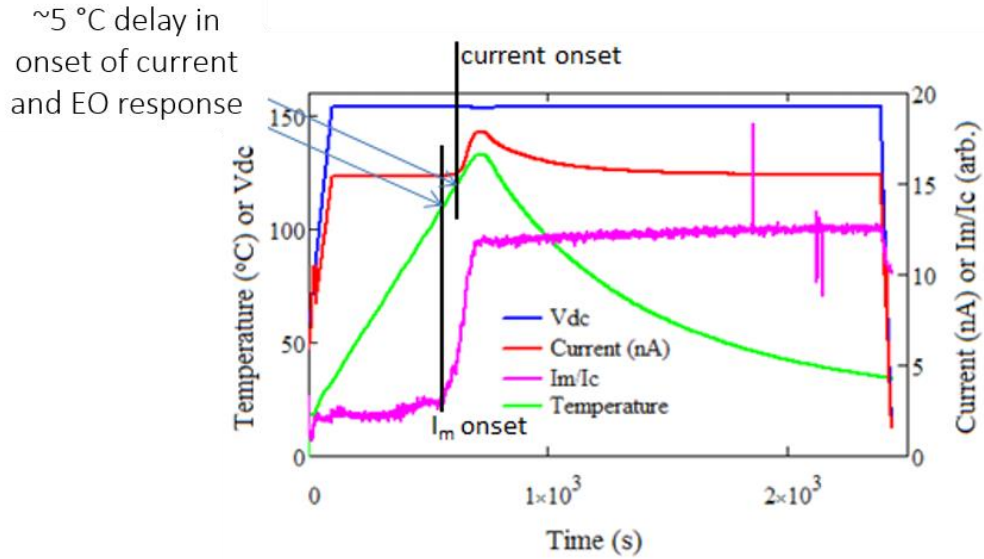


Figure 3.5: Sample poling trace from simple reflection technique in-situ EO activity measurement. Figure courtesy of Dr. Benjamin C. Olbricht.

The magenta curve  $I_m/I_c$  is a normalized optical response to a small modulation voltage overlaid onto the DC poling bias that is proportional to the EO activity. Estimated values of  $r_{33}$  can be extracted from this response, but more importantly, its relative value plotted against poling temperature is used to determine the lowest temperature at which maximum poling is achieved. Another notable trend in Figure 3.4 is the onset of a current spike that occurs within 5 °C of the EO activity spike. Because *in-situ* EO activity monitoring during modulator poling is unavailable, leak through current becomes the main feedback and a current spike near  $T_p$  is

expected during the poling process. Based on these measurements  $T_p$  for IKD-1-50 and SEO250 were determined to be 113 °C and 132 °C, respectively.

### 3.2.2 Modulator Poling

A poling apparatus was designed and built specifically for poling OEOM modulators. For precise temperature control of the OEOM during the poling routine a temperature controlled stage was built including a thermocouple that exactly replicates the layered polymer waveguide structure on a Si substrate. The thermocouple and modulator are seated on the heated stage and enclosed in an  $N_2$  environment for highest poling efficiency as shown in Figure 3.6. The modulator electrodes are contacted with spring loaded needle probes and the poling field is applied via a Keithley SourceMeter capable of sourcing 1100 V while providing nA precision current feedback.

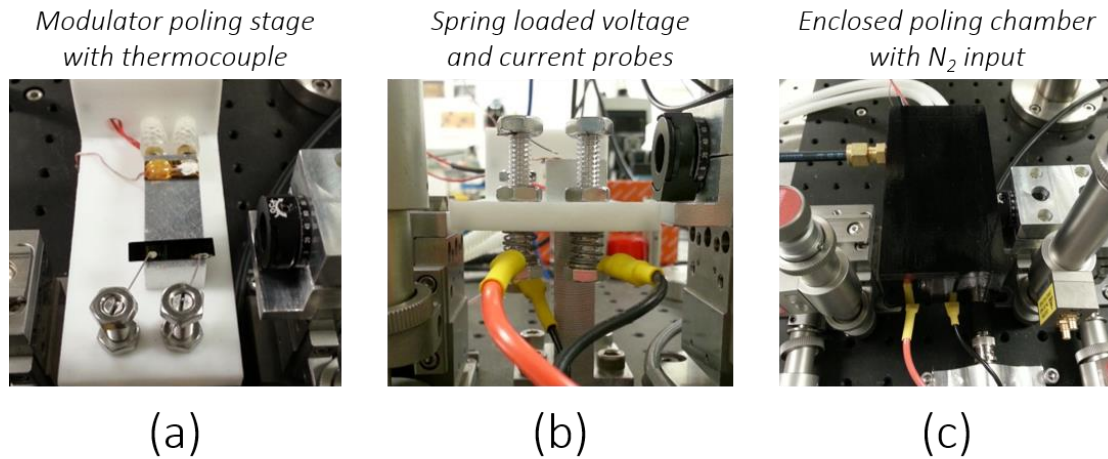


Figure 3.6: Modulator poling setup showing (a) thermocouple and contacted modulator, (b) spring loaded voltage and current probes and (c) enclosure with gas inlet for a  $N_2$  atmosphere.

The temperature controller, SourceMeter and N<sub>2</sub> valve are all interfaced with a CPU in LabVIEW to control the poling process. Once the stage is enclosed as shown in Figure 3.6 (c) a continuous flow of N<sub>2</sub> begins and the temperature and voltage are ramped up simultaneously at different rates such that the electric field peaks 90 seconds before T<sub>p</sub> is reached. The temperature soaks at T<sub>p</sub> for 30 seconds and then begins to cool to room temperature, once it reaches 30 °C and the chromophores are immobile the voltage ramps down to zero and the poling process is complete. A typical poling trace of an OEOM modulators is shown in Figure 3.7.

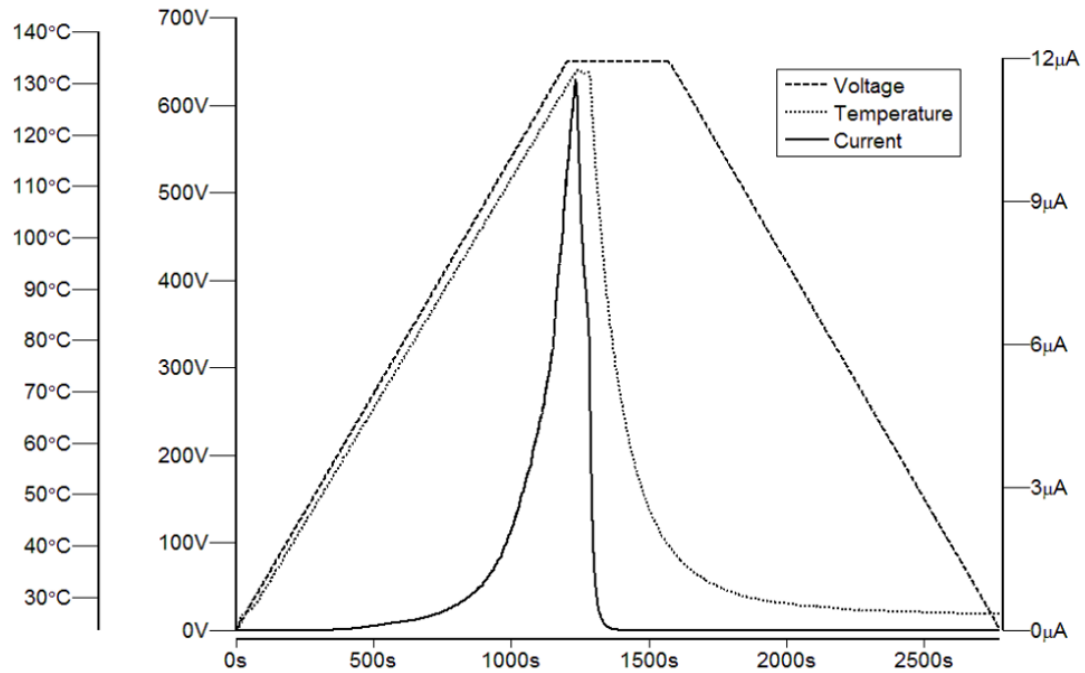


Figure 3.7: Modulator poling trace for an SEO250 device showing temperature, applied voltage and leak through current.

Electrical shorting is a persistent challenge during modulator poling. Shorting was frequently observed for a variety of reasons including: defects in the polymer films that were sometimes caused by the needle probes; ground plane and top electrode proximity resulting in fields greater than 3 V/ $\mu\text{m}$ , the dielectric breakdown of air; and high field concentrations at sharp corners on the poling electrode. The needle probe damage was corrected for by applying a conductive colloidal silver paste to the poling contact pad to provide a more robust contact point. Dielectric breakdown of air was avoided by ensuring that the poling electrode was patterned sufficiently far from the edge of the sample where the ground plane was exposed between the polymer and Si substrate. High field concentrations were minimized by designing the electrode contact as an ellipse to decrease the number of geometrical corners. With these modifications and by keeping poling fields to below 100 V/ $\mu\text{m}$  the modulator poling process became reasonably reliable with fewer than 20% of devices shorting during poling.

### 3.3 Phase Modulation Testing

Measuring phase modulation is challenging because optical measurements are limited to square law detectors, meaning only the time averaged power of an optical signal can be recorded. This means that for a phase modulated optical field of the form

$$\mathbf{E} = \mathbf{E}_0 e^{j(\beta_0 L + \Delta\phi)} \quad (3.1)$$

all that can be measured directly is

$$P_{ave} = \text{Re}(\mathbf{E}_0 e^{j(\beta_0 L + \Delta\phi)} \cdot \mathbf{E}_0^* e^{-j(\beta_0 L + \Delta\phi)}) = |\mathbf{E}_0|^2 \quad (3.2)$$

and the phase information is lost. Phase modulation measurement therefore requires an approach that transforms the phase modulation into amplitude modulation. A simple but cumbersome method for doing this is to build a Mach-Zehnder interferometer that

splits the incoming optical beam into two equal components, sends one through the modulator to impart a phase shift, and then recombines them to produce amplitude modulation via constructive and destructive interference. A simpler method is to translate the phase modulation into a polarization rotation and pass the resultant beam through a linear polarizer to achieve amplitude modulation. A polarization rotation measurement was used to characterize the OEOM phase modulators as described below.

### 3.3.1 Polarization Rotation Method

The polarization rotation method operates based on varying phase shifts imparted on the vertical and horizontal components of a 45° polarized input mode. Analysis of this technique is easily described by Jones matrices, which track the horizontal and vertical field components perpendicular to the direction of propagation in a 2×1 vector:

$$\mathbf{E} = \begin{bmatrix} E_h \\ E_v \end{bmatrix}, \quad (3.3)$$

where  $E_h$  and  $E_v$  are horizontal and vertical field components, respectively. In general,  $E_h$  and  $E_v$  are complex and include phase information, but for this discussion we will assume that the components of the mode launched into the modulator are in phase and of equal amplitude, *i.e.* the mode is linearly polarized at 45°

$$\mathbf{E}_{in} = \frac{1}{\sqrt{2}} \begin{bmatrix} 1 \\ 1 \end{bmatrix}. \quad (3.4)$$

As the light traverses a TM modulator, the vertical modulation field induces an unequal phase shift in the vertical and horizontal field components as a result of  $r_{33}$  and  $r_{13}$  modulation, which can be represented as:

$$M_{TM} = e^{j\Delta\phi_0} \begin{bmatrix} e^{j\Delta\phi_h} & 0 \\ 0 & e^{j\Delta\phi_v} \end{bmatrix}, \quad (3.5)$$

where  $\Delta\phi_h = -\frac{1}{2}\beta_0 n_0^3 r_{13} \frac{V}{d} \Gamma L$  and  $\Delta\phi_v = -\frac{1}{2}\beta_0 n_0^3 r_{33} \frac{V}{d} \Gamma L$  as stated in Equation 2.19.

As the modulation voltage is increased the phase difference between the horizontal and vertical components increases due to the difference between  $r_{33}$  and  $r_{13}$ . The light therefore rotates from a linear polarization at  $45^\circ$  to an elliptical polarization with its major axis between  $45^\circ$  and  $-45^\circ$  until reaching the next linearly polarized state at  $-45^\circ$ . This is shown in Figure 3.8.

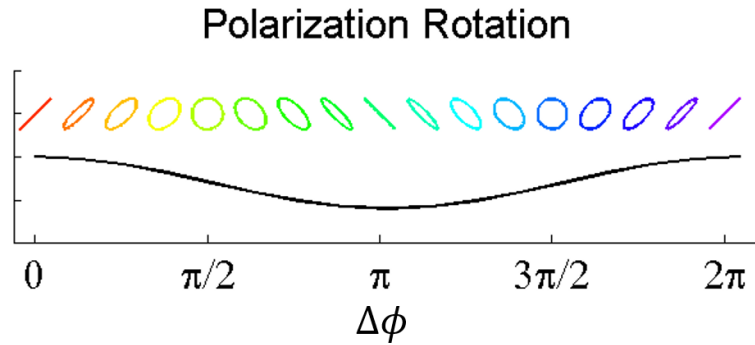


Figure 3.8: Polarization rotation with increasing phase difference between the horizontal and vertical field components. The colored shapes represent the polarization state as  $\Delta\phi$  increases, the black line is the output intensity cosine curve.

After leaving the modulator the light is focused by a lens, through a polarizer oriented at  $45^\circ$  onto a photodetector resulting in amplitude modulation as the polarization rotates into and out of the axis of the polarizer. The polarizer is represented as

$$P_{45^\circ} = \frac{1}{2} \begin{bmatrix} 1 & 1 \\ 1 & 1 \end{bmatrix}. \quad (3.6)$$

The linearly polarized light leaving the polarizer towards the photodetector can then be calculated as

$$\mathbf{E}_{out} = P_{45^\circ} \cdot M_{TM} \cdot \mathbf{E}_{in} = \frac{1}{2\sqrt{2}} e^{j\Delta\phi_0} \begin{bmatrix} e^{j\Delta\phi_h} + e^{j\Delta\phi_v} \\ e^{j\Delta\phi_h} + e^{j\Delta\phi_v} \end{bmatrix} \quad (3.7)$$

and the intensity measured on the photodetector is

$$I_{out} = \mathbf{E}_{out}^* \cdot \mathbf{E}_{out} = \frac{1}{2} [1 + \cos(\Delta\phi_h - \Delta\phi_v)]. \quad (3.8)$$

The output intensity is therefore dependent on the difference in phase shift between the horizontal and vertical components

$$\Delta\phi_{45^\circ} = \Delta\phi_h - \Delta\phi_v = \frac{1}{2} \beta_0 n_0^3 (r_{13} - r_{33}) \frac{V}{d} \Gamma L. \quad (3.9)$$

Note that the horizontal component phase shift is a factor only because of the  $45^\circ$  polarized input light. In a purely TM phase modulator, only vertically polarized light will be launched and there will be no counteracting horizontal phase shift from  $r_{13}$  modulation. To account for this, the experimentally verified approximation that  $r_{13} \approx \frac{1}{3} r_{33}$  is used to back out a pure TM modulator  $V_\pi$ . Plugging this approximation into Equation 3.9 we find

$$\Delta\phi_{45^\circ} = -\frac{1}{3} \beta_0 n_0^3 r_{33} \frac{V}{d} L \quad (3.10)$$

and by setting Equation 3.10 equal to  $\pi$  and solving for  $V$

$$V_{\pi,45^\circ} = \frac{3d\lambda}{2n_0^3 r_{33} \Gamma L}. \quad (3.11)$$

Comparison with Equation 2.20 for pure TM phase modulation

$$V_{\pi, TM} = \frac{d\lambda}{n_0^3 r_{33} \Gamma L}$$

yields the relationship

$$V_{\pi,45^\circ} = \frac{3}{2} V_{\pi, TM}. \quad (3.12)$$

Therefore when reporting  $V_{\pi}$  values acquired from the polarization rotation technique, the measured values are multiplied by a factor of  $2/3$  to reflect the expected TM operation.

### **3.3.2 DC Phase Modulation Measurement**

A testing setup implementing the polarization rotation measurement was designed and built. The input light is launched with a  $2.5\ \mu\text{m}$  lensed fiber oriented at  $45^{\circ}$  into the end facet of the modulator, which is seated on the same vacuum stage that was built for device poling. The output of the device enters a  $0.5''$  diameter rotatable optics tube containing the lens, polarizer and photodetector mounted on a translation stage to align with the output of the modulator for maximum photodetector illumination. The output of the photodetector is sent to a transimpedance amplifier to convert the photocurrent to a voltage and then read on an oscilloscope. A diagram and photograph of the testing set up are shown in Figure 3.9 (a) and (b), respectively.

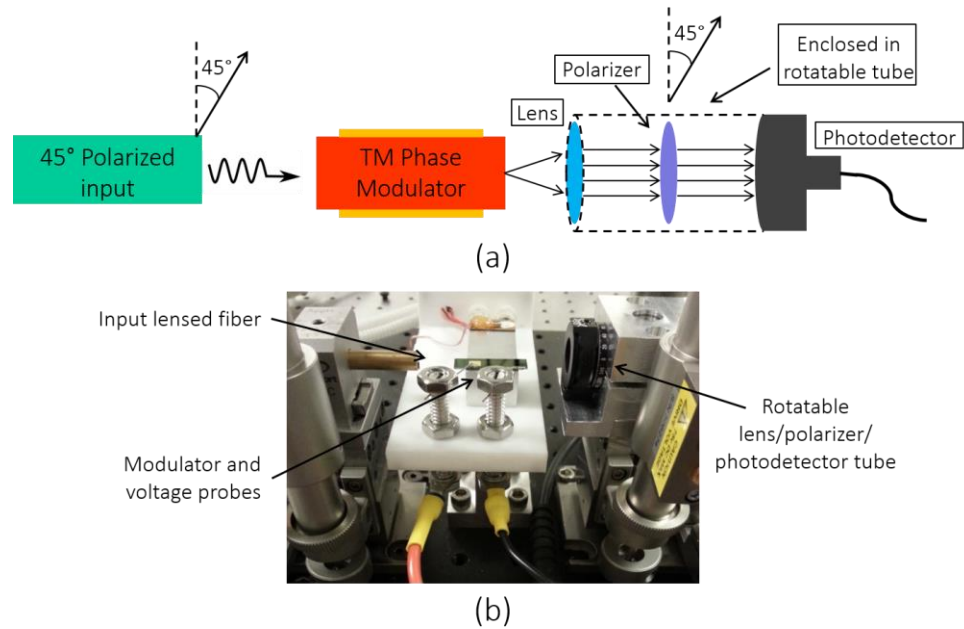


Figure 3.9: (a) Polarization rotation measurement setup diagram. (b) Picture of lab setup for polarization rotation phase modulator testing.

A symmetric triangle voltage function at 1 kHz was applied to the modulator electrode, and  $V_{\pi,45^\circ}$  values were found by measuring the voltage necessary to impart a  $\pi$  phase shift, which corresponds to a peak to trough oscillation of the cosine in Equation 3.8. An example oscilloscope trace showing the modulation voltage and optical response from the photodiode is shown in Figure 3.10.

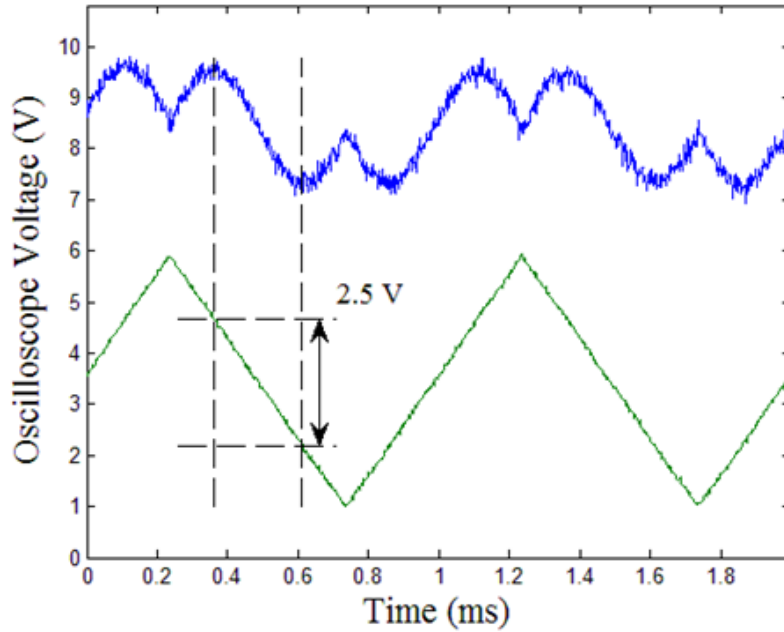


Figure 3.10: Polarization rotation phase modulation measurement trace.

IKD-1-50 and SEO250 based phase modulators were characterized and  $V_\pi$ 's down to around 2 V were measured for these 16 mm interaction length devices, resulting in a  $V_\pi L$  of 3.2 V·cm. This is a large improvement over the  $V_\pi L$  of 17.2 V·cm previously demonstrated in LiNbO<sub>3</sub> modulators that had a  $V_\pi$  of 8.6 V for a 2 cm long interaction length [23]. While previously demonstrated OEOM based modulators have shown  $V_\pi L$  values far lower than this by implemented nano-slot waveguide or photonic crystals [35], [39], the simplified and lower resolution fabrication required for these devices enables longer interaction lengths for lower drive voltages. Indeed several iterations of SEO250 devices with longer interaction lengths of 25 mm were also fabricated for even more efficient operation that demonstrated  $V_\pi$ 's down to 1 V.

From the measured  $V_\pi$  values an estimated  $r_{33}$  is backed out based on Equation 2.20. To account for fabrication variations the waveguide dimensions are measured

with a scanning electron microscope and used to numerically calculate a value for the overlap integral  $\Gamma$  and also to give the electrode gap  $d$ . A summary of results from the most efficiently poled IKD-1-50 and SEO250 modulators are given in Table 3.3.

Table 3.3: DC Modulator results for IKD-1-50 and SEO250 modulators.

Core Material	Int. Length	Electrode Gap	$E_{pole}$	$V_{\pi}$	$r_{33}$
IKD-1-50	16 mm	7.5 $\mu\text{m}$	100 V/ $\mu\text{m}$	2.2 V	$\sim 75$ pm/V
SEO250	16 mm	6.5 $\mu\text{m}$	80 V/ $\mu\text{m}$	1.7 V	$\sim 110$ pm/V
SEO250	25 mm	7.5 $\mu\text{m}$	80 V/ $\mu\text{m}$	1.0 V	$\sim 100$ pm/V

A general trend of increasing  $r_{33}$  with poling field was observed but many devices underperformed due to several factors such as device defects, solution age and suspected poling field damage to the waveguide core. However, optimization of the poling process yielded several devices, including the ones listed in Table 3.3, that demonstrated near 100% poling efficiency, yielding  $r_{33}$  values equal to or greater than was predicted by the simple slab devices. As the field progresses studies of in-device poling efficiency continue, but  $r_{33}$ 's from 70–100 pm/V were regularly achieved, offering more than twice the EO activity of LiNbO<sub>3</sub>. The increased  $r_{33}$  as well as the improved field overlap and decreased electrode gap resulted in measured drive voltages significantly lower than are found in LiNbO<sub>3</sub> modulators.

Optical loss measurements were taken and referenced to fiber-to-fiber throughput to evaluate the total insertion loss. Loss values on the order of -13 dB were measured for the 16 mm interaction length devices. The high loss results from a variety of factors including poor overlap with the coupling fibers, inconsistent end facet preparation, mode leakage into the ridge slab and material loss. Further optimization of the waveguide parameters could be done to better match with optical

fiber modes and to improve lateral index contrast to minimize slab mode leakage. Additionally UV15 has been reported to have high material loss at 1550 nm [65]. A different cladding material with lower loss would improve the loss figure and could likely be easily integrated into this simple modulator structure.

### 3.4 Conclusion

In the previous sections the design, fabrication and characterization of DC OEOM phase modulators were discussed. A fabrication routine that does not damage the core OEOM material was developed and poling routines to induce high EO activity into two different OEOMs were optimized. The result of these efforts is a phase modulator with a lower  $V_{\pi}L$  than existing LiNbO<sub>3</sub> modulators. The next goal for these devices is operation at RF frequencies up to 50 GHz. The electrode configuration on the DC devices is a vertically oriented lumped element capacitor. To effectively modulate at RF frequencies this electrode needs to be redesigned as a microstrip transmission line that will apply the same vertically oriented modulation field while also impedance matching to a feed circuit and efficiently transferring the signal energy into an EO modulation response. This RF design requires knowledge of the RF properties of the materials being used. The following chapter will discuss a novel RF material characterization technique that will enable further high frequency device design.

## Chapter 4

### RF DIELECTRIC CHARACTERIZATION OF THIN FILMS

High frequency operation is achieved via a traveling wave modulator design in which a transmission line is built around an optical waveguide. The three main design considerations for an efficient traveling wave modulator are impedance matching with the feed probe or circuit, wave velocity matching between the optical and RF mode and minimal RF transmission loss. For well-informed design it is therefore necessary to know the dielectric and attenuation constants of the materials being used at the intended frequencies of operation, in this case 0–50 GHz.

#### 4.1 RF Dielectric Constant Characterization Techniques

Most materials used in OEOM waveguides have been characterized in the optical domain by methods such as the attenuated internal reflection technique and variable angle spectroscopic ellipsometry [66]. These techniques are performed on simple thin films on the order of a few microns and are optically probed via free space or prism coupling. Characterization at RF frequencies requires completely different measurement techniques with a fabricated structure to launch and confine the RF field into the material under study. To this end, there are many established techniques for confining RF energy into a material and extracting dielectric properties from the measured response such as substrate integrated cavities, open-ended straight resonators and ring resonators [67]–[69].

Substrate integrated cavities, or rectangular cavity resonators, are enclosed cavity resonators that fully confine the energy to the material within the metallic walls of a three dimensional enclosure [69], [70]. The resonances within this structure vary with frequency and are dependent on the dielectric properties of the substrate and can therefore be analyzed to find an accurate value of the dielectric constant. A drawback of this technique is developing the fabrication process to build an enclosed cavity and to fill it with the material being investigated.

Linear and ring resonators can in general be implemented using any type of RF transmission line to guide the energy along a resonant path. The scattering parameters (S-parameters) of a resonant transmission line structure will show resonances wherever the path length is an integer multiple of the effective wavelength of the transmission line mode, summarized mathematically as

$$\frac{\lambda_{res}}{\sqrt{\epsilon_{eff}}} = \frac{L}{N}, \quad (4.1)$$

or equivalently for the resonant frequency as

$$f_{res} = \frac{c_0 N}{L \sqrt{\epsilon_{eff}}}, \quad (4.2)$$

where  $c_0$  is the speed of light in free space,  $N$  is the resonance number,  $L$  is the path length and  $\epsilon_{eff}$  is the effective dielectric constant of the mode. By measuring the resonances the effective dielectric constant of the transmission line mode can be extracted and compared with numerical or analytical calculations to extract the material dielectric constant  $\epsilon_r$ . The most commonly used transmission line for material characterization is the microstrip line. While microstrip lines do not fully confine the field to the material, as is done in a substrate integrated cavity, the field is highly confined to the substrate between the signal electrode and ground plane as can

be seen in the finite element solution for a thin film microstrip in Figure 4.1. Because of this high field confinement to the substrate  $\epsilon_{eff}$  is very close to  $\epsilon_r$  and less dependent on electrode thickness, which is a challenging parameter to control during a fabrication process due to uncertainty in electroplating rates.

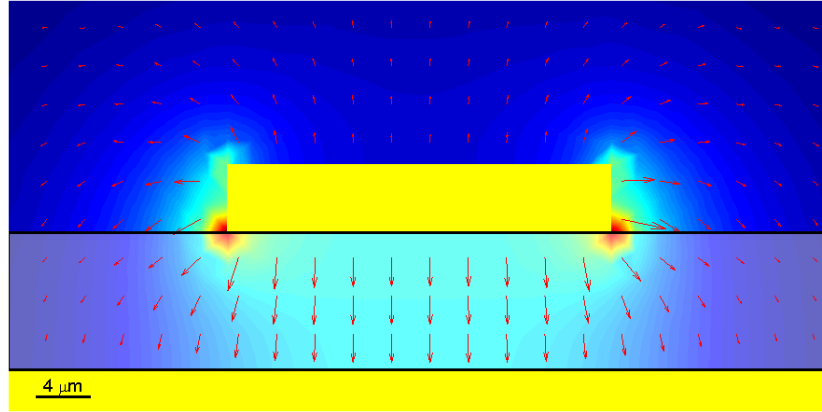


Figure 4.1: Electric field of a microstrip transmission line. The field magnitude is represented in the heat map and the field vectors are shown as red arrows.

Open-ended straight microstrip resonators are the simplest method to carry out this type of measurement, however variations in probe position and fringing fields at the open ends of these structures result in uncertainty in the path length  $L$  and effective dielectric constant  $\epsilon_{eff}$ , which can skew the extracted value of  $\epsilon_r$ . These drawbacks of open ended straight resonators are completely eliminated by the closed path of ring resonators. By coupling RF energy to the ring with a feed microstrip line the resonant characteristics of an unperturbed mode along a known path can be measured and  $\epsilon_r$  can be extracted.

Microstrip ring resonators (MSRRs) were therefore determined to be the optimal structure for extracting the dielectric constant. The path length of MSRRs is dictated only by the ring radius, and Equation 4.2 is therefore modified such that the length is the circumference of ring with radius  $r$

$$f_{res} = \frac{c_0 N}{2\pi r \sqrt{\epsilon_{eff}}} \quad (4.3)$$

By measuring resonances in rings with different radii the dielectric constant at discrete frequency points across a broad spectrum can be obtained.

There is a substantial body of work analyzing MSRR operation for material characterization and filtering applications [67], [68], [71]–[73], however like all of the measurement techniques previously mentioned these procedures were designed for characterizing traditional RF substrates with thicknesses on the order of 100’s of  $\mu\text{m}$ . Unfortunately, OEOMs are synthesized on the milligram scale and film thickness of this size would require prohibitively large volumes of material. Maximum films are therefore limited to thicknesses on the order of 10  $\mu\text{m}$ . The dimensional constraint of these materials introduces new challenges related to coupling to the ring and increased propagation loss. To address these issues it was necessary to modify the traditional RF material characterization techniques to thin film substrates, *i.e.* 10  $\mu\text{m}$  and below.

## 4.2 Thin Film Microstrip Ring Resonators

Thin film MSRRs were designed for 10  $\mu\text{m}$  thick films of an arbitrary polymer material. The goal of the measurement was to ascertain an accurate value for  $\epsilon_r$ , but it was assumed that the value would be between 2–5 based on the optical indices and the expected low dispersion of polymers [34]. The feed microstrip width was therefore chosen to be 28  $\mu\text{m}$  to maintain an impedance close to 50  $\Omega$  for good matching with

RF probes. The ring microstrip width is decreased to 13  $\mu\text{m}$  to minimize path length difference between the inner and outer ring diameter which could introduce measurement error [67], [74], [75].

#### 4.2.1 Coupling to the Ring Resonator

The major challenge for thin film MSRRs is coupling from a feed line into the ring resonator with sufficient power that a resonant response can be measured. With conventional thicker substrates this coupling is simply achieved with a terminated microstrip line a short distance from the outer edge of the ring as shown in Figure 4.2.

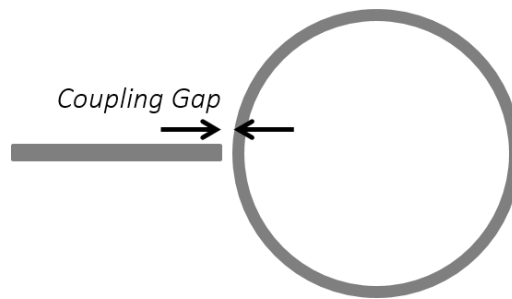


Figure 4.2: Traditional microstrip ring resonator with terminated feed line coupling.

The proximity of the rings outer diameter and the fringing field of the terminated feed line provides adequate lateral coupling for a resonance measurement. Thin film MSRRs suffer from a variety of factors that make this simple coupling method inadequate. First, the proximity of the signal electrode and ground plane results in a more tightly confined mode and substantially diminishes the fringing field that would laterally couple to the ring. Additionally, the miniaturized dimensions for a 50  $\Omega$  feed line mean a narrower strip width, and the aspect ratio of the electrode height

and coupling gap introduce fabrication limitations on the strip thickness. These factors combine to yield a smaller cross sectional coupling area, further decreasing the power transferred to the ring. The power coupling issues are compounded by the larger propagation loss of thin film microstrips [76], [77], which increases the coupled power required for a resonance measurement. As a result of these limiting factors in thin film MSRRs a modified approach for coupling energy into the ring was required.

#### 4.2.2 Arc Coupler Design

To achieve adequate power coupling for a resonance measurement an arc coupler was implemented. The coupler consists of a concentric arc that maintains a constant distance from the outer diameter of the ring resonator as shown in Figure 4.3.

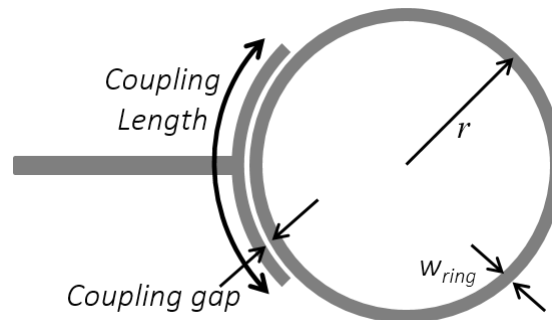


Figure 4.3: Thin film microstrip ring resonator with arc coupler.

The arc increases the cross sectional coupling area between the feed and the ring, and allows for directional coupling of the tightly confined mode given a sufficient coupling length across a small coupling gap. While the arc coupler increases the power transferred to the ring, it can also perturb the field traveling around the circumference of the ring. A field perturbation in the presence of the coupler would

slightly alter the phase velocity of the microstrip mode and could result in shifting the resonant frequency. The coupling length was therefore designed to optimize energy coupling while minimizing error arising from perturbations to the resonant characteristics of the MSRR.

The coupling of the microstrip transmission line to the MSRR is strongly dependent on the coupling gap and length, both shown in Figure 4.3, and also the electrode thickness. The coupling gap was chosen to be 5  $\mu\text{m}$  which was determined to be the minimum gap achievable without significantly increasing the risk of shorting between the coupler and the ring during electroplating. Thicker strip heights significantly improve the lateral coupling to the ring and do little to perturb the microstrip mode, which is largely confined in the substrate beneath the strip. It was therefore chosen to be in the range of 5–8  $\mu\text{m}$ , which is easily achieved with moderately thick electroplating resists and relaxes the requirement for precise electroplating thickness control.

Determining the optimal coupling length required a deeper investigation to find the correct tradeoff between power coupled and mode perturbation. The coupling length was studied numerically using Ansoft's high frequency structural simulator (HFSS) finite element electromagnetic simulation software. Coupling strength was evaluated by examining the total output power of a straight microstrip line that is fed with a T-coupling structure as shown in the inset of Figure 4.4. It was determined by comparison with an arc coupler to a half-ring that the curvature of radii down to 1.3 mm is low enough that the coupling characteristics are accurately portrayed by the straight T-coupling structure.

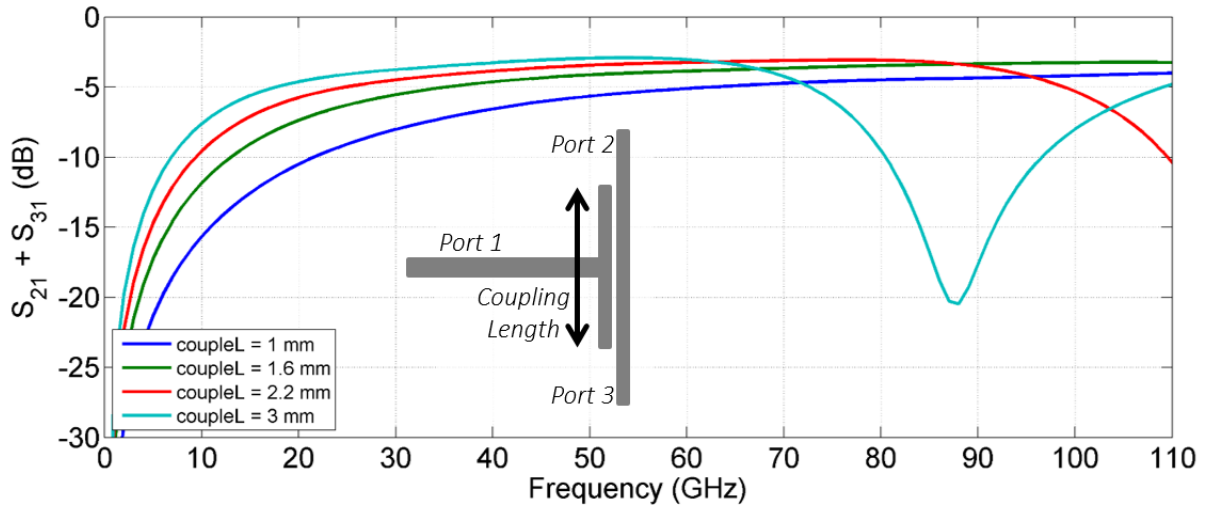


Figure 4.4: T-coupler power output and coupler structure (inset).

Analysis of output power from this structure showed sufficient coupling,  $> -10$  dB from 30–110 GHz, for coupling lengths from 1–1.6 mm. However, as the coupling length approaches the effective wavelength of the microstrip mode, a resonance that results in antenna-like radiation is induced and severely diminishes the power coupled to the output microstrips. This can be seen in Figure 4.4 for coupling lengths of 2.2 and 3 mm. From 0–40 GHz coupling lengths up to 5 mm can be safely implemented without inducing resonance.

With the required coupling lengths for adequate power coupling determined, the couplers loading effect on the ring resonance was also investigated using HFSS. The study was done for a single feed device in which only  $S_{11}$  reflection measurement are taken as shown in Figure 4.5, however the results are also valid for dual feed throughput structures for measuring  $S_{12}$ .

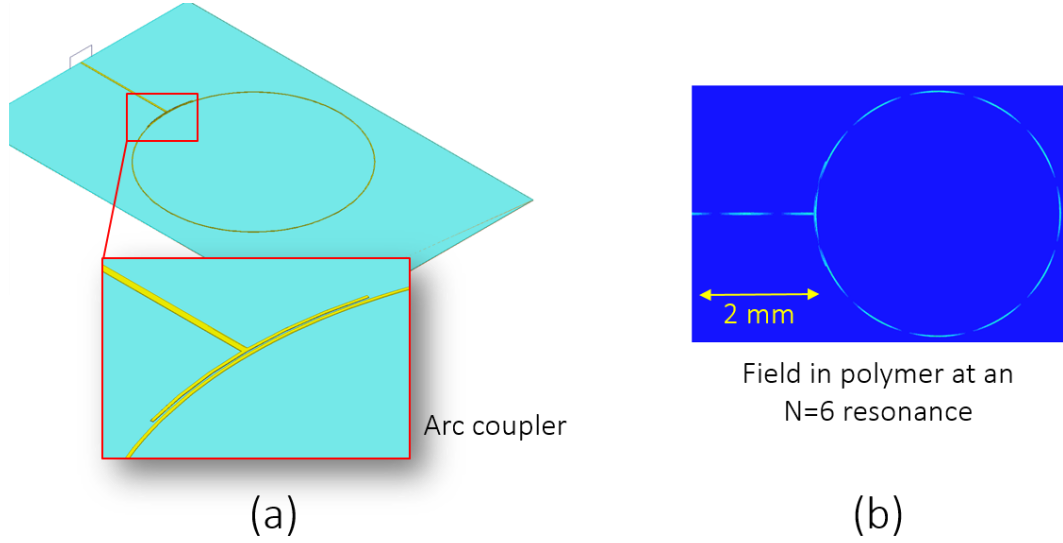


Figure 4.5: (a) MSRR with arc coupler model in HFSS. (b) Field profile in polymer.

The loading effect of the coupler was characterized with the following analysis. First, the feed microstrip, coupler, and ring resonator were modeled across the desired frequency range with 100 MHz resolution and the output S-parameters were extracted. From the resonant dips observed in the S-parameters,  $\epsilon_{eff,ring}$  was calculated at each resonant frequency according to Equation 4.3 solved for  $\epsilon_{eff}$

$$\epsilon_{eff,ring} = \left( \frac{c_0 N}{2\pi r f_{res}} \right)^2. \quad (4.4)$$

These values were then compared to frequency dependent, numerically calculated values,  $\epsilon_{eff,straight}$ , for an identical microstrip cross section and dielectric constant as that of the modeled ring. Comparison of  $\epsilon_{eff,ring}$  extracted from the S-parameters, and  $\epsilon_{eff,straight}$  calculated directly from the microstrip dimensions provides a quantitative evaluation of the error introduced by the coupler, as well as the

error present in standard MSRR measurements such as ring curvature and inductance across the ring diameter. Figure 4.6 shows an example of the resonance error analysis.

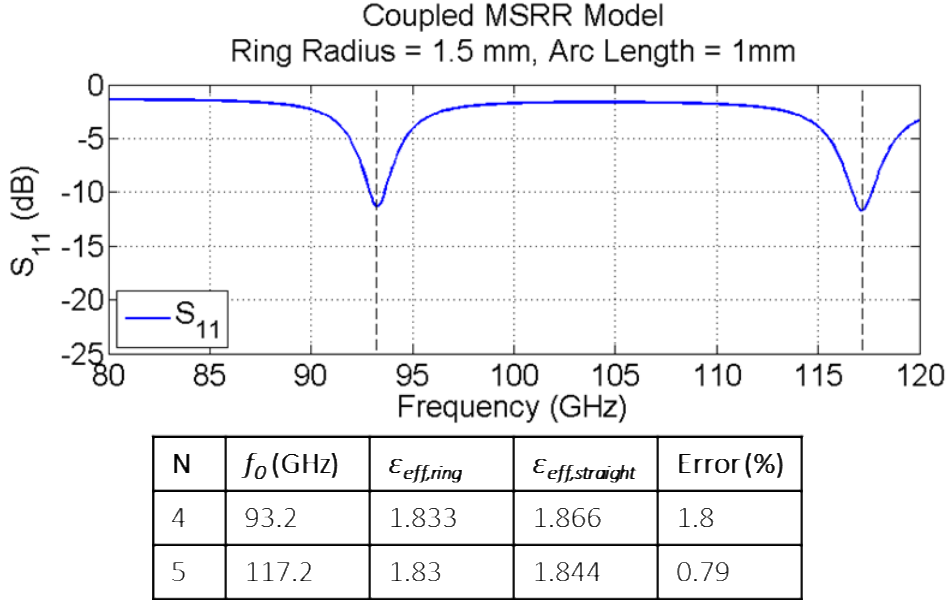


Figure 4.6: MSRR arc coupler resonance error modeling and analysis.

Extensive simulations were performed for ring radii varying from 1–5 mm and coupling lengths from 1–5 mm in different frequency regimes. Above 40 GHz in rings with radii from 1.3 to 3 mm, coupling lengths up to 1.6 mm shifted loaded  $\epsilon_{eff}$  by less than 2% compared to  $\epsilon_{eff}$  calculated for a straight cross section. Below 40 GHz, in  $r = 5$  mm rings, coupling lengths up to 5 mm were found to shift resonances slightly more, but still resulted in less than 4%  $\epsilon_{eff}$  error. Shorter couplers were preferred to minimize the likelihood of fabrication errors along the coupling length, but larger coupling lengths were used for bigger rings to compensate for the longer circumference that results in larger total propagation loss.

Based on the results of the arc coupler analysis and the Equation 4.3 for resonant frequency as a function of ring radius a variety of ring sizes and coupling lengths were chosen to probe different frequency ranges. To ensure high measurement accuracy, resonance orders of  $N \geq 4$  were used for the smaller ring measurements at higher frequencies. Choosing higher resonance orders limits dispersion due to bending of the ring structures by minimizing the wavelength compared to the ring curvature. At these higher order resonances the curved line more closely mimics the straight section of microstrip that will be used for comparison to extract  $\epsilon_r$ .

The preference for higher order resonances, however, presents a problem at frequencies below 40 GHz. At these frequencies very large rings are needed to probe with higher order resonances as can be seen from the relationship between radius, resonance number and resonant frequency:  $f_0 \propto N/r$ . For example to measure an  $N = 6$  resonance at 20 GHz would require a ring radius of more than 8 mm. Larger radius rings are more susceptible to fabrication defects across the larger area, require more material and suffer from larger total propagation loss around the circumference which degrades or even eliminates the resonant signature. The lowest frequency data are therefore the  $N = 2-5$  resonances from an  $r = 5$  mm ring and are accordingly subject to slightly larger measurement error, but showed little variation from the higher order resonant measurements as will be shown in a following section. Table 4.1 shows the ring radii and coupling lengths that were implemented on UV15 MSRRs for high frequency dielectric constant measurement.

Table 4.1: Radii and coupling lengths of UV15 MSRRs.

Radius (mm)	1.3	1.5	1.7	2	2.5	3	5
Coupling length (mm)	1, 1.5	1, 1.5	1	1, 1.2, 1.5	1, 1.5	1.5, 1.8	4.8

### 4.3 Thin Film MSRR Fabrication

The first MSRR structures were fabricated on 10  $\mu\text{m}$  thick films of UV15, the optical cladding material used in the OEOM phase modulator. UV15 was used while developing the fabrication process because it is plentiful and inexpensive compared with OEOMs. Its RF dielectric properties are also the most important for device design as it makes up  $> 80\%$  of the polymer waveguide that will be the substrate of the microstrip line in the high frequency modulator.

MSRRs were fabricated on a Si substrate with a 3  $\mu\text{m}$  thick electroplated Cu ground plane purchased from IMAT, Inc. (WA), capped with a Ti/Au layer of 20 nm and 100 nm, respectively, by electron beam evaporation. The resonators are probed at a CPW contact point at the input of the feed microstrip, which will be further discussed in Chapter 5. Ground contact is made through exposed Au pedestals electroplated up from the ground plane on either side of the microstrip signal contact pad prior to the substrate layer deposition. The pedestals are patterned in a 6  $\mu\text{m}$  layer of NR2-8000P, spin deposited at 4000 rpm for 45 seconds, followed by a 150  $^{\circ}\text{C}$  bake for 60 seconds. The pattern is exposed with 250  $\text{mJ}/\text{cm}^2$  of 365 nm light, post exposure baked at 100  $^{\circ}\text{C}$  for 60 seconds and then developed in RD6. The exposed ground plane areas are further cleaned with an  $\text{O}_2$  plasma to ensure uniform electroplating across the pedestal. The pedestals are then electroplated in Techni-Au 25 ES RTU at 60  $^{\circ}\text{C}$  with 2 mA of current and a 300 rpm spin bar for 30 minutes which results an Au thickness of  $\sim 5$   $\mu\text{m}$ . Precise plating thickness control is very

challenging due to the variability in plating area at the contact point. Fortunately the pedestal height is not a crucial parameter and serves only to bring the ground plane closer to the polymer surface for ground-signal-ground (GSG) contact probes. The resist is removed in resist remover RR41, an acetone, methanol, isopropanol rinse and an O<sub>2</sub> plasma followed by a 100 °C bake to remove the RR41 residual. The result of this step is shown schematically in Figure 4.7 (a).

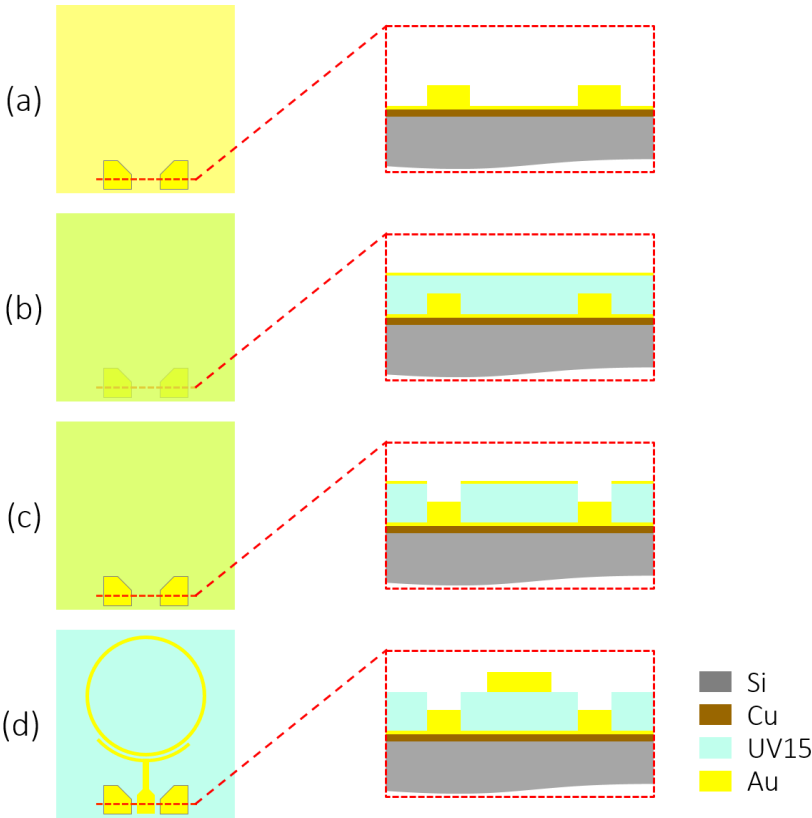


Figure 4.7: MSRR fabrication process. (a) Via pedestals electroplating. (b) Substrate deposition and curing. (c) Via pedestal exposure. (d) Microstrip feed and ring patterning and electroplating.

The 10  $\mu\text{m}$  thick UV15 layer is then spin deposited over the ground plane pedestals at 3000 rpm for 150 seconds and smoothed with a 100 °C bake for 60 seconds to ensure a flat surface over the pedestals. The film is then cured with a UV dose of 5 J/cm<sup>2</sup> at 365 nm, and a thermal cure at 110° C under vacuum for at least 12 hours. Once the film is cured a 30 nm electroplating seed layer of Au is deposited by e-beam evaporation as shown in Figure 4.7 (b). The Au layer serves not only as a seed layer for electroplating, but also as a buffer layer between the resist solvents and the polymer substrate.

The via pedestals are exposed for probe contact with a pattern and dry etch step. A 10  $\mu\text{m}$  thick layer of NR2-8000P is deposited at 2350 rpm for 40 sec followed by a 12 minute bake at 100 °C. This prebake temperature is lowered from 150 °C and increased in duration to minimize cracking that results from mismatches in the coefficient of thermal expansions (CTE) between the UV15 and resist. The resist is exposed with 460 mJ/cm<sup>2</sup> of 365 nm light, post exposure baked at 100 °C for 3 minutes and developed in RD6. The Au seed layer is locally etched with a commercial Au wet etch, and the pedestals are exposed with a low pressure, high bias O<sub>2</sub>/CF<sub>4</sub> ICP etch that provides highly direction etching for vertical trenches to the via pedestals. The parameters for this etch are listed in Table 4.2. The resist is then removed using the same cleaning process as was used for the pedestal electroplating. The result of this step is illustrated in Figure 4.7 (c) where the resulting ground contacts are a few  $\mu\text{m}$  from the surface of the polymer and are easily contacted with a GSG probe.

Table 4.2: Low pressure, high bias etch for via pedestal exposure.

Pressure	O <sub>2</sub> Flow	CF <sub>4</sub> Flow	ICP Power	Bias Power
0.67 Pa	30 sccm	3 sccm	500 W	300 W

With the ground plane contacts prepared all that remains is to add the microstrip structures. The feed microstrip, coupler and ring resonator are patterned in another layer of NR2-8000P deposited and exposed with the same procedure as was used for the via pedestals. The same electroplating process is then used transfer the top layer structure onto the polymer substrate in a 5  $\mu\text{m}$  Au trace. To prevent CTE mismatch cracking, the device is submerged and removed from the electroplating solution at room temperature, allowing the thermal cycle to occur gradually with the solution instead of removing it directly from a hot bath to the room temperature lab. The electroplating resist is removed in RR41 and  $\text{O}_2$  plasma with special attention given to removing the residual resist between the coupler and the ring. Finally the seed layer is removed, electrically isolating the coupler from the ring, as depicted in Figure 4.7 (d). SEM images of the ring and coupling gap, and the CPW contact point of a finalized UV15 MSRR is shown in Figure 4.8. (a) and (b), respectively.

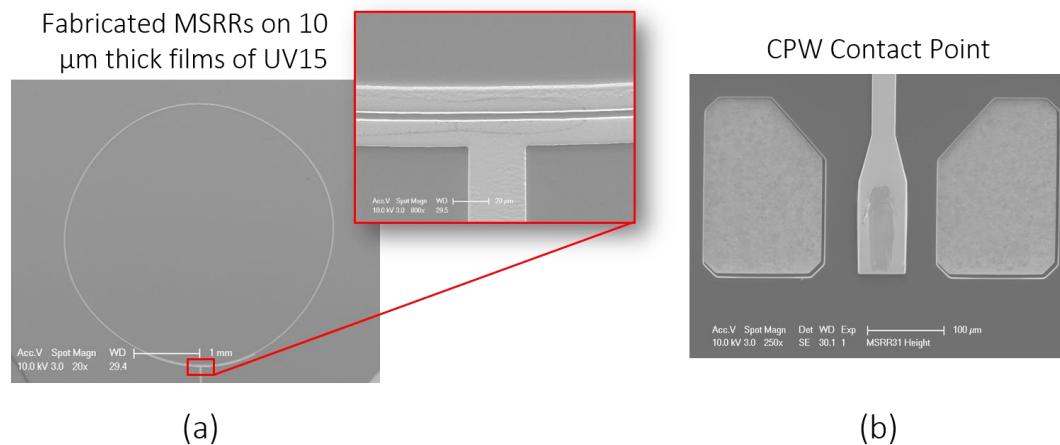


Figure 4.8: SEMs of fabricated MSRRs on UV15 showing (a) ring and arc coupler and (b) CPW contact point.

#### 4.4 Dielectric Constant Measurement

The completed UV15 MSRRs were characterized using an Agilent 8361C PNA. 100  $\mu\text{m}$  pitch GSG probes from Picoprobe with 50  $\Omega$  impedance were translated with micromanipulator probe holders to contact the feed microstrip contact pad and the ground plane pedestals. The probe is calibrated with a 1-port open, short, load CS-5 calibration substrate. A low reflection contact is observed by time domain measurements showing  $< 10$  dB  $S_{11}$  at  $t = 0$  indicating good impedance matching between the contact probe and the CPW contact point. Broadband  $S_{11}$  measurements are taken from 0–110 GHz with 1601 frequency points at a resolution of 68.7 MHz.

The relative dielectric constant  $\epsilon_r$  was extracted from these  $S_{11}$  measurements through a combination of calculated and measured values, summarized schematically in Figure 4.9.

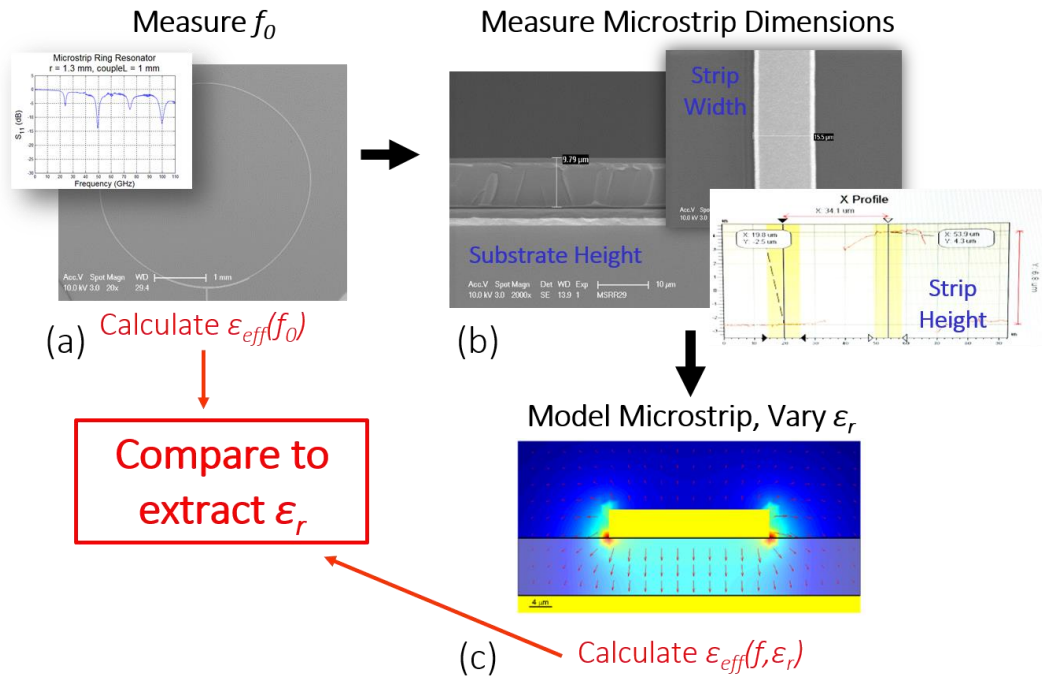
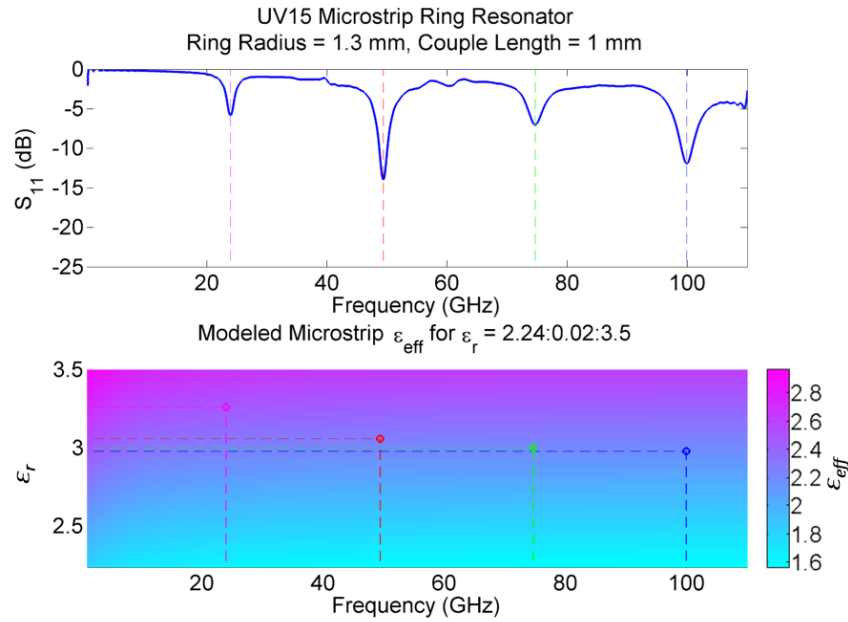


Figure 4.9: MSRR  $\epsilon_r$  extraction procedure. (a) Resonant frequencies from a fabricated ring are measured and  $\epsilon_{eff}$  is calculated. (b) The ring microstrip parameters are then measured and (c) plugged into an HFSS model to calculate  $\epsilon_{eff}$  for varying values of  $\epsilon_r$ . Comparison between the measured and calculated values of  $\epsilon_{eff}$  yield the dielectric constant of the material.

The resonant frequencies are determined from  $S_{11}$  responses like the one shown in the inset of Figure 4.9 (a). From these resonant frequencies values of  $\epsilon_{eff,ring}$  are calculated based on Equation 4.4. After  $S_{11}$  measurement, the physical dimensions of the device under test were determined. White light interferometry was used to measure the thickness of the microstrip lines and SEM imaging was used to find the substrate thickness and line width of the ring, shown in Figure 4.9 (b). The measured microstrip parameters are used in an HFSS model, shown in Figure 4.9 (c), to calculate  $\epsilon_{eff,straight}$  for an equivalent straight section of microstrip built on a

substrate with varying dielectric constant from  $\epsilon_r = 2.4$  to 3.5 by steps of 0.02. The measured values of  $\epsilon_{eff,ring}$  and calculated values  $\epsilon_{eff,straight}$  are then compared to extract the relative dielectric constant,  $\epsilon_r$ , at each resonant frequency. An example of this analysis for a 1.3 mm radius ring is shown in Figure 4.10.



$N$	1	2	3	4
$f_0$ (GHz)	23.933	49.37	74.67	99.90
$\epsilon_{eff}$	2.36	2.21	2.18	2.16
$\epsilon_r$	3.26	3.06	3.00	2.98

Figure 4.10:  $\epsilon_r$  calculation example showing measured resonances from which  $\epsilon_{eff}$  is calculated, and a heat map of numerically calculated  $\epsilon_{eff}$  for different values of  $\epsilon_r$ .

UV15 rings of varying size as listed in Table 4.1 were characterized to probe the dielectric constant at frequencies ranging from 10–110 GHz as shown in Figure

4.11. The data presented includes measurements from both  $S_{11}$  reflection only devices as well as some  $S_{21}$  through measurements taken on devices with input and output couplers and feeds. The addition of another coupling structure did not affect the accuracy of the measurement and is considered validation for the reflection only measurements. As was mentioned previously the data points for 40 GHz and above are calculated from  $N \geq 4$  resonances on smaller rings, and the lower frequency data is from  $N \geq 2$  resonances measured on a larger 5 mm radius ring.

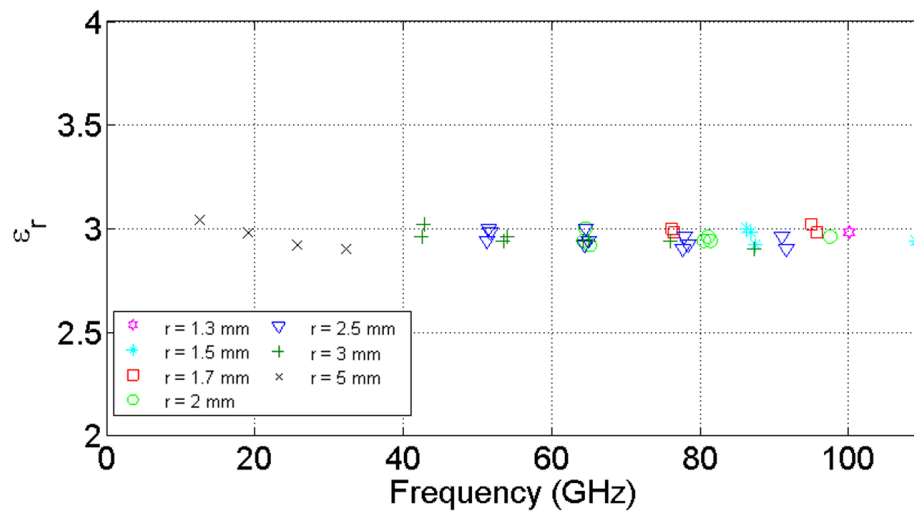


Figure 4.11: Extracted  $\epsilon_r$  of UV15 from 10 – 110 GHz measured with varying rings with radii ranging from 1.3 – 5 mm.

Multiple device iterations of rings with the same radius gave consistent values of  $\epsilon_r$  at their resonant frequencies with less than 3% variation from the mean. The measured values indicate that, as expected for a polymer [34], UV15 has very low frequency dispersion with a constant relative dielectric constant of  $2.97 \pm 0.07$ . This is

in excellent agreement with the room temperature value listed by the manufacturer of 2.96 at 1 MHz, further validating the measurement technique.

The MSRR technique was also performed on thin films of IKD-1-50. OEOM solutions are typically 3–8% solids and spun at 1200 rpm for  $\sim 1$   $\mu\text{m}$  thick layers, which is too thin for this measurement. For the MSRR measurement a dual deposition of a 13.5% solids solution at 850 rpm resulted in a total film thickness of 6.1  $\mu\text{m}$ . Some issues with film cracking and swelling during lithography occurred with the IKD-1-50 films which significantly lowered measurable device yield. However, a few small rings with 1.3 mm and 1.5 mm radii were characterized with  $N \geq 4$  resonances that indicated a similar relative dielectric constant of  $3.08 \pm 0.08$  from 70–110 GHz. Values below 70 GHz varied more widely up to  $\epsilon_r = 3.4$ . Further studies into the high frequency relative dielectric constant of OEOM materials were postponed due to the large volumes of material required and because the RF modulator being designed is  $> 80\%$  UV15 by volume meaning the RF characteristics of the device will be dominated by its dielectric characteristics. However, compiling a library of high frequency dielectric constants for various OEOMs is an important avenue of study that could be continued using this technique.

#### **4.5 Dielectric Loss Tangent Measurement**

Dielectric loss tangent,  $\tan\delta$ , can be characterized using resonant techniques such as MSRRs by analyzing the resonant quality factor and extracting individual loss factors [68], [70], [71], [74]. However, these techniques are greatly complicated by accounting for the coupling to the ring, which is highly variable in the thin film MSRRs as discussed in the previous section. To extract  $\tan\delta$  of UV15 a simpler method was used implementing straight microstrip lines fabricated on 10  $\mu\text{m}$  UV15

films, and measured using the same CPW probe contacts as were used for the MSRRs. There are three major factors that contribute to the transmission line attenuation: conduction loss, dielectric loss, and radiation loss due to surface roughness. These loss factors will be discussed more extensively in a subsequent chapter on traveling wave modulator design but it is necessary to mention them here for the purpose of material characterization. At lower frequencies, radiation losses due to surface roughness are minimal and electromagnetic transmission line theory suggests that conduction and dielectric losses scale with  $\sqrt{f}$  and  $f$ , respectively [78]. Thus, the total attenuation coefficient may take the form

$$\alpha_{tot} = \alpha_c + \alpha_d = a\sqrt{f} + bf, \quad (4.5)$$

in which  $a$  and  $b$  are constants corresponding to the conduction and dielectric loss. The total transmission loss can be extracted from the measured transmission parameter  $S_{12}$  by noting that

$$S_{12}^{dB} = 20 \cdot \log_{10}(e^{\alpha_{tot}L}) \quad (4.6)$$

and solving for  $\alpha_{tot}$  to be

$$\alpha_{tot} = -\frac{S_{12}^{dB}}{20 \cdot L} \ln(10) = -8.686 \cdot \frac{S_{12}^{dB}}{L} \quad (4.7)$$

in units of Np/m.

The total loss was measured on lines varying from 2.5–10 mm and fitted to Equation 4.5 using a least squares algorithm in MATLAB. Measurements were taken from 0–110 GHz, however the fitting was only applied to the data from 0–60 GHz, where the surface roughness radiation losses were minimal and Equation 4.5 is a more faithful representation of the dominant loss factors. The extracted values of  $a$  and  $b$  were then compared with analytical expressions for  $\alpha_c$  and  $\alpha_d$  to extract the

conductivity and loss tangent [78], [79]. Three different samples were characterized and the average  $\tan\delta$  for UV15 was found to be 0.015.

The extracted values of  $a$  and  $b$  were then used to calculate loss figures out to 110 GHz according to Equation 4.5 to compare with the measured results. The extrapolated loss calculated in this manner was found to underestimate the total measured attenuation at higher frequencies. This is understandable, as the operational frequency increases, particularly  $> 60$  GHz, the surface roughness of the film and electrodes become nontrivial in loss factor calculations and the simple expression for  $\alpha_{tot}$  listed in Equation 4.5 is no longer adequate. Better matching to the measured data was achieved by combining the extracted dielectric loss ( $\alpha_d = bf$ ) with analytical expressions for conduction loss that include surface roughness, conductivity, and microstrip dimensions [78], [79].

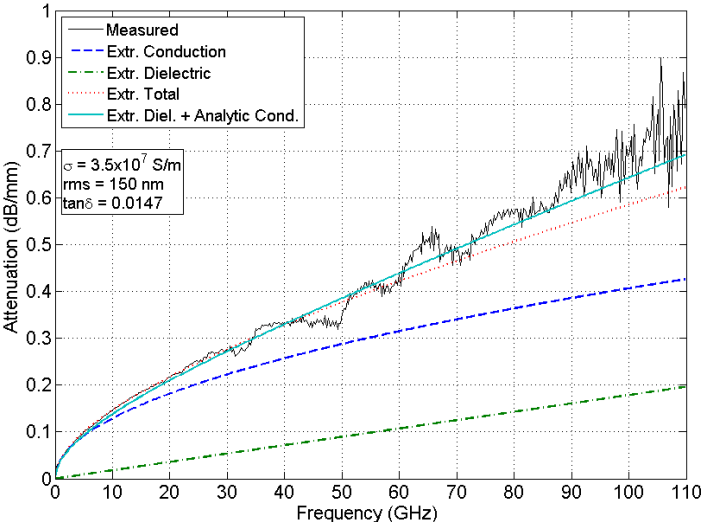


Figure 4.12: Measured, fitted and calculated microstrip loss and data. The best fit with the measured data is achieved by combining the extracted dielectric loss with calculated conduction loss that accounts for surface roughness.

For the calculated conduction loss the RMS surface roughness of the electroplated lines was measured by a Wyko interferometric profilometer to be approximately 150 nm. The analytical expression for conduction loss assumes a uniform conductivity for the signal electrode and ground plane. As was outlined in the MSRR fabrication section the ground plane in these devices were Cu/Ti/Au and the signal electrode is electroplated Au which is subject to impurities during the plating process that diminish the metal conductivity. Therefore, the conductivity was adjusted to match with the measured data and found, as expected, to be slightly lower than that of pure Au due to the Ti adhesion layer and the lower conductivity electroplated signal trace. The measured data matched well with calculations using  $\sigma = 3.5 \times 10^7$  S/m, about 15% lower than expected for pure Au.

Figure 4.12 shows the measured, fitted and calculated data. The dot-dashed, dashed, and dotted lines are extracted dielectric, conduction, and total losses, respectively according to Equation 4.5. The solid green line shows the sum of the extracted dielectric loss and calculated conduction loss including surface roughness and is the best fit to the measured data shown as the solid black line. It is apparent that conduction losses are almost twice as high as dielectric losses for these microstrips. This is expected and has been previously reported [76] and is thought to be due to the high field confinement, which results in larger currents flowing through the metal. The total attenuation coefficient of these lines was found to be less than 0.5 dB/mm below 70 GHz, which is adequate for use in microstrip traveling wave EO modulators.

#### **4.6 Conclusion**

RF characterization of thin films will be an important process as the field of OEOM modulators proceeds. The several orders of magnitude in scale between optical

and RF wavelengths have resulted in a dearth of RF techniques for optical scale devices and necessitated the modification of traditional measurements to attain the required dielectric information. Indeed this issue of scale is an enduring challenging in designing and fabrication microwave EO modulators where millimeter scale RF waves need to be confined to micrometer scale optical structures. The following chapters will discuss this challenge not only in modulator design but also in concise packaging for practical usage.

## Chapter 5

### HIG FREQUENCY MODULATOR DESIGN AND FABRICATION

#### 5.1 Traveling Wave Modulator Design

In Chapter 2 a low frequency OEOM based modulator was designed, and in Chapter 3 that modulator was fabricated and characterized to demonstrate higher in-device  $r_{33}$  and lower  $V_\pi$  values than have been observed in LiNbO<sub>3</sub> modulators. The other highly appealing attribute of OEOMs is their EO response at ultrahigh frequencies which has been measured into the THz regime [30]. Harnessing this wide bandwidth into EO modulators requires careful design in both the optical and RF frequency regimes. Whereas previously a constant modulation voltage across the electrode was assumed, we now will consider a high frequency modulation voltage of the form

$$V(z, t) = V_0 \sin\left(\frac{2\pi n_m}{\lambda_m} z - 2\pi f_m t\right), \quad (5.1)$$

where  $n_m$  is the effective index of the RF transmission line modulation mode,  $\lambda_m$  is the wavelength of the modulating wave,  $f_m$  is the frequency of the modulating wave, and  $z$  is the position along the length of the modulator. Efficient high-frequency operation requires consideration of RF loss, RF and optical wave velocity (index) matching, and modulation and poling field overlap. These design factors will be discussed in the following sections.

### 5.1.1 Impedance Matching and RF Loss

An obvious requirement for efficient EO modulation is the device's ability to focus RF energy from a source to the modulation electrode with minimal power loss. Impedance matching and RF attenuation are the two major factors that contribute to the energy that is transferred to the modulation field.

Impedance matching is often left out of the design equations for modulator efficiency, but it is what dictates the device dimensions. Chapter 4 commented on the impedance of thin film microstrip transmission lines and the miniaturized dimensions required to achieve the  $50\ \Omega$  standard for most RF connectors. The optical waveguides designed in Chapter 2 for low  $V_\pi$  modulators are  $6\text{--}8\ \mu\text{m}$  thick, with a dielectric constant of  $\sim 3$ , and require a signal trace of  $\sim 17\ \mu\text{m}$  for  $50\ \Omega$  operation. This is easily achievable with standard UV lithography, but requires a taper to a larger structure for contact with standard RF elements such as the  $50\ \Omega$  GSG probes used to probe the MSRRs in Chapter 4. The narrow, thin film microstrip lines were therefore tapered out to an  $80\times 80\ \mu\text{m}$  contact pad with ground plane vias on either side in the same configuration as shown in Figure 4.8 (b). The contact pad impedance is far from  $50\ \Omega$  but because of its short length compared to the modulation wavelength it has little effect on the transition from probe to microstrip line. This was demonstrated on the short lengths of microstrip used for loss characterization in Chapter 4. The S-parameters of a UV15 microstrip are shown in Figure 5.1 where the impedance-matched transition is illustrated by the  $S_{11}$  and  $S_{22}$  reflection parameters that remain below  $-10\ \text{dB}$  up to almost  $100\ \text{GHz}$ . This contact pad transition therefore transfers more than 90% of the input signal energy to the thin film microstrip and is adequate for feeding the traveling wave modulator.

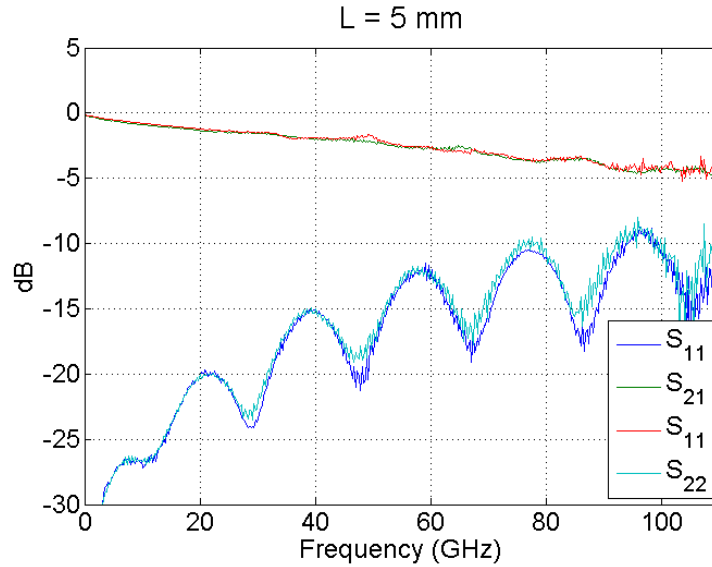


Figure 5.1: S-parameters for a thin film UV15 microstrip with the contact pad taper illustrating a well matched transition.

Attenuation of the modulating wave as it traverses the modulator is the second key factor in converting RF energy to the EO modulation. As mentioned in Chapter 4, as an RF signal travels down a transmission line energy is lost due to two major contributing factors: dielectric and conduction loss. Dielectric loss occurs in a material when the electromagnetic energy is converted to heat and dissipated rather than stored in the polarization oscillations of the constituent molecules of the material [80]. Dielectric loss in a microstrip transmission line is dependent on the inherent material loss tangent,  $\tan\delta$ , which is the ratio of energy lost to energy stored, and also the microstrip dimensions that dictate how much of the modulation field is confined to the material.

The dominant attenuation factor in thin film microstrips, however, is conduction loss, which results from the currents flowing through the ground and signal

electrodes of finite conductivity [81], [82]. Conduction loss can be intuited by considering the resistance seen by the current induced by the traveling wave. The resistance of a length of wire at low frequencies is given by the well-known formula  $R = \frac{\rho L}{A}$ , where  $\rho$  is the resistivity of the material,  $L$  is the length and  $A$  is the cross sectional area. In an RF transmission line the cross sectional area is determined by the width of the trace and how deep into the conductors the electric field penetrates and induces current. This penetration is parameterized by the skin depth  $\delta$ , which is the depth where the field amplitude decays by  $1/e$  and can be calculated to be [78]

$$\delta = \sqrt{\frac{2}{\omega \mu_0 \sigma}} = \sqrt{\frac{1}{\pi f \mu_0 \sigma}} \quad (5.2)$$

where  $\omega$  is the angular frequency and  $\sigma$  is the conductivity of the metal. (It is noted here that traditional notation assigns the character  $\delta$  to parameters associated with both dielectric and conduction loss, which is unfortunate.)

Evident from the resistance formula and Equation 5.2 are two conclusions: to minimize the conduction loss the electrodes should be at least one, and preferably several skin depths thick to allow for maximum field penetration and a large cross sectional area; and the skin depth's inverse relationship with  $\sqrt{f}$  results in a proportionality between the resistance and the square root of the frequency, shown in Equation 4.5 for fitting the measured attenuation to conduction and dielectric loss components. Conduction loss is also directly related to the square of the current amplitude as we might expect from the DC current power loss,  $P = I^2 R$ . Thin film microstrips for EO modulators have high field confinement by design for the strongest possible modulation field. However, these strong fields also induce large currents that increase conduction loss.

These concepts have been thoroughly investigated [79], [81]–[85] and rigorous closed form solutions that account for skin depth penetration, field distribution and electrode surface roughness have been developed that allow conduction and dielectric loss to be calculated during device design. It is interesting to note that analytical expressions for conduction loss are often preferred over numerical techniques because of the computational resources required to mesh within the skin depths of metals for accurate conduction loss approximations.

RF loss diminishes a modulator's efficiency by directly lowering the magnitude of the signal voltage as it propagates down the line. Including a term for the propagation loss of the modulating wave,  $\alpha_m$  (Np/m), Equation 5.1 for the RF voltage wave becomes

$$V(z) = V_0 e^{-\alpha_m z} \sin\left(\frac{2\pi n_m}{\lambda_m} z - 2\pi f_m t\right). \quad (5.3)$$

The attenuation in voltage along the modulation electrode changes the assumption in Equation 2.19, restated here for convenience as

$$\Delta\phi_{DC} = -\frac{\pi}{\lambda} n_0^3 r_{33} \frac{V}{d} \Gamma L,$$

of a uniform voltage  $V$  along the interaction length  $L$ . Accounting for propagation loss Equation 2.19 can be rewritten as

$$\Delta\phi = -\frac{\pi}{\lambda} n_0^3 r_{33} \frac{\Gamma}{d} \int_0^L V_0 e^{-\alpha_m z} \sin\left(\frac{2\pi n_m}{\lambda_m} z - 2\pi f_m t\right) dz, \quad (5.4)$$

which accounts for the exponential decay of the modulating voltage along the propagation length and the resultant decrease in phase shift per applied voltage.

### 5.1.2 Wave Velocity Matching

As the name suggests, a traveling wave modulator operates on the principle of an RF modulating wave propagating down a transmission line built around an optical

waveguide with an EO core material. This is in contrast to a low frequency lumped element modulator as discussed in earlier chapters, which assumes that the signal electrode is at a uniform potential all along the interaction length. The distinction between low frequency lumped element modulators and high frequency traveling wave modulators is most easily understood by considering the wavelength of the modulating signal ( $\lambda_{mod}$ ) in relation to the electrode length  $L$ . If  $\lambda_{mod} \gg L$  the modulation electrode only ever ‘sees’ a small, seemingly constant portion of the voltage wave. For example a 10 kHz signal has a wavelength of  $\lambda_{mod} = 30$  km with spatial oscillations far too gradual to be observed on a 1.5 cm electrode. At higher frequencies where the wavelength approaches the length of the modulation electrode,  $\lambda_{mod} \approx L$ , those spatial oscillations become significant. A 10 GHz signal has a wavelength of  $\lambda_{mod} = 3$  cm and a 1.5 cm modulation electrode will experience a half oscillation including a voltage peak and null. The variation in voltage along the modulation electrode further changes the assumption in Equation 2.19 of a uniform voltage along the interaction length and needs to be accounted for in the expected phase shift.

The interaction between the modulation and optical waves in a traveling wave modulator can be understood by considering an optical photon traveling down the interaction length of the modulator in the presence of the modulation voltage given in Equation 5.3 [86], [87]. A photon that enters the modulator at time  $t_0$  will be at position  $z$  at time

$$t = t_0 + \frac{z}{c} n_o \quad (5.5)$$

where  $n_o$  is the optical effective index of the waveguide mode. By plugging Equation 5.5 into 5.3 and rearranging the terms we find the voltage experienced by the photon at every point along its journey down the modulator interaction length

$$V(z) = V_0 e^{-\alpha_m z} \sin\left(\frac{2\pi n_m}{\lambda_m} \left(1 - \frac{n_o}{n_m}\right) z - 2\pi f_m t_0\right). \quad (5.6)$$

This expression is simplified by defining the RF-optical walk off constant

$$\eta \equiv \frac{2\pi n_m}{\lambda_m} \left(1 - \frac{n_o}{n_m}\right) = \beta_m \left(1 - \frac{n_o}{n_m}\right) \quad (5.7)$$

where  $\beta_m$  is the propagation constant of the RF modulation mode. The modulation voltage seen by the photon is then

$$V(z) = V_0 e^{-\alpha_m z} \sin(\eta z - 2\pi f_m t_0). \quad (5.8)$$

The concept of wave velocity, or index, matching is made clear by noting that if  $n_o = n_m$ , the walk off constant  $\eta = 0$  and a photon entering the modulator at time  $t_0$  experiences a voltage (and equivalently, modulation field) diminished only by the RF attenuation. Any mismatch in index results in a sinusoidal variation of the modulation voltage along the interaction length which will diminish the total phase shift expressed in Equation 2.19 to

$$\Delta\phi = -\frac{\pi}{\lambda} n_o^3 r_{33} \frac{\Gamma}{d} \int_0^L V_0 e^{-\alpha_m z} \sin(\eta z - 2\pi f_m t_0) dz. \quad (5.9)$$

The preceding analysis shows the importance of having well matched optical and RF effective indexes for efficient modulation. Index matching in OEOM modulators is simpler than in LiNbO<sub>3</sub> modulators because there is large dispersion in LiNbO<sub>3</sub> with the material index varying from 2.14 at 1550 nm to 5.6 in the RF regime [28] whereas the index of organic materials such as UV15 and IKD-1-50 in PMMA show much less dispersion varying from ~1.5–1.7 across the same span of spectrum.

This is particularly useful in microstrip modulators because the optical and RF modes are largely confined to the same materials.

RF index tuning in microstrip modulators can be achieved in a few different ways: the fraction of fringing field that is outside of the polymer can be increased or decreased by varying the height of the microstrip, resulting in a lower or higher effective index, respectively; the microstrip can be coated in an additional cladding layer of polymer to fully confine the field into a higher index material to raise the effective index; and the materials being used in the waveguide cladding, or microstrip cladding can be chosen specifically for their contribution to the resultant effective index. RF and optical effective indexes can be computed numerically using the dielectric properties in each frequency regime and the dimensions of the structures to design a well index matched modulator.

### 5.1.3 Modulation Frequency Response

When designing a traveling wave modulator both RF attenuation and index matching need to be considered for efficient operation at a given frequency. The net effect of these phenomena is quantified in what is referred to as the modulation, or EO, frequency response. This value is calculated by comparing the expected phase shift of an RF modulator at frequency  $f_m$  given in Equation 5.9, to the DC phase shift expected at low frequencies given by Equation 2.19

$$m(f_m) = \frac{|\Delta\phi(f_m)|}{|\Delta\phi_{DC}|}. \quad (5.10)$$

Varying expressions for the frequency response have been published [37], [87]–[89], and a derivation for the expression in [37] is outlined here. Assuming a harmonic time

dependence  $e^{j2\pi f_m t_0}$  and converting to the frequency domain Equation 5.9 can be rewritten as

$$\Delta\phi(f_m) = -\frac{\pi}{\lambda} n_0^3 r_{33} \frac{\Gamma}{d} V_0 e^{-\frac{j\pi}{2}} \int_0^L e^{-(\alpha_m + j\eta)z} dz. \quad (5.11)$$

We recognize the constant term in front of the integral as the phase shift from a DC modulator with voltage  $V_0$  divided by  $L$  and including a  $-\frac{\pi}{2}$  phase shift. Plugging this in and completing the integration yields

$$\Delta\phi(f_m) = -\frac{\Delta\phi_{DC} e^{-\frac{j\pi}{2}} (e^{\alpha_m L} e^{-j\eta L} - 1)(\alpha_m - j\eta)}{L (\alpha_m^2 + \eta^2)} \quad (5.12)$$

Taking the magnitude  $|\Delta\phi(f_m)| = \sqrt{\Delta\phi(f_m) \cdot \Delta\phi^*(f_m)}$  results in

$$|\Delta\phi(f_m)| = |\Delta\phi_{DC}| e^{-\alpha_m L} \sqrt{\frac{\sinh^2(\alpha_m L/2) + \sin^2(\eta L/2)}{\left(\frac{\alpha_m L}{2}\right)^2 + \left(\frac{\eta L}{2}\right)^2}} \quad (5.13)$$

and solving for  $m(f)$  in Equation 5.10 is then

$$m(f_m) = e^{-\alpha_m L} \sqrt{\frac{\sinh^2(\alpha_m L/2) + \sin^2(\eta L/2)}{\left(\frac{\alpha_m L}{2}\right)^2 + \left(\frac{\eta L}{2}\right)^2}}. \quad (5.14)$$

Equation 5.14 shows that for a lossless, perfectly matched modulator,  $\alpha_m = \eta = 0$  and  $m(f_m) = 1$  meaning that at RF frequencies the modulator has the same performance as at DC. The modulation frequency response can be evaluated with Equation 5.14 using numerically and analytically calculated values for effective index and attenuation.

#### 5.1.4 DC-RF-Optical Field Overlap

The importance of strong overlap between the optical and modulating electric fields for optimal drive voltage was discussed in Chapter 2. Equation 2.18, restated here for reference, gave the expression for the field overlap that is used in calculating the expected phase shift from a given modulating field:

$$\Gamma = \frac{d \iint_{EO \text{ core}} E_{mod}(x,y) \cdot |E_{opt}(x,y)|^2 dx dy}{V \iint_{-\infty}^{\infty} |E_{opt}(x,y)|^2 dx dy}.$$

Field overlap is equally important for high frequency operations and needs to be considered as electrode configurations are being designed for other factors such as impedance, index matching, loss, fabrication and packaging. Throughout the course of this work the option of switching to a planar CPW modulation transmission line was often considered for its ease of fabrication and ground plane contact. CPW lines are frequently used in LiNbO<sub>3</sub> modulators and are capable of providing adequate modulation fields for either TM or TE operation [28], [90], [91] by positioning the waveguide directly under the signal electrode or between and below the signal and ground electrodes, respectively. A CPW based modulator however depends on fringing fields rather than the direct field between signal and ground afforded by a microstrip modulator. Further, because OEOM modulators need to be poled to induce EO activity, there is an additional design component regarding field overlap.

As was discussed in Chapter 3 poling is the process that induces EO activity into the core material, and the resultant  $r_{33}$  is generally proportional to the strength of the field applied to the material. The spatial distribution of the static electric field produced by applying a bias to the modulation electrodes will therefore limit the EO activity achievable in an OEOM modulator architecture for a given poling voltage. While it seems intuitive that a microstrip would therefore be the optimal transmission

line for an OEOM modulator, a quantitative evaluation of microstrip and CPW transmission lines for OEOM modulator applications was developed by modifying the overlap integral to include the poling field.

The overlap integral in Equation 2.18 assumes that the EO material has a continuous  $r_{33}$  throughout the whole waveguide that is proportional to the poling field  $E_{pole} = V/d$ . This is not always true especially when considering the fields produced by a CPW in relation to the optical waveguide. To account for the poling field a unit less weighting distribution

$$r_{330}(x, y) = \frac{E_{pole}(x, y)}{V_{pole}/d} \quad (5.15)$$

was added to the overlap integral where  $E_{pole}(x, y)$  is now the component of the static field distribution aligned with the intended direction of optical operation (vertical for TM and horizontal for TE). This distribution captures the poling field strength at every point in the waveguide core normalized to the field that is typically assumed for poling: the applied voltage divided by the signal to ground electrode gap. Equation 5.15 is inserted into Equation 2.18 to yield a full DC-RF-optical overlap integral for OEOM modulators

$$\Gamma_{OEOM} = \frac{d}{V_{mod}} \frac{\iint_{EO\ core} E_{mod}(x, y) \cdot |E_{opt}(x, y)|^2 \cdot r_{330}(x, y) \, dx dy}{\iint_{-\infty}^{\infty} |E_{opt}(x, y)|^2 \, dx dy}. \quad (5.16)$$

Note that if the poling field has uniform magnitude  $V/d$  and fully engulfs the optical waveguide,  $r_{330}(x, y) = 1$  and Equation 2.18 is recovered. The static field distribution used to calculate  $r_{330}$  can be found using MATLAB PDE Toolbox to solve Laplace's equation or other electrostatic field solvers.

### 5.1.5 Effective Modulation Length

The RF attenuation, index mismatch and field overlaps were all combined into one figure of merit for an OEOM modulator and named the effective modulation length given by

$$L_{eff}(f_m) = \Gamma_{OEOM} \cdot m(f_m) \cdot L. \quad (5.17)$$

This figure of merit captures the  $V_\pi$  and frequency response capabilities of a given modulator architecture. It is necessary for the quantity to include the physical interaction length because the modulation depth improves as the length shortens, but the resulting  $V_\pi$  becomes larger. Note that for the optimal conditions of a uniform poling field, 100% overlap between the optical and modulation fields, perfect index matching and zero RF attenuation the effective interaction length  $L_{eff} = L$ .

Three traveling wave device designs were considered with this analysis: a TE CPW modulator with the optical waveguide below and between the signal and ground electrode; a TM CPW modulator with the optical waveguide below the center electrode; and a TM microstrip modulator with the optical waveguide below the signal electrode. A standard OEOM waveguide with a 3.5  $\mu\text{m}$  wide by 0.6  $\mu\text{m}$  deep trench and a 0.7  $\mu\text{m}$  thick ridge with a 3  $\mu\text{m}$  thick top cladding layer was used for all three modulator architectures. The CPW structure was assumed to be built on a thick handle of UV15 with no ground plane that would perturb the CPW field while the microstrip had a 3  $\mu\text{m}$  bottom cladding layer on top of a ground plane.

Optical, RF and DC models were solved using Lumerical MODE Solutions, HFSS and the MATLAB PDE Toolbox, respectively, to extract the field distributions and effective indexes of the RF and optical modes,  $n_m$  and  $n_o$ . Attenuation constants for the microstrip and CPW transmission lines were calculated with analytical expressions [78], [79], [92], [93] that more accurately reflect the conduction losses.

The simulated field distributions were imported into MATLAB and arranged onto a regular grid to numerically calculate  $\Gamma_{OEOM}$  in Equation 5.16. The numerically determined effective indexes and analytically calculated attenuation coefficients were plugged into Equation 5.14 to find  $m(f_m)$ . The field distributions, effective indexes, attenuation constants, modulation response and effective modulation lengths are shown in Figures 5.2, 5.3 and 5.4 for a TE CPW modulator, TM CPW modulator and TM microstrip modulator, respectively. In these figures the  $r_{330}$  distribution and the horizontal or vertical field component of the TE or TM optical mode are shown as heat maps while the poling and modulation field are shown as yellow vector field arrows. Note that the  $y$ -axis limits on the  $L_{eff}$  plots are all from 0–25 mm to emphasize the effective modulation length compared with the physical electrode length, and for consistent comparison between the three device architectures.

# TE CPW Modulator

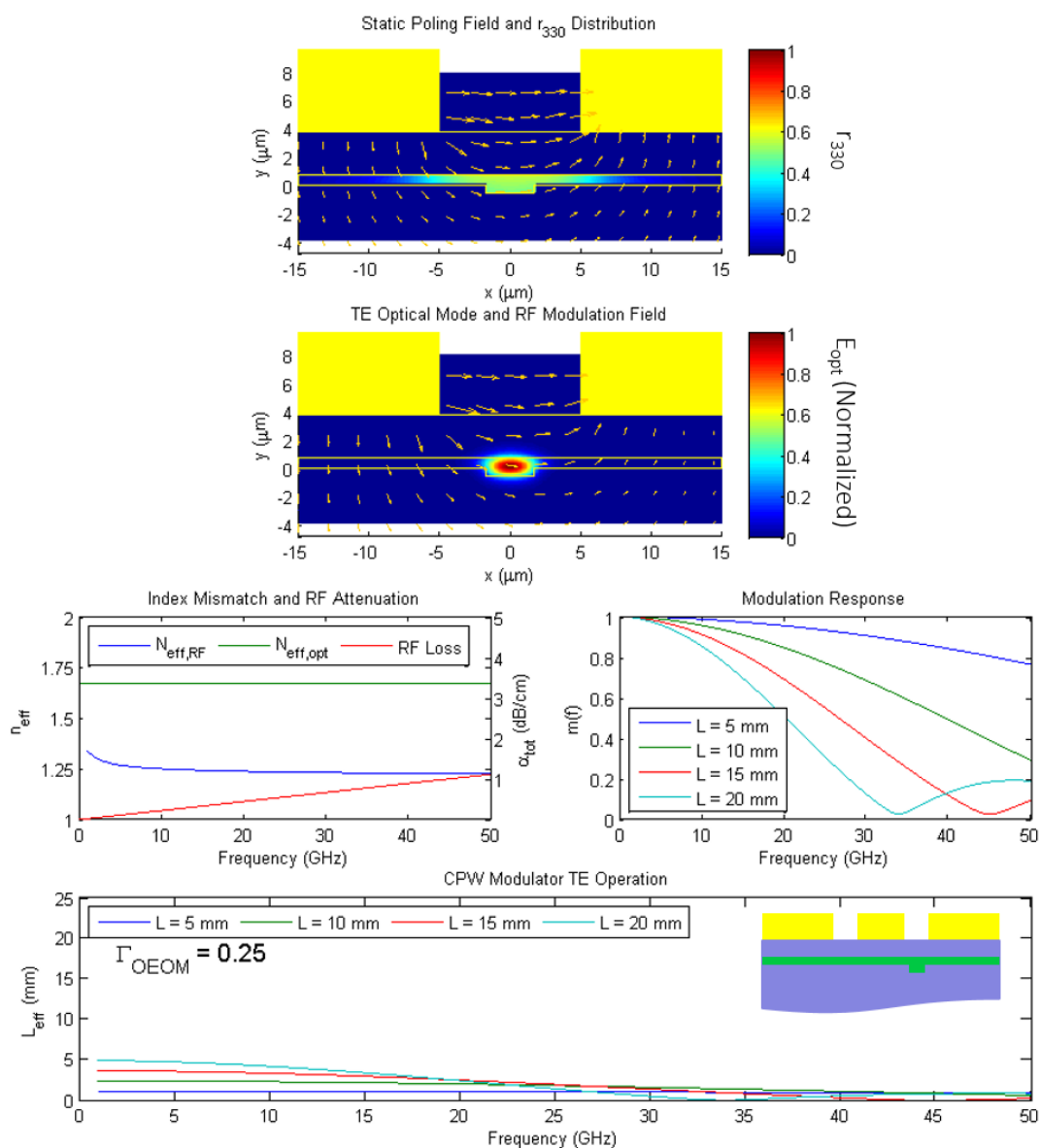


Figure 5.2: Effective length calculations for a TE CPW traveling wave OEOM modulator.

# TM CPW Modulator

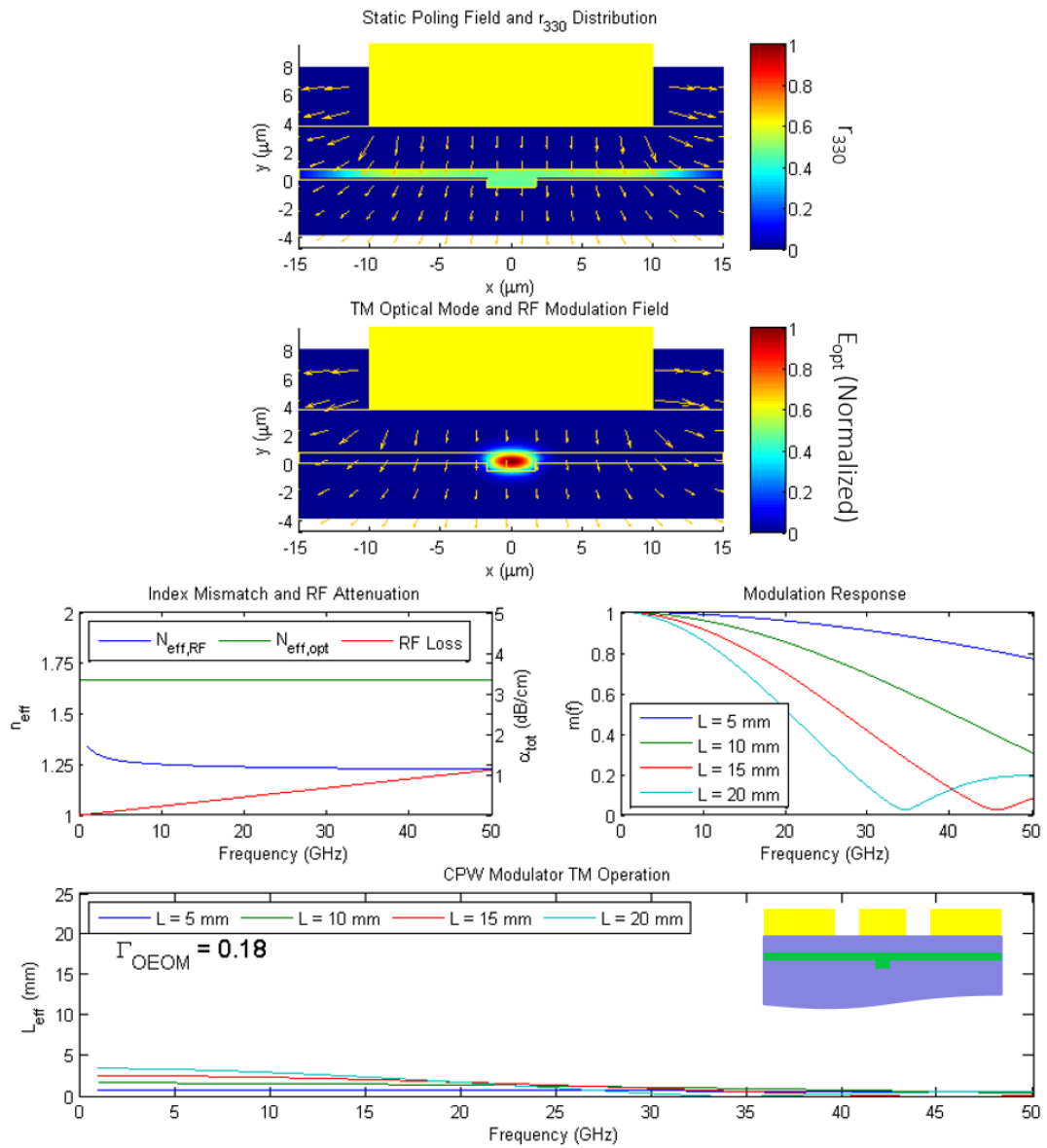


Figure 5.3: Effective length calculations for a TM CPW traveling wave OEOM modulator.

# TM Microstrip Modulator

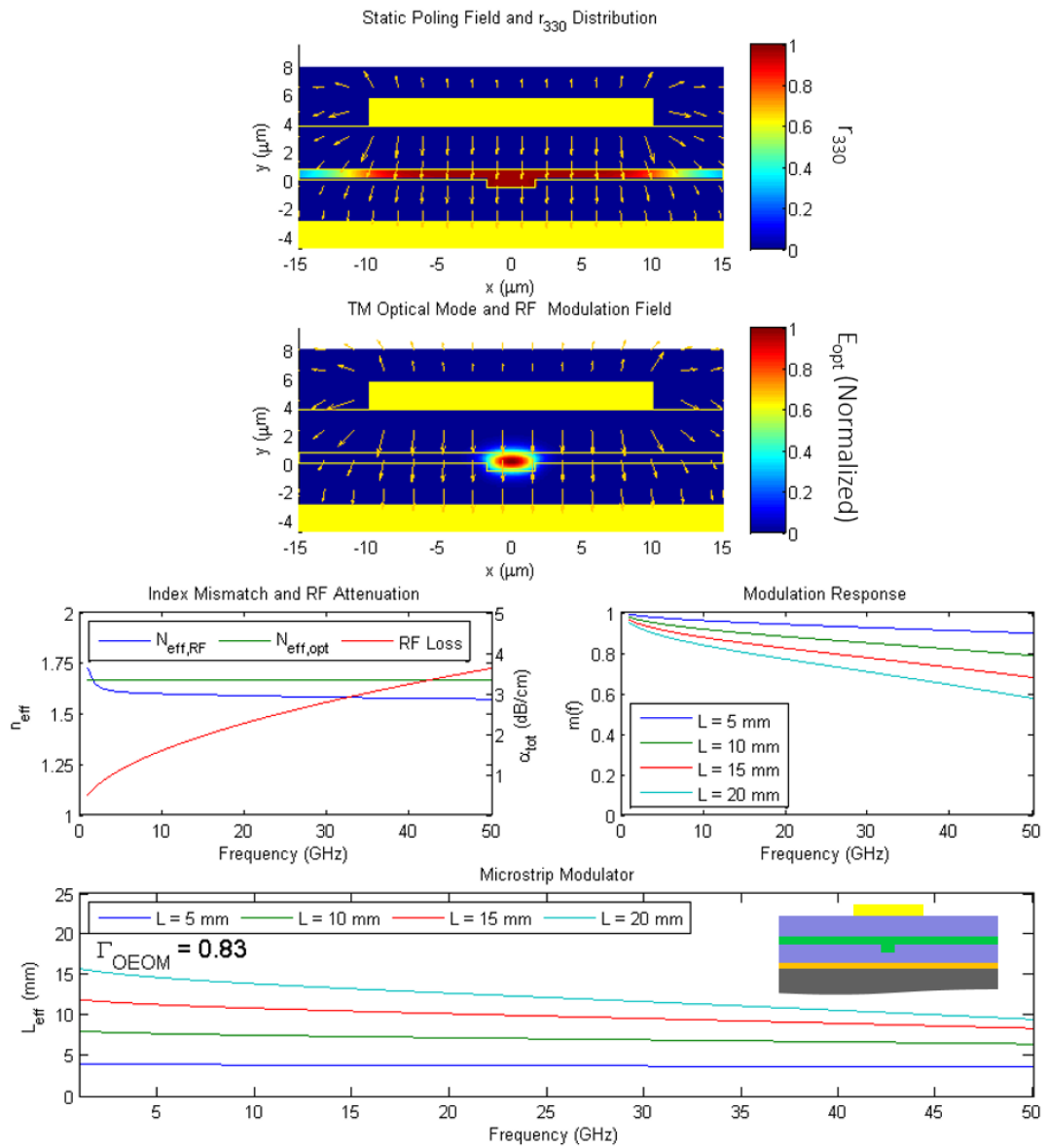


Figure 5.4: Effective length calculations for a TM microstrip traveling wave OEOM modulator.

The effective modulation length analysis clearly illustrates that the microstrip transmission line design is the most efficient device architecture with effective modulation lengths diminished by only ~17% at DC and gradual modulation response roll-off to 50 GHz. By contrast the TE and TM CPW architectures suffer 75-85% reduction in effective modulation length at DC and a much more rapid modulation response roll-off, particularly for the long interaction lengths.

Index matching could be improved in the CPW structures by coating the electrodes in the cladding polymer and confining the field to a higher index material instead of the air between the electrodes. However, the dual dependence on DC and RF field overlap for poling and modulating in OEOM modulators results in a very low  $\Gamma_{OEOM}$  of 0.25 and 0.18 for the TE and TM CPW devices, respectively, compared with 0.83 for the TM microstrip. Recall that the  $r_{330}$  distribution in  $\Gamma_{OEOM}$  is normalized to  $V_{pole}/d$  and in the CPW electrode configuration the direct field lines with amplitude of the order  $V_{pole}/d$  are found between the signal and ground while the optical waveguide core experiences only fringing field lines. In theory CPW devices should be able to achieve the same EO activity as microstrip devices by increasing the poling voltage so that the fringing field lines are the same strength as the direct field lines in a microstrip. In practice, however, using a larger poling voltage increases the likelihood of shorting and critically damaging the device. Additionally because CPW electrodes are separated by air the poling voltage is limited by the dielectric breakdown of air at 3 V/ $\mu\text{m}$  [94]. It was therefore apparent that despite the challenges of building and feeding it, a thin film microstrip modulator was the correct device architecture to pursue.

## 5.2 RF Microstrip Modulator Fabrication

The RF microstrip modulators were very similar to the DC modulators discussed in Chapter 3 with a few modifications that enable high frequency operation and feeding including a thicker ground plane electrode, electroplated signal electrode and a bending electrode trace for RF contact at the device edge. Each fabricated chip is  $2.5 \times 3$  cm and contains 3 modulators that are poled concurrently and diced into individual devices after fabrication. The fabrication process is shown schematically in Figure 5.5 and will be discussed in the following sections.

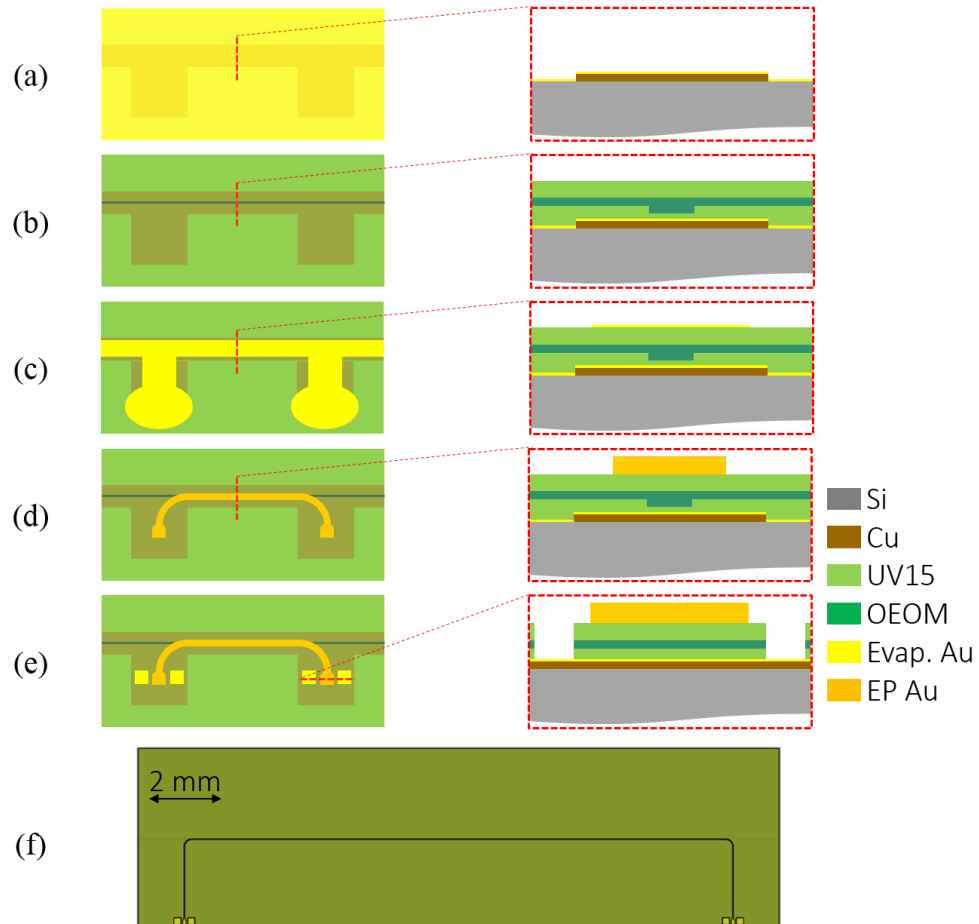


Figure 5.5: RF microstrip modulator fabrication process.

### 5.2.1 Patterned Cu Ground Plane

The first modification from the DC modulator was to include a thick ground plane layer that was a few skin depths deep to minimize conduction loss. The modulators were therefore built on the same 3  $\mu\text{m}$  Cu coated Si wafers that were used for the MSRRs. The Cu was again coated with a 20 nm/10 nm Ti/Au layer. However, the need to dice and cryo-cleave the modulators introduced a new challenge: prior to the Ti/Au deposition a thin copper oxide film grows on the Cu surface in standard atmospheric conditions [95], [96]. This copper oxide has poor adhesion to the Ti/Au layer and during dicing and cleaving the devices layers were susceptible to delamination and peeling off of the substrate.

To address this issue two modifications were introduced before the Ti/Au deposition. First, the Cu ground plane was patterned using a positive resist and ferric chloride into the shape shown in Figure 5.5 (a). This pattern ensures that the microstrip will be built over the thick ground plane and the optical waveguide will not have to traverse any uneven surfaces, but the rest of the surface is more securely adhered to the Si substrate via the superior adhesion of Ti to Si. The patterned ground plane (PGP) effectively anchors the device and prevents delamination and peeling sufficiently for the remaining processing steps. Secondly, a copper oxide etch step in a 5% sulfuric acid in deionized water solution was introduced. A 2 minute soak in this solution visibly changed the color of the Cu surface, removing the oxide and exposing pure Cu. After the copper oxide etch the substrates were held under vacuum until they were transferred to the e-beam evaporator for Ti/Au deposition.

### **5.2.2 Optical Waveguide Fabrication and Poling**

SEO250 optical waveguides identical to those discussed in Chapter 3 were built on the PGP substrates. The fabrication process for the waveguides was the same as the one discussed in Section 3.1 except for the addition of a 2 minute 100 °C smoothing bake step after the bottom cladding deposition to ensure a flat UV15 surface over the PGP edges. A top down and cross sectional schematic of the device after this step are shown in Figure 5.5 (b).

Following waveguide fabrication a 40 nm Au coating is sputtered onto the top UV15 layer and a large area poling electrode is patterned with positive resist and Au wet etch as shown in Figure 5.5 (c). Poling was done with a designated thin film electrode rather than the electroplated signal electrode to avoid the high field concentrations that occur when a large bias is applied to narrow conductor lines which would increase the likelihood of shorting. Additionally, having large scale poling electrode allowed the use of the previously built poling station and probes shown in Figure 3.6.

The same poling process that was outlined in Section 3.2.2 was implemented for poling the high frequency devices. Poling behavior was consistent with what was observed in the low frequency devices, unperturbed by the Cu ground plane or the ripples at the PGP edges. After poling, the electrode is removed with Au wet etch and the device is baked under constant vacuum at 100 °C for > 5 hours to remove any residual moisture.

### **5.2.3 Microstrip Signal Fabrication and Ground Plane Exposure**

The microstrip modulation electrode is patterned in a 3 μm thick layer of NR9-3000P spun at 3000 rpm and soft baked at 80 °C for 3 minutes. The soft bake

temperature was lowered to prevent bubbling through the waveguide stack that was observed at the standard 100 °C soft bake temperature in the presence of the resist solvents. The pattern is then exposed with 70 mJ/cm<sup>2</sup>, post exposure baked at 100 °C and developed in RD6 for 30 seconds. After developing, the device is put through a light O<sub>2</sub> plasma clean to remove any residual resist from the areas to be plated and the back of the substrate is coated with polyimide tape to prevent back plating. The signal electrode is electroplated with the same procedure used for the MSRRs including heating and cooling with the electroplating solution for slow thermal cycling to prevent CTE mismatch cracking. The plating is carried out using Techni-Au 25 ES RTU at 1 mA of current for ~45 minutes to produce ~3 μm thick Au traces. The microstrip width is 17 μm with 2 mm radius 90° bends that lead to 80×80 μm wire bond contact pads as shown in Figure 5.5 (d) and in a to scale CAD drawing in Figure 5.5 (f). After removal from the cooled electroplating solution the resist is removed in RR41 and an O<sub>2</sub> plasma, and the seed layer is removed in Au etch. The electroplating process is again followed by a 5 hour, 100 °C bake under vacuum to remove any absorbed moisture.

The final fabrication step is to etch ground plane vias adjacent to the microstrip contact pad as shown in Figure 5.5 (e). The device is first encapsulated in an e-beam evaporated 30 nm Ti layer to prevent contact with the resist solvents that have been observed to permeate the top cladding layer and damage the OEOM core. An 8 μm thick layer of NR2-8000P is deposited, aligned and patterned according the process used in Section 4.3 for ground plane exposure in the MSRRs. The exposed via patterns are further cleaned out with an O<sub>2</sub> plasma, and the Ti encapsulation layer is locally etched with a 20:1:1 solution of H<sub>2</sub>O:HF:H<sub>2</sub>O<sub>2</sub>. Finally the vias are etched in the

O<sub>2</sub>/CF<sub>4</sub> ICP etch listed in Table 4.2 to expose the top Au layer of the patterned ground plane. After etching, the resist is removed with RR41, but the Ti layer is left to encapsulate the device during edge facet dicing.

#### **5.2.4 Edge Facet Dicing and Optical End Facet Cleaving**

The fabricated chip is diced into individual modulators using an R07 resin bond dicing blade from DiscoUSA (CA). As will be discussed in the following chapter it was necessary to have the microstrip contact pad in close proximity to the device edge for feeding the RF signal. The modulators were therefore diced 20 μm from the end of the microstrip contact pad and the opposite edge was diced 5 mm away, parallel to the RF feed edge. The dicing was done with a blade rotation of 3000 rpm and a 1 mm/sec feed rate. After dicing, the modulators are rinsed in deionized water and the Ti encapsulation layer is wet etched. The end facets for optical coupling are then prepared by cryo-cleaving as discussed in Section 3.1, and the modulator is ready for optical and RF characterization. A to-scale drawing of the finalized device is shown in Figure 5.5 (f) and SEM images of a diced device showing the patterned ground plane and smooth edge facet are shown in Figure 5.6.

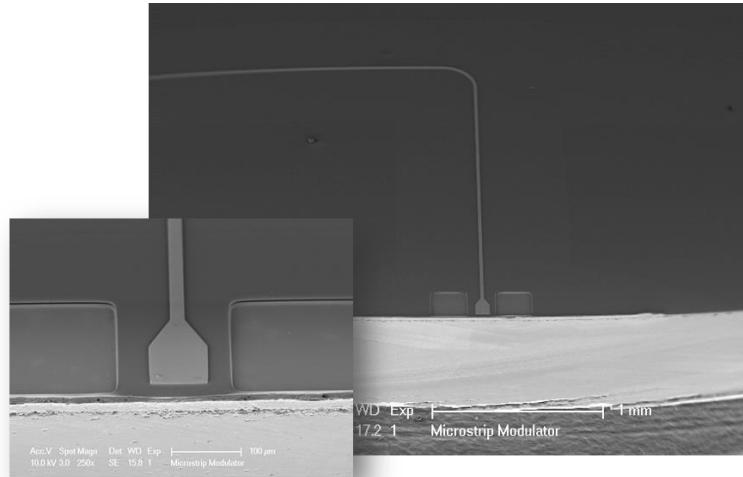


Figure 5.6: SEM of diced microstrip modulator showing electroplated signal electrode, ground plane vias and diced edge facet.

### 5.3 Conclusion

With the design and fabrication of the RF OEOM modulator concluded all that remained was to characterize the device at frequencies up to 50 GHz. Characterizing a microstrip modulator however introduces its own set of challenges. The encapsulated ground plane in a microstrip transmission line was addressed with the ground plane vias etched adjacent to the microstrip contact pads that were sufficient for RF feeding with CPW contact probes. However, for practical device integration a permanent RF feed to the microstrip line needs to be implemented. This RF packaging challenge is addressed and a demonstrated solution is presented in the next chapter.

## Chapter 6

### RF PACKAGING AND MODULATION TESTING

Practical implementation of any optical or electrical device requires a compact and efficient packaging. For EO modulators, this entails optical coupling into and out of the waveguide and RF feeding to the modulation transmission line. Optical packaging is typically accomplished with V-groove seated fibers that can be bonded to the waveguide end facet with a UV curable epoxy. A pervasive challenge in many optical devices is overcoming the difference in mode size between a standard SMF-28 single mode fiber, which has a mode field diameter of  $\sim 10.5 \mu\text{m}$ , and the mode of a planar optical waveguide, which often have mode field diameters of  $5 \mu\text{m}$  and below. Recently Herrera, *et al.*, developed a bonding technique that involves splicing a SMF-28 fiber to a high numerical aperture fiber that transitions the  $10.5 \mu\text{m}$  diameter mode down to  $3.2 \mu\text{m}$  diameter fiber mode, allowing for a  $< 3 \text{ dB}$  total coupling loss to a  $4.5 \mu\text{m}$  diameter waveguide mode [97]. This solution is applicable to the optical waveguides in this work and would allow for efficient optical packaging. With solutions such as this in mind, efforts were diverted from optical packaging towards RF feeding, and devices were coupled to optically with lensed fibers on translation stages for modulation demonstrations.

Several previous microstrip modulators have demonstrated EO modulation at RF frequencies; however most of these devices use on-device CPW to microstrip transitions that enable device characterization but not integration with RF circuitry [89], [98]. In practice, it is often necessary for RF signals to be amplified, filtered,

split or otherwise altered before being sent to the EO modulator. Standard RF components that would perform these manipulations are typically built on substrates such as ceramic, Teflon or LCP, chosen to leverage various properties such as low RF losses, an appropriate dielectric constant and physical characteristics beneficial to integration. This is in contrast to OEOM modulators, which are typically—as in this work—built on Si wafers, which provide optically smooth surfaces, crystal planes for end facet cleaving, and high thermal conductivity for micron scale lithographic patterning and poling processes. The ideal solution of homogeneous integration between RF components and OEOM modulators would therefore require significant alterations in either the modulator or RF component design and fabrication process. An alternative approach is to integrate the components together in a compact package by close proximity mounting and a cross-platform transition. The following sections will describe a low loss wire bond transition and packaging scheme that enables heterogeneous integration between a ceramic substrate and an OEOM modulator, and direct connection to 2.4 mm RF cables for signal feeding up to 50 GHz.

### **6.1 Ceramic CPW to Thin Film Microstrip Transition**

To achieve the mode transition from the RF substrate to the thin film microstrip of the OEOM modulator, an appropriate feed transmission line on the RF substrate needed to be chosen. While first intuition suggests designing a transition from a microstrip built on an RF substrate to the thin film polymer microstrip, there are several drawbacks to this approach. The microstrip transmission line mode exists in the substrate and is roughly the size of the substrate thickness (100's of  $\mu\text{m}$  for typical RF material platforms). This results in a large mode size mismatch with the thin film microstrip, which introduces loss into the transition. Additionally connecting

the ground planes between two microstrips on different substrates is challenging and requires either mounting to a conductive base or making contact through vias that must be etched through the 100's of  $\mu\text{m}$ -thick RF substrate. Conversely CPW transmission lines support a tightly confined RF mode near the surface of the substrate that is comparable in size to the mode of a thin film microstrip (10's of  $\mu\text{m}$ ), allowing for a smoother field transition. Furthermore the easily accessible ground planes on the substrate surface are much more simply connected to the ground plane exposed through vias on a thin film microstrip. For these reasons a CPW on a 96% alumina handle was chosen to be the feed transmission line. Ninety-six percent alumina is a common ceramic substrate with low RF losses and a dielectric constant of  $\epsilon_r = 9.4$ .

### **6.1.1 Wire Bond Transition Design**

The CPW signal width, signal to ground spacing, and electrode thickness were 80  $\mu\text{m}$ , 50  $\mu\text{m}$  and 5  $\mu\text{m}$ , respectively, yielding a 50  $\Omega$  impedance to match with the RF feed and the thin film microstrip. The transition from CPW to thin film microstrip modulator was first designed and tested on single layer UV15 thin film microstrips for simplicity and to avoid using OEOM during process development. As was mentioned previously, UV15 compromised > 80% of the OEOM modulator so the UV15 microstrip closely mimics the RF characteristics of the modulator microstrip. As with the modulator, the UV15 microstrips had signal width, thickness and substrate height of 17  $\mu\text{m}$ , 5  $\mu\text{m}$  and 7  $\mu\text{m}$ , respectively.

The feed CPW and thin film microstrip were connected via wire bonds that smoothly transformed the CPW mode, to a conductor-backed CPW mode, to a microstrip mode with minimal energy lost. The transition was investigated numerically in HFSS to analyze the effect of mounting proximity, wire bond thickness

and bond position. The HFSS model in Figure 6.1 (a) shows the wire bonds that connect the CPW signal to a contact pad at the end of the microstrip signal, and the CPW ground pads to the microstrip ground plane through vias that are etched through the polymer substrate.

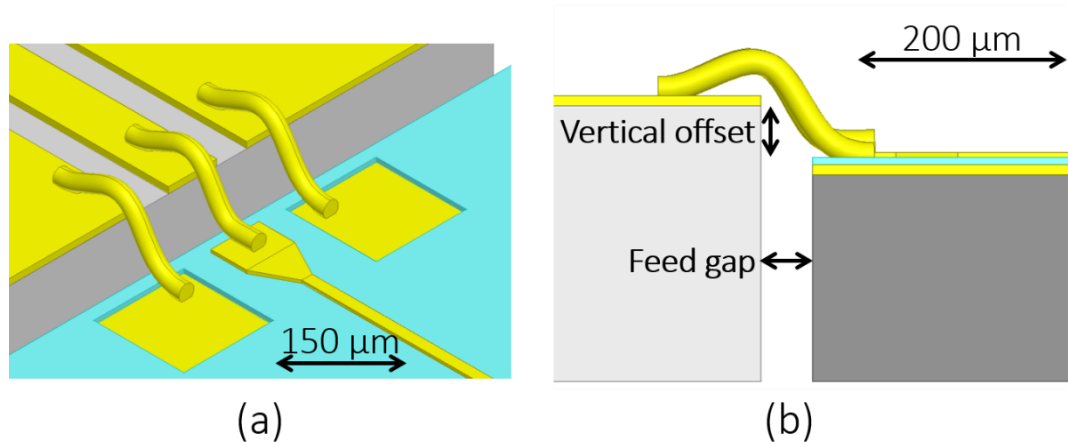


Figure 6.1: (a) HFSS model of CPW to thin film microstrip transition. (b) Vertical offset and feed gap that were determined to be the dominant parameter for a low loss transition.

Simulations using 25 μm and 18 μm diameter wire demonstrated very similar performance with < 0.25 dB additional loss introduced by the thinner wire from 0–50 GHz. The signal wire bond point and alignment also showed a comfortable tolerance allowing for lateral misalignment of up to 100 μm without significantly degrading performance. The dominating parameter for a low loss transition was found to be the spacing between the CPW and the microstrip. In particular, the feed gap between the two substrates and the vertical offset between the surfaces of the two devices, as labeled in Figure 6.1 (b), need to be minimized for a low loss transition.

Smooth edge facets with micron-scale roughness are easily achieved with the dicing saw discussed in Chapter 5. These edge facets allow for flush lateral seating, and a 50  $\mu\text{m}$  feed gap was accordingly assumed for the numerical transition study. Simulations were run sweeping the vertical offset from -150  $\mu\text{m}$  to 150  $\mu\text{m}$  and the  $S_{12}$  transmission parameters from 0 to 50 GHz were evaluated. Figure 6.2 (a) shows the field transition from CPW to conductor-backed CPW to microstrip. The power throughput,  $S_{12}$ , is shown in Figure 6.2 (b) and shows that if the vertical offset and feed gap can be brought to 50  $\mu\text{m}$  or below, a transmission loss of less than 0.5 dB can be expected for each CPW to microstrip transmission.

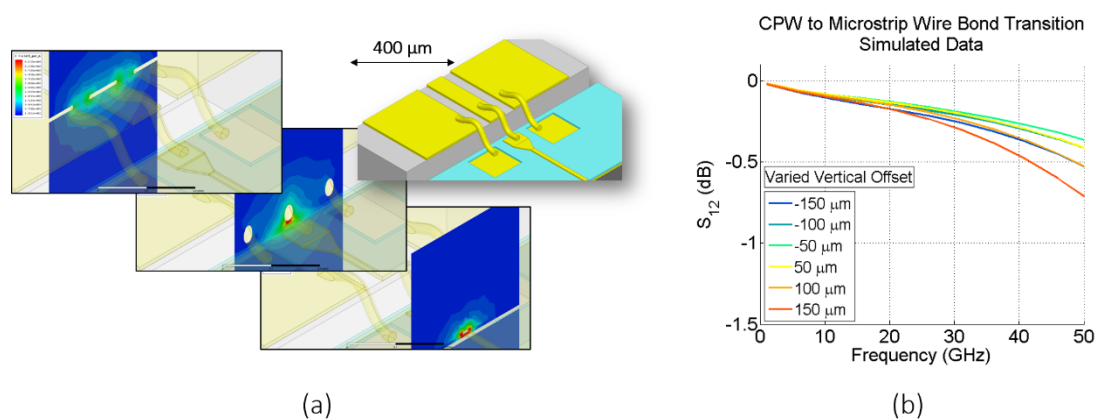


Figure 6.2: (a) Field transition from CPW to conductor-backed CPW to microstrip. (b)  $S_{12}$  parameters for the CPW to microstrip transition with varying vertical offset.

### 6.1.2 Wire Bond Transition Testing

The wire bond transition was tested on short lengths of ceramic CPW and UV15 microstrip. The CPWs were fabricated on 96% alumina ceramic substrates purchased from CoorsTek, Inc (CO). The substrates were coated with an e-beam

evaporated 20/30 nm Ti/Au seed layer, and the CPW was patterned in NR2-8000P and Au electroplated in Techni-Au 25 ES RTU using the same process used for electroplating the MSRR structures. The UV15 microstrips were fabricated using the same procedure that was used for the UV15 MSRRs.

The vertical offset was minimized by intentional selection of handle wafers. The Cu coated Si microstrip substrates from IMAT were cleaved from an 8" wafer and were measured to be 734  $\mu\text{m}$  thick. The chosen ceramic substrate was 0.03", or 762  $\mu\text{m}$  thick. To further level the substrates, a 25  $\mu\text{m}$  layer of polyimide tape was adhered to the bottom of the Si, bringing the nominal heights to within 10  $\mu\text{m}$  of each other, well below the offset necessary for a transition with <1 dB loss according to numerical simulations. Edge facets on both samples were diced 20  $\mu\text{m}$  from the end of the transmission lines, and the two devices were aligned and seated flush against one another on an aluminum mount with double-sided polyimide tape. The mounted devices were heated to 60  $^{\circ}\text{C}$  and connected with 25  $\mu\text{m}$  diameter Au wire bonds using an F&K Delvotek ultrasonic wedge wire bonding system. An SEM image of the test CPW to microstrip wire bond transition is shown in Figure 6.3.

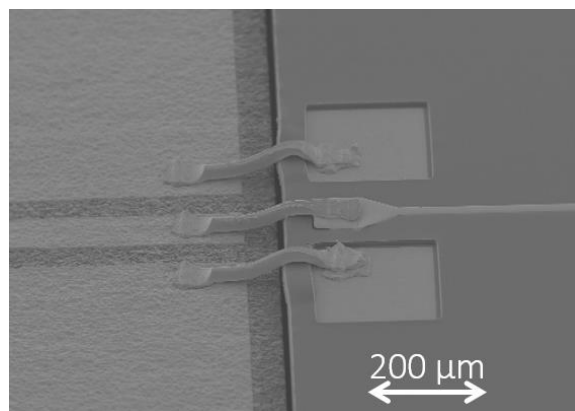


Figure 6.3: SEM image of the CPW to thin film microstrip wirebond transition.

Test devices were characterized using high frequency probes connected to an Agilent 8361C PNA after an open-short-load-through calibration. Initial attempts to characterize the wire bond transition loss ( $S_{12,WB}$ ) were made by measuring the loss of the bonded devices together from end to end ( $S_{12,Tot}$ ) and then subtracting the expected losses, ( $S_{12,CPW}$  and  $S_{12,MS}$ ), of each transmission line based on measured attenuation coefficients of identical microstrip and CPW devices individually. The loss resulting from the wire bond was then calculated as  $S_{12,WB} = S_{12,Tot} - S_{12,CPW} - S_{12,MS}$ . This technique was eventually abandoned due to small spikes and noise in the measurements that were greater than 1 dB, which resulted in  $S_{12,WB}$  being greater than 0 at some frequencies. However, this method of measurement did indicate that the transition was introducing losses on the order of 1 dB and below. A quantitative evaluation of the transition was achieved by direct probing in which the CPW and microstrip signal electrodes were laser ablated just beyond the wire bonding points, and the probes made contact immediately adjacent to the wire bonds. The resulting power throughput is shown in Figure 6.4 and remains below 1 dB up to 50 GHz, sufficiently low for integration from an RF substrate to EO modulator.

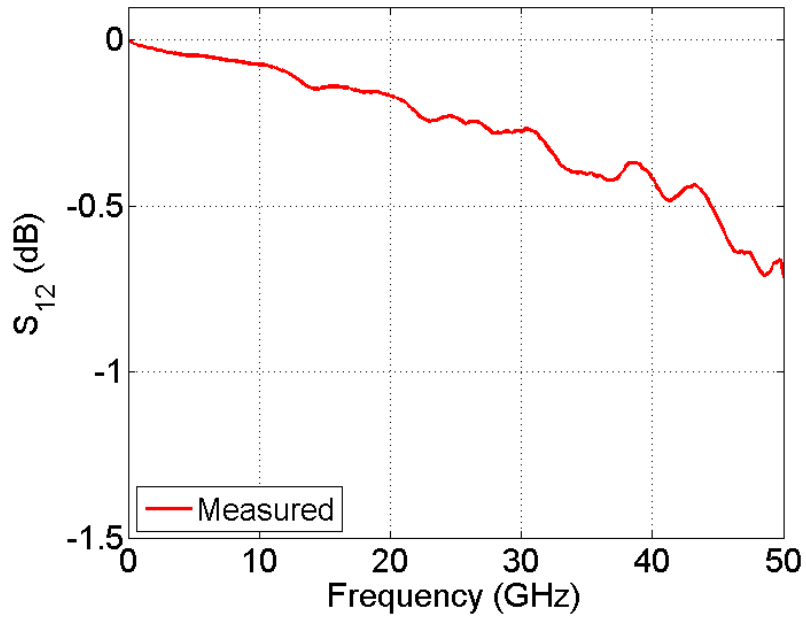


Figure 6.4: Direct probe measurement of CPW to microstrip wire bond transition loss.

The wire bond transition was therefore determined to be the optimal solution for heterogeneous integration of a ceramic RF substrate with a thin film microstrip on a Si substrate; the final challenge was implementing this transition with the OEOM modulators discussed in Chapter 5 for RF modulation characterization up to 50 GHz.

## 6.2 RF Packaging

The optimal configuration for practical usage and simplified testing is an RF packaging scheme that enables direct connection with coaxial cables. With the transition from the thin film microstrip to the ceramic CPW completed, a final transition from the CPW to a coaxial cable connector was necessary. Fortunately, solutions for this transition are commercially available.

### 6.2.1 Coaxial to CPW to Microstrip Integration

Planar to coaxial end launch connectors (ELCs) that connect the signal electrode of a planar transmission line to the center pin electrode of a coaxial transmission line that operate up to 110 GHz can be purchased from Southwest Microwave (AZ). For this work, ELCs that transition from a 2.4 mm coaxial connector that operate up to 50 GHz were purchased and used to contact the non-bonded end of the ceramic feed CPWs.

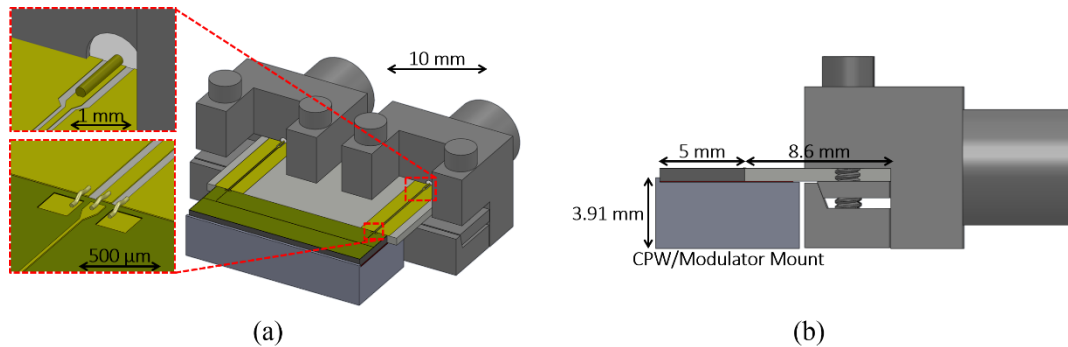
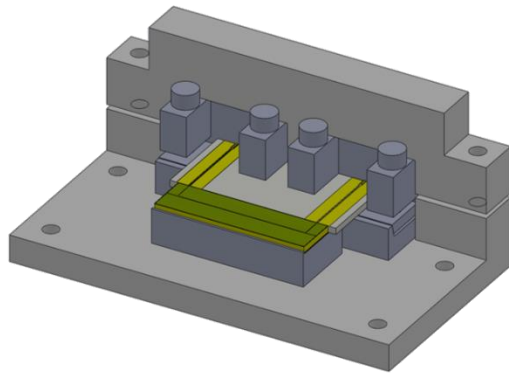


Figure 6.5: Coaxial to CPW to microstrip modulator RF packaging.

The ELC to CPW contact and wire bond transition are shown in the insets of Figure 6.5 (a) along with a CAD drawing of the full proposed integration scheme. The input and output CPWs were fabricated on a single substrate, spaced by 15.4 mm to align with the microstrip wire bond pads, and diced at both ends with a 20 μm gap between the end of the lines and the edges of the substrate. The CPW lines were 8.6 mm long, including 7.5 mm of 80 μm wide signal trace, a 100 μm taper, and a 1 mm long section with 200 μm wide signal trace for contact with the 127 μm diameter ELC pin. As with the test CPW to microstrip devices, the modulator and

CPW were seated flush against each other with their signal electrodes aligned and secured to an aluminum mount with double-sided polyimide tape. The mount was machined precisely to 3.91 mm so that the modulator and CPW were held at the same height as determined by the ELC, as shown in the side view of Figure 6.5 (b).

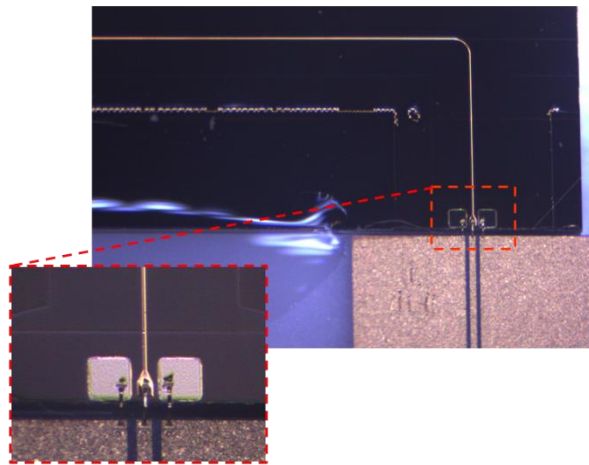
Because the wire bonds between the ceramic and Si substrates are very short and delicate, it was necessary to restrict the relative movement between the substrates to prevent breaking or delaminating the wire bond connections. To stabilize the individual components, a testing stage clamp that holds the modulator, CPW, aluminum mount and ELC was designed and machined in aluminum. Once mounted in the clamp, the whole assembly was firmly secured and could be transferred to the wire bonding system for signal and ground contact via 17  $\mu\text{m}$  Au wires, which were found to yield more reliable bonds than the 25  $\mu\text{m}$  wires. With the modulator and RF circuitry fully packaged for operation up to 50 GHz, the device was mounted to a testing podium where it could be fed high frequency signals with 2.4 mm cables and probed optically with lensed fibers on translation stages. A CAD drawing of the testing stage clamp assembly and a photograph of a fabricated and mounted device on the testing podium is shown in Figure 6.6 (a) and (b), respectively. Figure 6.6 (c) shows a stereoscope image of the feed CPW and modulator microstrip mounted and connected by the Au wire bonds.



(a)



(b)



(c)

Figure 6.6: (a) CAD drawing of the testing stage clamp assembly. (b) Photograph of a mounted and bonded CPW fed OEOM modulator. (c) Stereoscope image of feed CPW, modulator microstrip and wirebond connections.

### 6.2.2 RF Packaging Loss Testing

The RF packaging was characterized with a series of S-parameter measurements taken from 0–50 GHz with the Agilent PNA. The full response of a packaged device was first measured by connecting 2.4 mm cables to the ELCs after an open-short-load-through calibration; the measured S-parameters are shown in Figure

6.7. The  $S_{11}$  and  $S_{22}$  reflection parameters remain below -10 dB all the way to 50 GHz, indicating that both the ELC to CPW and CPW to microstrip impedances are well matched. The total loss of the packaged device remained below 15 dB to 50 GHz with most of the loss attributed to the almost 2 cm of thin film microstrip propagation.

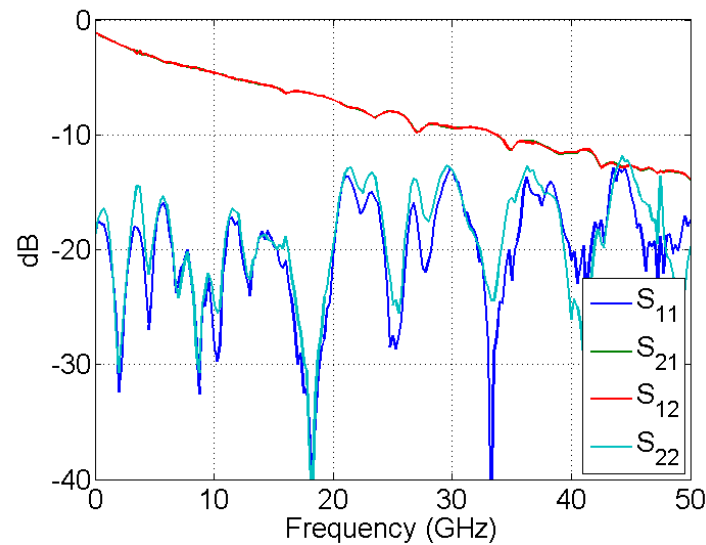


Figure 6.7: S-parameters of RF packaged OEOM phase modulator.

The performance of the RF packaging scheme is truly reflected in the loss that resulted from the ELC to CPW and CPW to microstrip transitions alone, as this is what would be carried over to another RF feed and microstrip modulator assembly. Specifically the loss introduced by these transitions on only the input side will dictate how much RF energy is fed to the modulator electrode. The loss of the transitions was referred to as the feed loss, and was extracted by measuring the attenuation coefficients of CPW and microstrip lines identical to those in the packaged device and

subtracting the expected transmission line loss from the total loss measured in Figure 6.7, hereafter referred to as  $S_{12, \text{PkgMod}}$ . Unpackaged CPWs and modulator microstrips of known lengths were measured with high frequency probes at the GSG contact points, and the frequency dependent attenuation coefficients in dB/mm were backed out as shown in Figure 6.8.

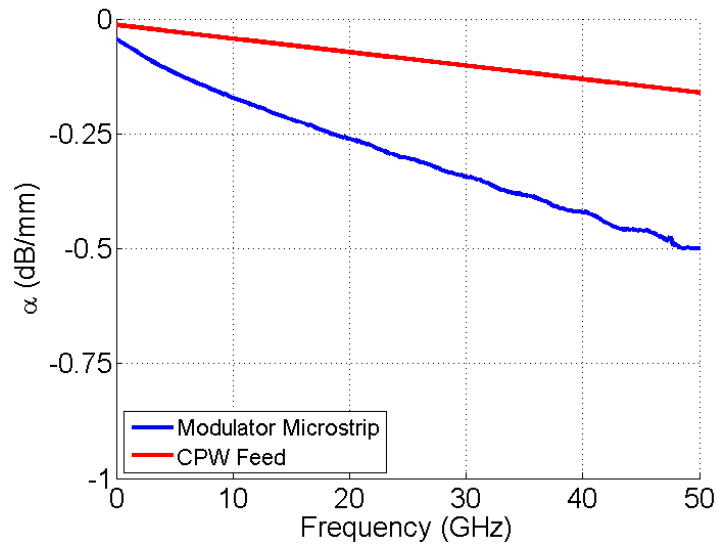


Figure 6.8: CPW and modulator microstrip attenuation coefficients.

Note that to remove small ripples due to reflection, the CPW attenuation constant has been fitted to  $\alpha = a\sqrt{f} + bf$  as in Section 4.5. Using these attenuation coefficients, the expected loss for the total CPW propagation length ( $2 \times 7.5$  mm),  $S_{12, \text{CPW}}$ , and microstrip propagation length (19.62 mm including the bending radius and 2 mm feed lengths),  $S_{12, \text{ModMS}}$ , were calculated. The feed loss on just the input side was then calculated as  $S_{12, \text{Feed}} = (S_{12, \text{PkgMod}} - S_{12, \text{ModMS}} - S_{12, \text{CPW}})/2$ , thereby isolating

the packaging transition losses from the losses inherent to the modulator and CPW feed, which could be further optimized for higher performance in another device. The extracted losses are all plotted in Figure 6.9 where the feed loss can be seen to remain below 1 dB out to 50 GHz.

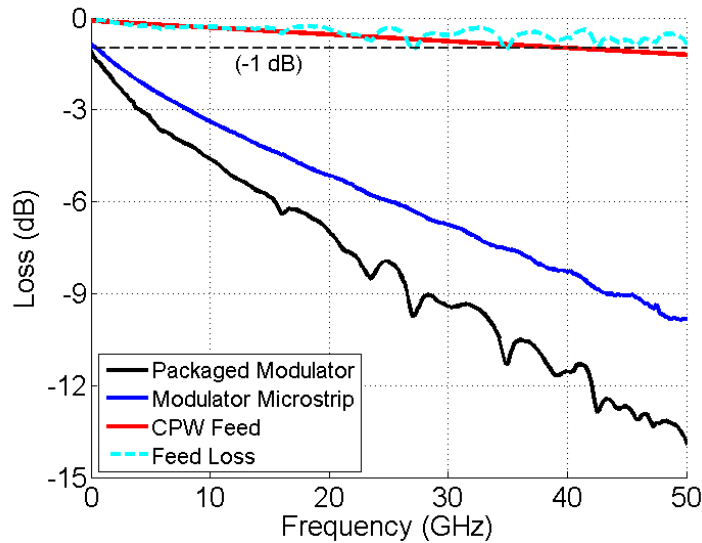


Figure 6.9: Loss factors in the microstrip modulator RF packaging illustrating a feed loss <1 dB out to 50 GHz.

The measured feed loss is comparable to the loss measured in previously demonstrated single substrate CPW to OEOM microstrip modulator transitions for probe testing [89], [98]. This packaging scheme however has the added benefit of including a transition to and from a ceramic substrate that supports the RF circuitry necessary for electrical signal manipulations, thereby enabling a compact, modular component.

### 6.3 RF Phase Modulation

The final analysis for the packaged RF modulator was to evaluate the modulation response of the fabricated device. As with DC modulation measurements, the phase information is unavailable by direct measurement of the output 1550 nm optical beam. Fortunately, at higher frequencies the phase modulation results in generated optical sidebands that are further from the carrier and more easily distinguishable than at low frequencies, and can therefore be measured and analyzed to evaluate modulation response. This measurement technique and measured results are presented in the following sections.

#### 6.3.1 Optical Sideband Generation

The sinusoidal phase variation imparted by a modulation voltage generates new frequency components spaced by the frequency of the modulation signal. These sidebands can be derived mathematically by considering the phase modulated optical field

$$\mathbf{E} = \mathbf{E}_0 e^{-j(\beta_0 L + \Delta\phi)} e^{j\omega_o t} \quad (6.1)$$

where  $\omega_o$  is the optical angular frequency and  $\Delta\phi$  is the phase shift given in Equation 2.19 as  $\Delta\phi = -\frac{\pi}{\lambda} n_0^3 r_{33} \frac{V}{d} \Gamma L$ . This expression for phase shift is now modified to explicitly state the time dependence of the modulation voltage as  $V = V_0 \sin(\omega_m t)$  where  $\omega_m$  is the modulation angular frequency. Plugging this into Equation 6.1 gives

$$\mathbf{E} = \mathbf{E}_0 e^{-j\beta_0 L} e^{-j\delta \sin(\omega_m t)} e^{j\omega_o t} \quad (6.2)$$

where the phase modulation index

$$\delta = \frac{\pi}{\lambda} n_0^3 r_{33} \frac{\Gamma}{d} V_0 L \quad (6.3)$$

has been defined. Note that this phase modulation index is simply the DC phase shift with an applied voltage  $V_0$ . The phase shift term in Equation 6.2 can be expanded into a sum of Bessel functions of the first kind,  $J_n(x)$ , using the Jacobi-Anger expansion, which is expressed as:

$$e^{jx\sin\theta} = \sum_{n=-\infty}^{\infty} J_n(x)e^{jn\theta} \quad (6.4)$$

by inserting  $\delta$  for  $x$  and  $\omega_m t$  for  $\theta$ . The modulated optical field is then:

$$\mathbf{E} = \mathbf{E}_0 e^{-j\beta_0 L} \sum_{n=-\infty}^{\infty} J_n(\delta) e^{jn\omega_m t} e^{j\omega_o t}. \quad (6.5)$$

For a small value of  $\delta$ , only the zeroth and first order Bessel functions will be non-negligible, simplifying Equation 6.5 to

$$\mathbf{E} = \mathbf{E}_0 e^{-j\beta_0 L} [J_{-1}(\delta)e^{-j\omega_m t} + J_0(\delta) + J_1(\delta)e^{j\omega_m t}] e^{j\omega_o t}. \quad (6.6)$$

This expression becomes more illuminating by using the relation  $J_{-n}(\delta) = (-1)^n J_n(\delta)$  and rearranging to illustrate the carrier frequency and generated upper and lower optical sidebands

$$\mathbf{E} = \mathbf{E}_0 e^{-j\beta_0 L} \left[ \underbrace{J_0(\delta)e^{j\omega_o t}}_{\text{Carrier}} - \underbrace{J_1(\delta)e^{j(\omega_o - \omega_m)t}}_{\text{Lower sideband}} + \underbrace{J_1(\delta)e^{j(\omega_o + \omega_m)t}}_{\text{Upper sideband}} \right]. \quad (6.7)$$

These three field components oscillate with different optical frequencies  $\omega_o$ ,  $\omega_o - \omega_m$  and  $\omega_o + \omega_m$  and can be distinguished with an optical spectrum analyzer (OSA) with sufficiently fine resolution. The optical frequency at 1550 nm is  $\sim 193$  THz, and a generated frequency component offset by 10 GHz at this frequency is  $\sim 80$  pm, which is easily within the resolution capabilities of many commercially available OSAs. The optical power of each frequency component is weighted by the phase modulation index in the squared Bessel function

$$P_{carrier} = |E_o|^2 J_0^2(\delta)$$

$$P_{Lower SB} = P_{Upper SB} = |E_o|^2 J_1^2(\delta). \quad (6.8)$$

For small values of  $\delta$ , the Bessel functions  $J_0(\delta) \rightarrow 1$  and  $J_1(\delta) \rightarrow \delta/2$  meaning the sideband power is proportional to the square of the phase modulation index. In this derivation, RF loss and velocity matching were omitted for simplicity, but incorporating them into the derivation results in coefficients to  $\delta$  that diminish the generated sideband power accordingly. Measured sideband power relative to the carrier power ( $P_{SBRC}$ ) is therefore an informative measurement that indicates the modulator's performance as the operating frequency is increased

$$P_{SBRC} = \left[ \frac{J_1(\delta)}{J_0(\delta)} \right]^2 \approx \frac{\delta^2}{4}. \quad (6.9)$$

The modulation response  $m(f)$  calculated in Section 5.1.3 can be used to estimate the expected sideband power trend for comparison with measured results.  $m(f) = |\Delta\phi(f)|/|\Delta\phi_{DC}|$  is a normalized value between 0–1 that tracks the expected phase shift with frequency, much like the phase modulation index. Therefore when plugged into the Bessel functions of Equation 6.9, an expected sideband power relative to the carrier ( $P_{ExSBRC}$ ) is found that closely mimics the trend in the measured  $P_{SBRC}$ .

$$P_{ExSBRC} = \left[ \frac{J_1(m(f))}{J_0(m(f))} \right]^2 \quad (6.10)$$

Normalizing  $P_{ExSBRC}$  and  $P_{SBRC}$  to the same maximum value allows for direct comparison of measured and expected results, as will be shown in the next section.

### 6.3.2 RF Phase Modulation Measurement

High frequency phase modulators were characterized with the testing setup shown in Figure 6.10. The packaged device was mounted between two piezo-electric

controlled translation stages that allow sub-micron alignment of lensed fibers to the input and output facets of the optical waveguide. The output fiber was fed to a Yokogawa AQ6319 OSA that read a 1 nm spectrum centered on 1550 nm with 10 pm resolution. The modulation signal was provided by a Keysight MXG signal generator capable of operation up to 40 GHz that was directly connected to the 2.4 mm connectors on the input ELC. The output of the modulator was terminated in a 50  $\Omega$  resistive load. To ensure that balanced signals were sent to the modulator, the feed cable loss was accounted for by measuring the cable output on an RF power meter to determine the MXG power setting required for constant output from 0–40 GHz.

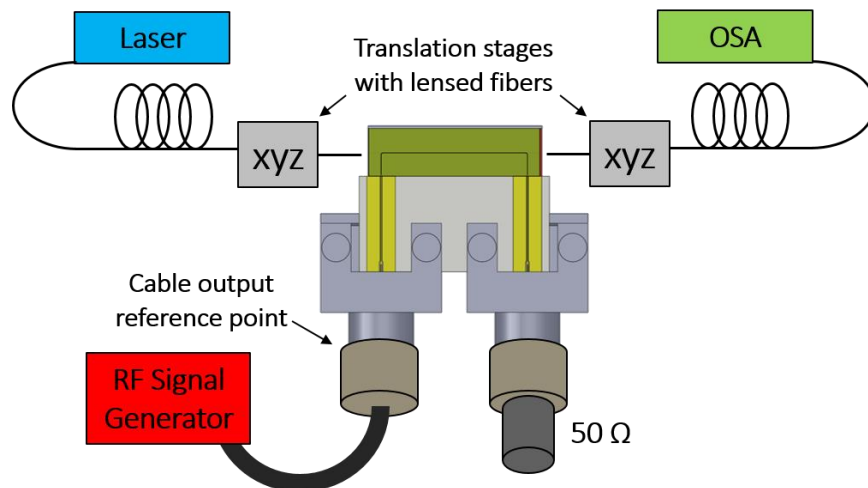


Figure 6.10: RF modulation sideband testing setup.

OSA sideband measurements were taken at frequencies from 5–40 GHz, and the power of the sideband relative to the carrier was evaluated to determine the modulation efficiency at each frequency. The expected RF power loss due to the CPW feed and the microstrip feed length were also accounted for to isolate the response of

the modulator to the power that was delivered to the interaction region of the device. Initial testing showed a very quick modulation response roll-off of  $\sim 10$  dB at 40 GHz. This quickly decaying modulation response was determined to be a result of poor index matching due to a higher optical index of poled SEO250 than the un-poled value that had been previously assumed. Attenuated total-internal-reflection measurements of poled SEO250 revealed an optical index of 1.88 as compared to the un-poled value of 1.77 at 1550 nm. The larger index of poled SEO250 resulted in a significantly higher optical effective index than RF. To better match the effective indexes, the modulator microstrip line was clad in UV15 to fully confine the modulation mode in the higher index polymer. The optical sidebands were re-measured and found to have a significantly lower roll of  $< 5$  dB from 5–40 GHz. The measured OSA data showing the modulation sidebands for the clad microstrip modulator is shown in Figure 6.11.

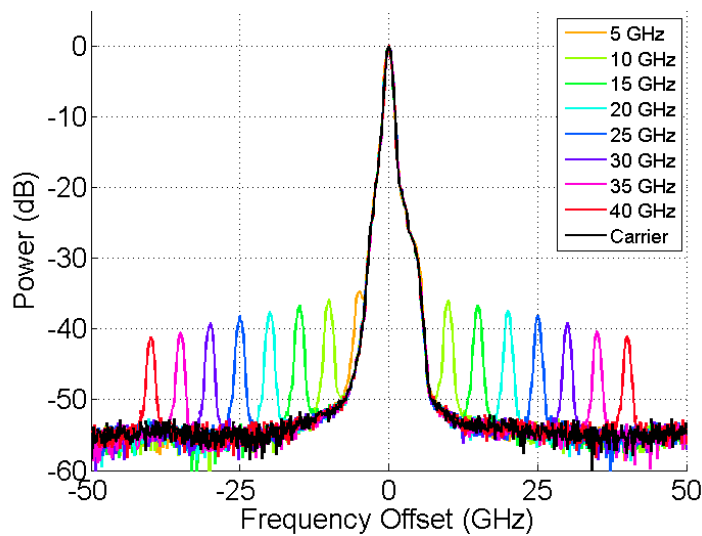


Figure 6.11: Generated optical sidebands from 5–40 GHz of the clad microstrip modulator.

The expected modulation response  $m(f)$  was calculated according to Equation 5.13 using measured attenuation coefficients and numerically calculated optical and RF effective index values. The measured and predicted roll-off of sideband power relative to the carrier ( $P_{SBRC}$  and  $P_{ExSBRC}$ ) for the clad and unclad microstrip modulators are plotted in Figure 6.12.

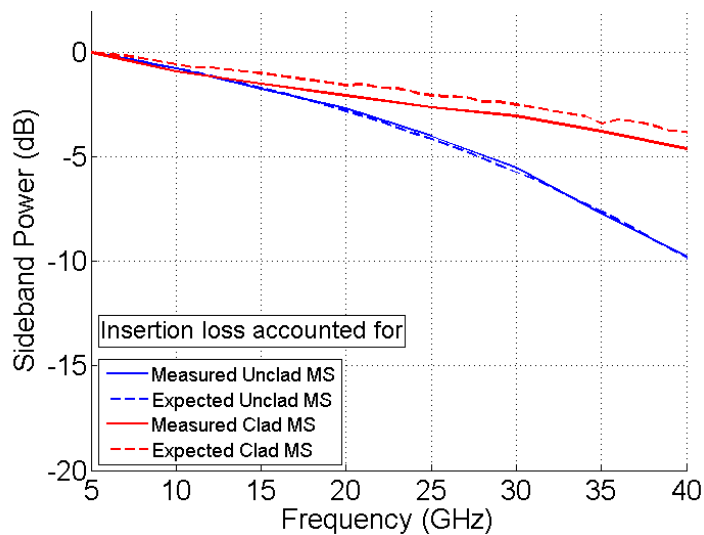


Figure 6.12: Measured and calculated sideband power roll-off for a clad and unclad microstrip modulator normalized to the sideband response at 5 GHz.

Note that because sidebands below 5 GHz could not be distinguished from the carrier, a DC EO response was not measured. The values have therefore been normalized to the sideband power predicted at 5 GHz, and the plot serves only to show the matching frequency trends between measured and expected values. The excellent matching indicates that the calculated  $m(f)$  is an accurate reflection of the modulator's frequency response. The calculated responses for the clad and unclad

microstrip are shown in Figure 6.13 where a 3 dB bandwidth of ~20 GHz for the clad microstrip modulator is apparent.

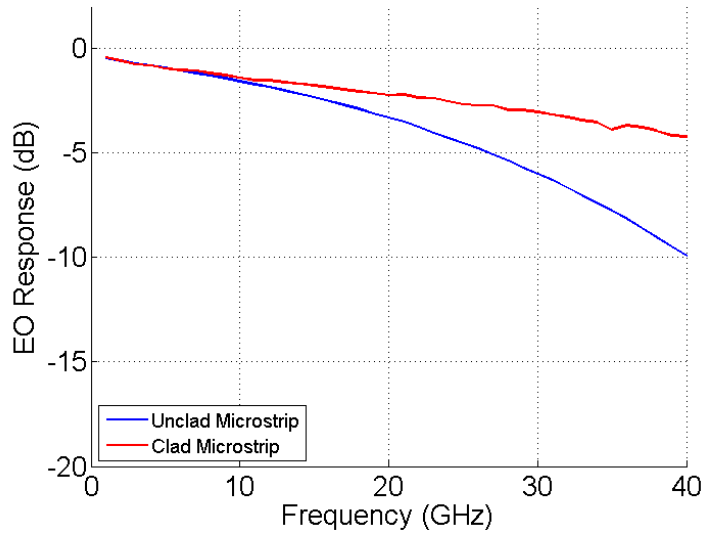


Figure 6.13: Calculated modulation response for a clad and unclad microstrip modulator.

Moving forward, further work on optimizing the OEOM modulator could improve the modulator bandwidth by decreasing the RF loss with lower loss dielectrics and optimizing the electroplating process. Additionally the low frequency  $V_{\pi}$  of the measured devices were around 16 V—much higher than previously measured devices. It is postulated that this was due to the SEO250 solution that was used in this device, which was mixed several months prior to deposition and likely experienced significant chromophore decay from prolonged solvent exposure. However, both drive voltage and bandwidth improvement could be made and easily integrated into this RF packaging scheme. Indeed many of the high performance polymer microstrip based

modulators that have been previously published [43], [89], [98] could easily be modified to include ground plane vias and be made fully compatible with the RF packaging scheme that was demonstrated.

#### **6.4 Conclusion**

Practical usage of high frequency modulators requires concise and efficient packaging along with manipulations of the RF signal prior to being fed to the modulator. The heterogeneous wire bond transition and RF packaging scheme that was demonstrated offers a compact solution for feeding the modulator via a ceramic substrate that is suitable for RF circuitry for signal manipulations, with  $< 1$  dB of added RF loss. The high frequency phase modulation results illustrated the effectiveness of this packaging and could be compatible with most microstrip traveling wave modulators with exposed ground plane contacts.

## **Chapter 7**

### **CONCLUSION**

This final chapter will summarize the work detailed in this dissertation and highlight the original contributions. Following the summary, some thoughts on future efforts that can build on this work will be presented.

#### **7.1 Summary**

The field of microwave photonics is producing a wide variety of new technologies that will ultimately help to solve many modern-day technological challenges. EO modulators are critical to most microwave photonic systems for efficient conversion of a high speed electrical signals onto an optical carrier. LiNbO<sub>3</sub> modulators have been heavily researched and developed over the past several decades, resulting in high performance modulators that have enabled the microwave photonic systems of today. However, as these systems increase in complexity and performance, there is a growing demand for a next generation of modulators with ultra-low drive voltages and extremely high bandwidths. OEOM based modulators offer an avenue for meeting the stringent demands of developing systems due to their very high EO coefficient and ultrafast response times. This work focused on the development and integration of OEOM based modulators that are easily fabricated and scalable, and would be suitable for microwave photonic applications.

The initial challenge was to develop a simply fabricated waveguide with an OEOM core material. This was achieved via an inverted ridge waveguide that

implemented a commercially available cladding material, UV15, and standard lithographic and ICP etching tools. The inverted ridge waveguide was integrated into a DC phase modulator configuration with a lumped element, vertically oriented TM modulation electrode. A thermally enabled poling procedure was developed to induce EO activity into the core material, and a custom made poling apparatus was designed and built. The drive voltage of the DC modulators was then measured with a polarization rotation technique, and  $V_{\pi}$  values down to 1 V were measured, with  $V_{\pi}L$ 's of 3.2 V·cm compared with 17.2 V·cm found in standard LiNbO<sub>3</sub> modulators [99].

The next goal was to integrate these OEOM waveguides into high frequency modulators capable of operating up to 50 GHz. In order to design an efficient device, it was necessary to determine the RF dielectric constant and attenuation factor of the waveguide materials. This turned out to be a challenge for the thin polymer films used in these devices, as most RF material characterization techniques were developed for thick substrates on the order of 100's of microns. A modified microstrip ring resonator technique was therefore developed, which implemented an arc coupler to feed sufficient energy into the ring for a resonance measurement. The arc coupler was designed using numerical electromagnetic simulation software to optimize for sufficient power coupling with minimal loading effect to the ring. Using this technique, the dielectric constant of UV15 and IDK-1-50 were determined up to 110 GHz, and the dielectric loss tangent of UV15 was determined with straight UV15 microstrip S-parameter measurements and curve fitting [100]. This information was then used to design a broadband traveling wave modulator.

Standard traveling wave modulator design requires attention to velocity matching between the optical and RF modes and microwave attenuation. OEOM

modulator design includes an additional factor to account for the need to pole the material for high EO activity. The standard optical/modulation field overlap integral was modified to include a dimensionless poling field distribution that would be proportional to the resultant EO coefficient,  $r_{33}$ . The modified overlap and standard modulation response coefficient were combined with the interaction length to form a comprehensive figure of merit that reveals the relative merits of various traveling wave modulator architectures for OEOM based modulators. The results of this analysis showed conclusively that TM microstrip based modulators are the far superior device configuration. A microstrip based modulator was therefore designed with 50  $\Omega$  impedance, excellent field overlap, minimized RF attenuation and well matched optical and RF wave velocities.

A fabrication procedure was then developed to build a microstrip modulator that included a Cu ground plane and electroplated Au electrodes that were sufficiently thick to minimize conduction losses. An etch process for ground plane vias adjacent to the microstrip feed contact was developed, which exposed the ground without damaging the polymer stack by direct exposure to solvents or temperatures above 100 °C. The vias and microstrip contact pad enabled direct feeding with CPW contact probes, but practical device integration required additional feed design.

RF signals being sent to a modulator frequently require electronic manipulations such as amplifying or filtering that is performed by RF circuitry typically fabricated on traditional RF substrates such as ceramic, Teflon or LCP. These operations can be performed externally by standalone components before the signal is fed to the modulator, but a preferred solution would be to have the RF circuitry packaged compactly with the modulator itself. To this end, a single stage,

heterogeneous, wire bond transition from a CPW on a ceramic substrate to the modulator microstrip was developed that transferred signals from a ceramic substrate to the OEOM modulator with  $< 1$  dB transmission loss up to 50 GHz [101]. This transition was then implemented in a full RF packaging scheme that included coaxial to CPW connectors and the CPW to microstrip transition, allowing for modulator feeding with standard 2.4 mm coaxial cables. The feed loss from the packaging introduced less than 1 dB of loss out to 50 GHz. The packaged phase modulator was then characterized up to 40 GHz, the limitation of the modulation source, by measuring the relative power of the first order sidebands on an optical spectrum analyzer. The modulation response roll-off was below 5 dB at 40 GHz, and the 3 dB bandwidth was  $\sim 20$  GHz [101].

## **7.2 Outlook and Future Work**

The modulator and packaging scheme presented in this dissertation demonstrate the potential for scalable OEOM based modulators and suitable RF packaging for practical system integration. Additionally the dielectric constant characterization technique could be used to compile a library of RF dielectric information of the OEOMs that are currently being utilized as well as those that are still being developed. The demand for high performance modulators that motivated this work is ongoing, and continued work on this front could meet those demands.

There are several avenues for improvement to the modulator in this work. The modulation bandwidth was limited largely by RF attenuation in the microstrip electrode. This was due, in part, to the high dielectric loss of UV15 that was discovered during the material characterization work, and also to the low conductivity of the electroplated Au electrodes. A survey of the RF properties of other

commercially available polymer cladding materials such as the Norland Optical Adhesives or optical silicones from Dow Corning could reveal a superior material system that would allow for lower dielectric loss. Additionally the electroplating process could be optimized by experimenting with techniques such as periodic reverse plating or pulsed current plating for improved conductivity and lower conduction loss.

Perhaps the most compelling reason to continue work on OEOM based modulators is the continual research going into developing new and improved materials. The OEOM modulator demonstrations of the past decade have informed the organic chemistry community who develop these materials, and they are continually making modifications to better suit the needs of the photonics community. As a particular example; a major concern with OEOMs ten years ago was their photostability when exposed with continuous radiation at telecomm wavelengths. This challenge has been largely overcome in more recently developed materials. The materials used in this work demonstrated no degradation in EO activity after 2500 mW·Hr of continuous radiation at 1550 nm. New materials that promise higher EO activities continue to be developed, and studies of poling efficiency and processing are also ongoing. All of these material improvements translate directly into modulator performance enhancement, which leads to compounding overall device improvement as device designs are concurrently optimized. With the progress being made in the photonics and materials research communities, high performance EO modulators will enable future microwave photonic systems for decades to come.

## REFERENCES

- [1] James C. Maxwell, "A Dynamical Theory of the Electromagnetic Field," *Philos. Trans. R. Soc. Lond.*, pp. 459–512, 1865.
- [2] T. H. Maiman, "Stimulated Optical Radiation in Ruby," *Nature*, vol. 187, pp. 493–494, Aug. 1960.
- [3] T. Miya, Y. Terunuma, T. Hosaka, and T. Miyashita, "Ultimate low-loss single-mode fibre at 1.55  $\mu\text{m}$ ," *Electron. Lett.*, vol. 15, no. 4, pp. 106–108, 1979.
- [4] J. Capmany and D. Novak, "Microwave photonics combines two worlds," *Nat. Photonics*, vol. 1, no. 6, pp. 319–330, 2007.
- [5] R. J. Mears, L. Reekie, I. M. Jauncey, and D. N. Payne, "Low-noise erbium-doped fibre amplifier operating at 1.54  $\mu\text{m}$ ," *Electron. Lett.*, vol. 23, no. 19, pp. 1026–1028, 1987.
- [6] Shao-Qiu Xiao and Ming-Tuo Zhou, Eds., *Millimeter Wave Technology in Wireless PAN, LAN, and MAN*. Boca Raton, FL: Taylor and Francis Group, 2008.
- [7] J. Yao, "Microwave Photonics," *J. Light. Technol.*, vol. 27, no. 3, pp. 314–335, Feb. 2009.
- [8] Chi H. Lee, Ed., *Microwave Photonics*, 2nd ed. CRC Press, 2013.
- [9] M. Milosavljevic, M. P. Thakur, P. Kourtessis, J. E. Mitchell, and J. M. Senior, "Demonstration of Wireless Backhauling Over Long-Reach PONs," *J. Light. Technol.*, vol. 30, no. 5, pp. 811–817, Mar. 2012.
- [10] Andrew Wireless Solutions (TM), "ION Series Radio over Fiber." CommScope, Inc., 2008.
- [11] C. Ranaweera, E. Wong, C. Lim, and A. Nirmalathas, "Next generation optical-wireless converged network architectures," *Netw. IEEE*, vol. 26, no. 2, pp. 22–27, 2012.
- [12] G. Chang and C. Liu, "1–100GHz microwave photonics link technologies for next-generation WiFi and 5G wireless communications," in *Microwave Photonics (MWP), 2013 International Topical Meeting on*, 2013, pp. 5–8.
- [13] N. Ghazisaidi and M. Maier, "Fiber-wireless (FiWi) access networks: Challenges and opportunities," *Netw. IEEE*, vol. 25, no. 1, pp. 36–42, 2011.
- [14] B. Lannoo, D. Colle, M. Pickavet, and P. Demeester, "Radio-over-fiber-based solution to provide broadband internet access to train passengers," *IEEE Commun. Mag.*, vol. 45, no. 2, p. 56, 2007.
- [15] S. Koenig, D. Lopez-Diaz, J. Antes, F. Boes, R. Henneberger, A. Leuther, A. Tessmann, R. Schmogrow, D. Hillerkuss, R. Palmer, T. Zwick, C. Koos, W. Freude, O. Ambacher, J. Leuthold, and I. Kallfass, "Wireless sub-THz

- communication system with high data rate,” *Nat. Photonics*, vol. 7, no. 12, pp. 977–981, Oct. 2013.
- [16] A. Kanno, K. Inagaki, I. Morohashi, T. Sakamoto, T. Kuri, I. Hosako, T. Kawanishi, Y. Yoshida, and K. Kitayama, “40 Gb/s W-band (75–110 GHz) 16-QAM radio-over-fiber signal generation and its wireless transmission,” *Opt. Express*, vol. 19, no. 26, pp. B56–B63, 2011.
- [17] A. Hirata, T. Kosugi, H. Takahashi, R. Yamaguchi, F. Nakajima, T. Furuta, H. Ito, H. Sugahara, Y. Sato, and T. Nagatsuma, “120-GHz-band millimeter-wave photonic wireless link for 10-Gb/s data transmission,” *IEEE Trans. Microw. Theory Tech.*, vol. 54, no. 5, pp. 1937–1944, May 2006.
- [18] A. Beling and J. C. Campbell, “InP-Based High-Speed Photodetectors,” *J. Light. Technol.*, vol. 27, no. 3, pp. 343–355, Feb. 2009.
- [19] A. Beling, A. S. Cross, M. Piels, J. Peters, Q. Zhou, J. E. Bowers, and J. C. Campbell, “InP-based waveguide photodiodes heterogeneously integrated on silicon-on-insulator for photonic microwave generation,” *Opt. Express*, vol. 21, no. 22, p. 25901, Nov. 2013.
- [20] J. P. Wilson, C. A. Schuetz, T. E. Dillon, P. Yao, C. E. Harrity, and D. W. Prather, “Passive 77 GHz millimeter-wave sensor based on optical upconversion,” *Appl. Opt.*, vol. 51, no. 18, pp. 4157–4167, 2012.
- [21] N. Salmon, R. Appleby, P. Coward, and others, “Polarimetric passive millimetre wave imaging,” in *Microwave and Millimeter Wave Technology, 2002. Proceedings. ICMMT 2002. 2002 3rd International Conference on*, 2002, pp. 540–543.
- [22] C. A. Schuetz, R. D. Martin, I. Biswas, M. S. Mirotznik, S. Shi, G. J. Schneider, J. Murakowski, and D. W. Prather, “Sparse aperture millimeter-wave imaging using optical detection and correlation techniques,” in *SPIE Vol. 6548*, Orlando, FL, 2007, p. 65480B–65480B–8.
- [23] J. Macario, P. Yao, S. Shi, A. Zablocki, C. Harrity, R. D. Martin, C. A. Schuetz, and D. W. Prather, “Full spectrum millimeter-wave modulation,” *Opt. Express*, vol. 20, no. 21, pp. 23623–23629, 2012.
- [24] C. H. Cox, E. I. Ackerman, G. E. Betts, and J. L. Prince, “Limits on the performance of RF-over-fiber links and their impact on device design,” *IEEE Trans. Microw. Theory Tech.*, vol. 54, no. 2, pp. 906–920, Feb. 2006.
- [25] G. T. Reed, G. Mashanovich, F. Y. Gardes, and D. J. Thomson, “Silicon optical modulators,” *Nat. Photonics*, vol. 4, no. 8, pp. 518–526, Jul. 2010.
- [26] R. Soref and B. Bennett, “Electrooptical effects in silicon,” *IEEE J. Quantum Electron.*, vol. 23, no. 1, pp. 123–129, Jan. 1987.
- [27] Antao Chen and Edmond J. Murphy, Eds., *Broadband Optical Modulators*. Boca Raton, FL: Taylor and Francis Group, 2012.
- [28] J. Macario, Peng Yao, R. Shireen, C. A. Schuetz, Shouyuan Shi, and D. W. Prather, “Development of Electro-Optic Phase Modulator for 94 GHz Imaging System,” *J. Light. Technol.*, vol. 27, no. 24, pp. 5698–5703, Dec. 2009.

- [29] L. R. Dalton, "Electric Field Poled Organic Electro-Optic materials: State of the Art and Future Prospects." *Chemical Reviews*, 2010.
- [30] Colin V. McLaughlin, Michael L. Hayden, Brent Polishak, Su Huang, Jingdong Luo, Taedong Kim, and Alex K.-Y. Jen, "Wideband 15-THz response using organic electrooptic emitter-sensor pairs at telecommunications wavelengths," *Appl. Phys. Lett.*, vol. 92, pp. 151107–1, 2008.
- [31] H. -C. Song, M. -C. Oh, S. -W. Ahn, and W. H. Steier, "Flexible low-voltage electro-optic polymer modulators," *Appl. Phys. Lett.*, vol. 82, p. 4421, 2003.
- [32] David L.K. Eng, Stephen Kozacik, Shouyuan Shi, Benjamin C. Olbricht, and Dennis W. Prather, "All-Polymer modulator for high frequency low drive voltage application," in *SPIE 8983, Organic Photonic Materials and Devices XVI*, San Francisco, California, USA, 2014.
- [33] S. Takahashi, B. Bhola, A. Yick, W. H. Steier, Jingdong Luo, A. K.-Y. Jen, Dan Jin, and R. Dinu, "Photo-Stability Measurement of Electro-Optic Polymer Waveguides With High Intensity at 1550-nm Wavelength," *J. Light. Technol.*, vol. 27, no. 8, pp. 1045–1050, Apr. 2009.
- [34] M. Lee, O. Mitrofanov, H. E. Katz, and C. Erben, "Millimeter-wave dielectric properties of electro-optic polymer materials," *Appl. Phys. Lett.*, vol. 81, no. 8, p. 1474, 2002.
- [35] T. Baehr-Jones, B. Penkov, J. Huang, P. Sullivan, J. Davies, J. Takayesu, J. Luo, T.-D. Kim, L. Dalton, A. Jen, M. Hochberg, and A. Scherer, "Nonlinear polymer-clad silicon slot waveguide modulator with a half wave voltage of 0.25 V," *Appl. Phys. Lett.*, vol. 92, no. 16, p. 163303, 2008.
- [36] Y. Enami, B. Yuan, M. Tanaka, J. Luo, and A. K. Y. Jen, "Electro-optic polymer/TiO<sub>2</sub> multilayer slot waveguide modulators," *Appl. Phys. Lett.*, vol. 101, no. 12, pp. 123509–123509, 2012.
- [37] S. Shi and D. W. Prather, "Ultrabroadband Electro-Optic Modulator Based on Hybrid Silicon-Polymer Dual Vertical Slot Waveguide," *Adv. Optoelectron.*, vol. 2011, pp. 1–6, 2011.
- [38] S. Shi and D. W. Prather, "Dual rf-optical slot waveguide for ultrabroadband modulation with a subvolt V- $\pi$ ," *Appl. Phys. Lett.*, vol. 96, no. 20, p. 201107, 2010.
- [39] X. Zhang, C. Chung, A. Hosseini, H. Subbaraman, J. Luo, A. Jen, R. Neilson, C. Lee, and R. T. Chen, "High Performance Optical Modulator Based on Electro-optic Polymer Filled Silicon Slot Photonic Crystal Waveguide," *J. Light. Technol.*, pp. 1–1, 2015.
- [40] G. Xu, Z. Liu, J. Ma, B. Liu, S. T. Ho, L. Wang, P. Zhu, T. J. Marks, J. Luo, and A. K. Jen, "Organic electro-optic modulator using transparent conducting oxides as electrodes," *Opt Express*, vol. 13, no. 19, pp. 7380–7385, 2005.
- [41] Y. Enami, C. T. DeRose, C. Loychik, D. Mathine, R. A. Norwood, J. Luo, A. K.-Y. Jen, and N. Peyghambarian, "Low half-wave voltage and high electro-optic effect in hybrid polymer/sol-gel waveguide modulators," *Appl. Phys. Lett.*, vol. 89, no. 14, p. 143506, 2006.

- [42] Y. Enami, D. Mathine, C. T. DeRose, R. A. Norwood, J. Luo, A. K.-Y. Jen, and N. Peyghambarian, "Hybrid cross-linkable polymer/sol-gel waveguide modulators with 0.65 V half wave voltage at 1550 nm," *Appl. Phys. Lett.*, vol. 91, no. 9, p. 093505, 2007.
- [43] D. Chen, H. R. Fetterman, A. Chen, W. H. Steier, L. R. Dalton, W. Wang, and Y. Shi, "Demonstration of 110 GHz electro-optic polymer modulators," *Appl. Phys. Lett.*, vol. 70, p. 3335, 1997.
- [44] G. Cocorullo, M. Iodice, and I. Rendina, "All-silicon Fabry–Perot modulator based on the thermo-optic effect," *Opt. Lett.*, vol. 19, no. 6, pp. 420–422, 1994.
- [45] N. Takato, K. Jinguji, M. Yasu, H. Toba, and M. Kawachi, "Silica-based single-mode waveguides on silicon and their application to guided-wave optical interferometers," *Light. Technol. J. Of*, vol. 6, no. 6, pp. 1003–1010, 1988.
- [46] G. W. Scherer, "Stress-induced index profile distortion in optical waveguides," *Appl. Opt.*, vol. 19, no. 12, pp. 2000–2006, 1980.
- [47] B. Saleh and M. Teich, *Fundamentals of Photonics*. New York, NY: John Wiley and Sons, Inc., 1991.
- [48] R. Walker, "High-Speed Electrooptic Modulation in GaAs/GaAlAs Waveguide Devices," *J. Light. Technol.*, vol. LT-5, no. 10, pp. 1444–1453, Oct. 1987.
- [49] O. D. Herrera, R. Himmelhuber, K.-J. Kim, R. A. Norwood, and N. Peyghambarian, "Silicon/electro-optic polymer hybrid directional coupler switch," 2014, p. 89910Q.
- [50] F. Qiu, A. M. Spring, F. Yu, I. Aoki, A. Otomo, and S. Yokoyama, "Thin TiO<sub>2</sub> core and electro-optic polymer cladding waveguide modulators," *Appl. Phys. Lett.*, vol. 102, no. 23, p. 233504, 2013.
- [51] R. Ding, T. Baehr-Jones, W.-J. Kim, B. Boyko, R. Bojko, A. Spott, A. Pomerene, C. Hill, W. Reinhardt, and M. Hochberg, "Low-loss asymmetric strip-loaded slot waveguides in silicon-on-insulator," *Appl. Phys. Lett.*, vol. 98, no. 23, p. 233303, 2011.
- [52] R. Ding, T. Baehr-Jones, W.-J. Kim, X. Xiong, R. Bojko, J.-M. Fedeli, M. Fournier, and M. Hochberg, "Low-loss strip-loaded slot waveguides in Silicon-on-Insulator," *Opt. Express*, vol. 18, no. 24, pp. 25061–25067, Nov. 2010.
- [53] Y. Enami, D. Mathine, C. T. DeRose, R. A. Norwood, J. Luo, A. K.-Y. Jen, and N. Peyghambarian, "Transversely tapered hybrid electro-optic polymer/sol-gel Mach–Zehnder waveguide modulators," *Appl. Phys. Lett.*, vol. 92, no. 19, p. 193508, 2008.
- [54] Reem Song, Hyun-Chae Song, W. H. Steier, and C. H. Cox, "Analysis and Demonstration of Mach–Zehnder Polymer Modulators Using In-Plane Coplanar Waveguide Structure," *Quantum Electron. IEEE J. Of*, vol. 43, no. 8, pp. 633–640, 2007.
- [55] Seong-Ku Kim, H. Zhang, D. H. Chang, C. Zhang, C. Wang, W. H. Steier, and H. R. Fetterman, "Electrooptic polymer modulators with an inverted-rib waveguide structure," *IEEE Photonics Technol. Lett.*, vol. 15, no. 2, pp. 218–220, Feb. 2003.

- [56] Y. Enami, C. T. Derose, D. Mathine, C. Loychik, C. Greenlee, R. A. Norwood, T. D. Kim, J. Luo, Y. Tian, A. K.-Y. Jen, and N. Peyghambarian, "Hybrid polymer/sol-gel waveguide modulators with exceptionally large electro-optic coefficients," *Nat. Photonics*, vol. 1, no. 3, pp. 180–185, Mar. 2007.
- [57] Antao Chen, V. Chuyanov, S. Garner, W. H. Steier, and Larry R. Dalton, "Modified attenuated total reflection for the fast and routine electro-optic measurement of nonlinear optical polymer thin films," presented at the Organic Thin Films for Photonics Applications, Long Beach, CA, 1997, vol. 14, pp. 158–160.
- [58] Z. Zhu and T. Brown, "Full-vectorial finite-difference analysis of microstructured optical fibers," *Opt. Express*, vol. 10, no. 17, pp. 853–864, 2002.
- [59] J. P. Berenger, "A perfectly matched layer for the absorption of electromagnetic waves," *J. Comput. Phys.*, vol. 114, no. 2, pp. 185–200, 1994.
- [60] A. Yariv, *Optical Electronics*, 3rd ed. Holt, Rinehart and Winston, 1985.
- [61] B. C. Olbricht, P. A. Sullivan, P. C. Dennis, J. T. Hurst, L. E. Johnson, S. J. Benight, J. A. Davies, A. Chen, B. E. Eichinger, P. J. Reid, L. R. Dalton, and B. H. Robinson, "Measuring Order in Contact-Poled Organic Electrooptic Materials with Variable-Angle Polarization-Referenced Absorption Spectroscopy (VAPRAS)," *J. Phys. Chem. B*, vol. 115, no. 2, pp. 231–241, Jan. 2011.
- [62] B. C. Olbricht, P. A. Sullivan, G.-A. Wen, A. A. Mistry, J. A. Davies, T. R. Ewy, B. E. Eichinger, B. H. Robinson, P. J. Reid, and L. R. Dalton, "Laser-Assisted Poling of Binary Chromophore Materials," *J. Phys. Chem. C*, vol. 112, no. 21, pp. 7983–7988, May 2008.
- [63] C. C. Teng and H. T. Man, "Simple reflection technique for measuring the electro-optic coefficient of poled polymers," *Appl. Phys. Lett.*, vol. 56, no. 18, pp. 1734–1736, 1990.
- [64] D. H. Park, C. H. Lee, and W. N. Herman, "Analysis of multiple reflection effects in reflective measurements of electro-optic coefficients of poled polymers in multilayer structures," *Opt Express*, vol. 14, no. 19, pp. 8866–8884, Sep. 2006.
- [65] S. Musa, N. Lagali, G. Sengo, A. Driessen, and others, "Fabrication of Polymeric Multimode Waveguides for Application in the Local Area Network and Optical Interconnects.," presented at the 2000 IEEE Photonics Society Benelux Symposium, 2000.
- [66] John A. Woollam and Paul G. Snyder, "Fundamentals and Applications of Variable Angle Spectroscopic Ellipsometry," *Mater. Sci. Eng. B5*, vol. 5, no. 2, pp. 279–283, Jan. 1990.
- [67] P. Troughton, "Measurement techniques in microstrip," *Electron. Lett.*, vol. 5, no. 2, pp. 25–26, 1969.
- [68] C. Free and R. Hopkins, "Equivalent circuit for the microstrip ring resonator suitable for broadband materials characterisation," *IET Microw. Antennas Propag.*, vol. 2, no. 1, pp. 66–73, Feb. 2008.

- [69] K. Saeed, R. D. Pollard, and I. C. Hunter, "Substrate Integrated Waveguide Cavity Resonators for Complex Permittivity Characterization of Materials," *IEEE Trans. Microw. Theory Tech.*, vol. 56, no. 10, pp. 2340–2347, Oct. 2008.
- [70] L. F. Chen, C. K. Ong, C. P. Neo, V. V. Varadan, and V. K. Varadan, *Microwave Electronics: Measurement and Materials Characterization*, 1st ed. Wiley, 2004.
- [71] L.-H. Hsieh and K. Chang, "Equivalent lumped elements  $G$ ,  $L$ ,  $C$ , and unloaded  $Q$ 's of closed-and open-loop ring resonators," *Microw. Theory Tech. IEEE Trans. On*, vol. 50, no. 2, pp. 453–460, 2002.
- [72] C.-C. Yu and K. Chang, "Transmission-line analysis of a capacitively coupled microstrip-ring resonator," *Microw. Theory Tech. IEEE Trans. On*, vol. 45, no. 11, pp. 2018–2024, 1997.
- [73] G. Zou, H. Gronqvist, P. Starski, and J. Liu, "High frequency characteristics of liquid crystal polymer for system in a package application," in *Advanced Packaging Materials, 2002. Proceedings. 2002 8th International Symposium on*, 2002, pp. 337–341.
- [74] D. C. Thompson, O. Tantot, H. Jallageas, G. E. Ponchak, M. M. Tentzeris, and J. Papapolymerou, "Characterization of Liquid Crystal Polymer (LCP) Material and Transmission Lines on LCP Substrates From 30 to 110 GHz," *IEEE Trans. Microw. Theory Tech.*, vol. 52, no. 4, pp. 1343–1352, Apr. 2004.
- [75] I. Wolff and N. Knoppik, "Microstrip ring resonator and dispersion measurement on microstrip lines," *Electron. Lett.*, vol. 7, no. 26, pp. 779–781, 1971.
- [76] G. E. Ponchak and A. N. Downey, "Characterization of thin film microstrip lines on polyimide," *Compon. Packag. Manuf. Technol. Part B Adv. Packag. IEEE Trans. On*, vol. 21, no. 2, pp. 171–176, 1998.
- [77] F. Schnieder and W. Heinrich, "Model of thin-film microstrip line for circuit design," *Microw. Theory Tech. IEEE Trans. On*, vol. 49, no. 1, pp. 104–110, 2001.
- [78] G. Kompa, *Practical Microstrip Design and Applications*. 685 Canton Street, Norwood, MA 02062: Artech House, 2005.
- [79] E. Hammerstad and O. Jensen, "Accurate Models for Microstrip Computer-Aided Design," *IEEE MTT- Int Microw. Symp Dig.*, pp. 407–409, 1980.
- [80] Thomas S. Laverghetta, *Microwave Materials and Fabrication Techniques*, 3rd ed. Norwood, MA: Artech House, 2000.
- [81] Robert A. Pucel, Daniel J. Masse, and Curtis P. Hartwig, "Losses in Microstrip," *IEEE Trans. Microw. Theory Tech.*, vol. MTT-16, no. 6, Jun. 1968.
- [82] R. A. Pucel, D. J. Masse, and C. P. Hartwig, "Correction to ' Losses in Microstrip' (Correspondence)," *Microw. Theory Tech. IEEE Trans. On*, vol. 16, no. 12, pp. 1064–1064, 1968.
- [83] J. H. C. Van Heuven, "Conduction and Radiation Losses in Microstrip (Short Papers)," *Microw. Theory Tech. IEEE Trans. On*, vol. 22, no. 9, pp. 841–844, 1974.

- [84] H. A. Wheeler, "Formulas for the skin effect," *Proc. IRE*, vol. 30, no. 9, pp. 412–424, 1942.
- [85] S. P. Morgan, "Effect of Surface Roughness on Eddy Current Losses at Microwave Frequencies," *J. Appl. Phys.*, vol. 20, no. 4, p. 352, 1949.
- [86] Lynn Hutcheson, *Integrated Optical Circuits and Components*, vol. 13. New York, NY: Marcel Dekker, Inc, 1987.
- [87] Ivan P. Kaminow and Thomas L. Koch, *Optical Fiber Telecommunications Volume IIIb*, vol. IIIb. San Diego, CA: Academic Press, 1997.
- [88] Aref Chowdhury and Leon McCaughan, "Figure of Merit for Near-Velocity-Matched Traveling-Wave Modulators," *Opt. Lett.*, vol. 26, no. 17, pp. 1317–1319, Sep. 2001.
- [89] C. C. Teng, "Traveling-wave polymeric optical intensity modulator with more than 40 GHz of 3-dB electrical bandwidth," *Appl. Phys. Lett.*, vol. 60, no. 13, p. 1538, 1992.
- [90] B. M. A. Rahman and S. Haxha, "Optimization of microwave properties for ultrahigh-speed etched and unetched lithium niobate electrooptic modulators," *J. Light. Technol.*, vol. 20, no. 10, pp. 1856–1863, Oct. 2002.
- [91] H. Chung, W. S. Chang, and E. L. Adler, "Modeling and optimization of traveling-wave LiNbO<sub>3</sub> interferometric modulators," *Quantum Electron. IEEE J. Of*, vol. 27, no. 3, pp. 608–617, 1991.
- [92] Rainee N. Simons, *Coplanar Waveguide Circuits, Components, and Systems.*, 1st ed. New York, NY: John Wiley and Sons, Inc., 2001.
- [93] E. O. Hammerstad, "Equations for microstrip circuit design," in *Microwave Conference, 1975. 5th European*, 1975, pp. 268–272.
- [94] J. S. Rigden, *Macmillan Encyclopedia of Physics*. New York, NY: Simon and Schuster Macmillan, 1996.
- [95] K. L. Chavez and D. W. Hess, "A Novel Method of Etching Copper Oxide Using Acetic Acid," *J. Electrochem. Soc.*, vol. 148, no. 11, p. G640, 2001.
- [96] A. Satta, D. Shamiryan, M. R. Baklanov, C. M. Whelan, Q. Toan Le, G. P. Beyer, A. Vantomme, and K. Maex, "The Removal of Copper Oxides by Ethyl Alcohol Monitored In Situ by Spectroscopic Ellipsometry," *J. Electrochem. Soc.*, vol. 150, no. 5, p. G300, 2003.
- [97] O. Herrera, K.-J. Kim, R. Voorakaranam, R. Himmelhuber, S. Wang, Q. Zhan, L. Li, R. Norwood, R. Neilson, J. Luo, A. Jen, and N. Peyghambarian, "Silica/Electro-optic Polymer Optical Modulator with Integrated Antenna for Microwave Receiving," *J. Light. Technol.*, pp. 1–1, 2014.
- [98] R. J. Michalak, Ying-Hao Kuo, F. D. Nash, A. Szep, J. R. Caffey, P. M. Payson, F. Haas, B. F. McKeon, P. R. Cook, G. A. Brost, Jingdong Luo, A. K.-Y. Jen, L. R. Dalton, and W. H. Steier, "High-speed AJL8/APC polymer modulator," *IEEE Photonics Technol. Lett.*, vol. 18, pp. 1207–1209, Jun. 2006.
- [99] D. Eng, S. Kozacik, I. Kosilkin, J. Wilson, D. Ross, S. Shi, L. Dalton, B. Olbricht, and D. Prather, "Simple Fabrication and Processing of an All-Polymer Electro-Optic Modulator," *J. Sel. Top. Quantum Electron.*, 2013.

- [100] D. L. K. Eng, B. C. Olbricht, S. Shi, and D. W. Prather, "Dielectric characterization of thin films using microstrip ring resonators," *Microw. Opt. Technol. Lett.*, vol. 57, no. 10, pp. 2306–2310, Oct. 2015.
- [101] David L.K. Eng, Zion Aranda, Benjamin C. Olbricht, Shouyuan Shi, and Dennis W. Prather, "Heterogeneous Packaging of Organic Electro-Optic Modulators with RF Substrates," *Photonics Technol. Lett. IEEE*.

## Appendix A

### PERMISSIONS TO USE COPYRIGHTED MATERIAL

Figures in the introduction were taken from copyrighted material. Permission was or is being obtained to use those figures.

#### A.1 Figure 1.1

Figure 1.1 used plots from references [3] and [5]. Contact has been made to gain permission to use these figures as shown in the below email.

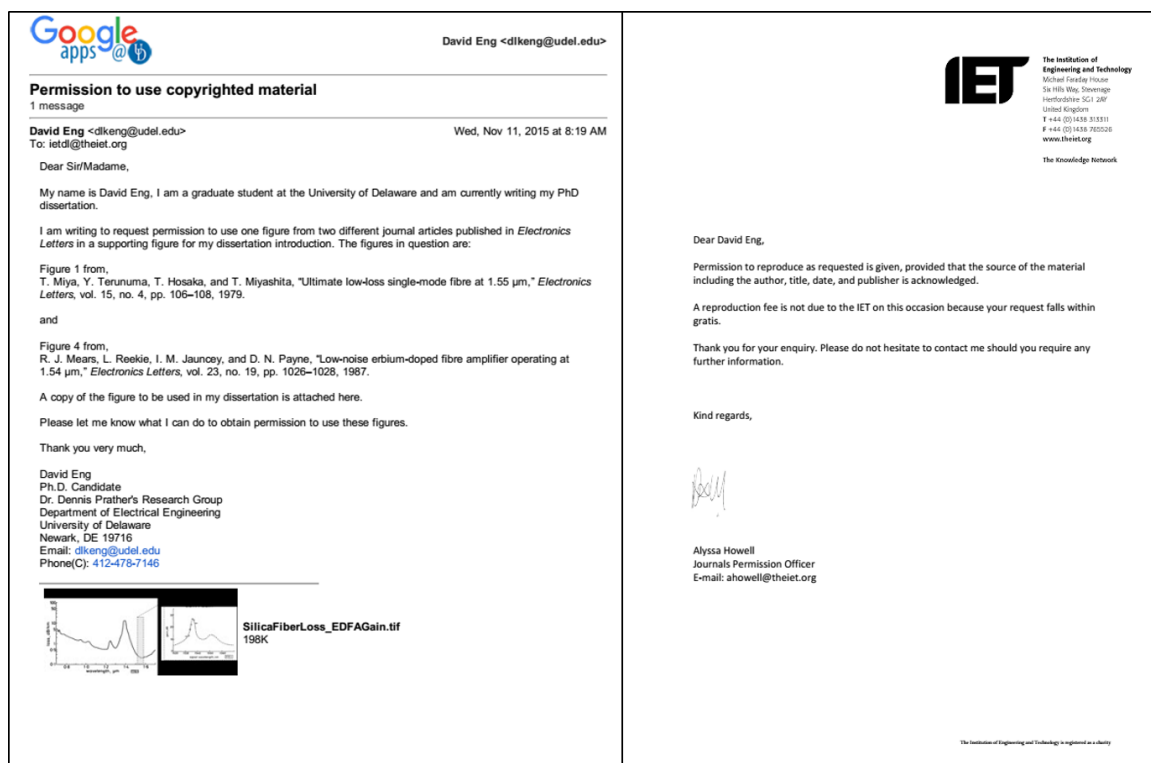


Figure A.1: Permission to use plots in Figure 1.1.

## A.2 Figure 1.2

Figure 1.2 was taken from the book in reference [6], with permission as shown below.

The screenshot shows the Copyright Clearance Center (CCC) website interface. At the top, there is a navigation bar with the CCC logo, a user greeting 'Welcome, David', and links for 'Log out', 'Cart (0)', 'Manage Account', 'Feedback', 'Help', and 'Live Help'. Below the navigation bar is a search bar with the text 'Get Permission / Find Title' and a search input field containing '978-0-8493-8227-7'. A 'Go' button is next to the search bar. A note below the search bar states: 'Note: Copyright.com supplies permissions but not the copyrighted content itself.' The main content area is titled 'Step 3: Order Confirmation' and features a progress indicator with three steps: '1 PAYMENT', '2 REVIEW', and '3 CONFIRMATION'. Below the title, there are links for 'Start new search >' and 'View your Order History >'. A 'Print order information' link is also present. A large text box contains a 'Thank you for your order!' message and contact information. Below this, the 'Confirmation Number: 11487397' and 'Order Date: 11/11/2015' are displayed. A 'Payment Information' section lists the user's name, university, and contact details. The 'Order Details' section includes the title 'Millimeter wave technology in wireless PAN, LAN, and MAN', order ID, license ID, ISBN, publication type, publisher, and author/editor. The 'Permission Status' is 'Granted' with a green checkmark, and the 'Permission type' is 'Republish or display content'. The 'Type of use' is 'Republish in a thesis/dissertation'. A 'View details' link is provided. A note at the bottom of the order details states: 'Note: This item will be invoiced or charged separately through CCC's RightsLink service. More info \$ 0.00'. At the very bottom, a summary bar shows 'Total order items: 1', 'This is not an invoice.', and 'Order Total: 0.00 USD'.

Figure A.2: Permission to use plot in Figure 1.2.